Vietnam Upwelling

Analysis of the upwelling and related processes in the coastal area off South Vietnam

Dissertation

Zur Erlangung des Doktorgrades
der Naturwissenschaften
im Department für Geowissenschaften
der Universität Hamburg

vorgelegt von

Hartmut Hein
aus
Heide

Hamburg
2008

Als Dissertation angenommen vom
Department Geowissenschaften der Universität Hamburg
auf Grund der Gutachten von

Prof. Dr. J. Sündermann
und
Dr. Th. Pohlmann

Hamburg, den 19.12.2007
Prof. Dr. Oßenbrügge
(Leiter des Departments Geowissenschaften)

Abstract

The coastal upwelling off southern Vietnam is one of the major hydrographic features of the South China Sea. While the extent at the coast is less than 100 km, it builds a cold filament, which transports the colder water up to 800 km offshore. The varying bathymetry, the influence of the riverine discharge of the Mekong and the seasonal monsoon winds form a complex system to investigate, which exhibits most of the processes involved in upwelling at western boundaries.

In this work, the upwelling is studied, using a three-dimensional model, which considers both, the local and the basin-wide forcing. The numeric model is based on the HAMburg Shelf Ocean Model (HAMSOM) in its latest version. It allows a high horizontal and vertical resolution. The model is validated with ship experiments, which belong to this work. This cruises took place during different seasons, and give a first view on the distribution of the hydrography in this region.

The results of the simulation discover a complex horizontal circulation, which can be divided into six states. Dependent on the state, two boundary currents, one from the north and one from the south, interacting alone or together with the bathymetry. Each state is influenced by mesoscale and bathymetric steered circulations. In three states a mesoscale anticyclonic eddy in a canyon-like structure is the most obvious feature.

Unlike former suggestions, the results from the simulation, as well as the observation demonstrate, that upwelling can be found independent from the season. Both, the local wind and the basin wide circulation force the vertical velocities. The classical upwelling processes, induced by Ekman motions in the boundary layers, do not explain the vertical velocities at several times.

Particularity, during winter the southward boundary current interacts with the bathymetry. In the regions were the shelf changes its depth, the boundary current can cross the isobathes, due to inertial forces and the occurrence of a high Froude number. Hence, the boundary current flows into shallower water, and will be squashed. This squashing causes an anticyclonic rotation of the current, because the flow has to conserve its potential vorticity. Both processes together induce significant upwelling.

Generally, the basin wide forcing yields 40 % to 100 % of the magnitude of the upwelling in the VUA.

The physical upwelling process influences the biologic primary production during spring, summer and winter. The chlorophyll *a* concentration, observed by remote sensing, as a good indication for the strength of the upwelling, shows a inter-annual correlation with the El Nino Southern Oscillation.

Contents

1
Introduction

1.1 Motivation

Coastal Upwelling, the process which moves cold and particularly nutrient-rich water towards the surface, is one of the most important physical processes for the primary production. Thus, it has a great influence on some of the most productive fishery areas in the world, which are the basis for the availability of food and the economic power in these areas. It also influences the transport of suspended matter and the distribution of the stratification on the shelf.

This thesis is part of an interdisciplinary project and was carried out in close cooperation with the other partners participating in the German-Vietnamese cooperation in marine sciences. One of the overall interests is the influence of the upwelling on the primary production. In oligotrophic waters, such as those off Vietnam, each nutrient enrichment due to upwelling is an important source for the regional growth of phytoplankton. Satellite observations of chlorophyll discover a jet of upwelling-influenced water (Fig. 1.1) during summer. This strong offshore jet is a typical characteristic of the upwelling off Vietnam. Interestingly, the offshore jet has a large extent, while the spatial extent of the upwelling near the coast is comparatively small.

In this thesis the focus is set on the physical processes of the southern Vietnam Upwelling Area (VUA). Without knowledge of the physical processes it is not possible to understand the biological processes related to the primary production.

In this work, the expression “upwelling” is used for all upward directed vertical motion of the water. This fulfils the requirements of Wooster (1981) who laments that there is since now only “a popular image of upwelling”.

The classical coastal upwelling process is forced by local alongshore wind, resulting in a net transport of the surface water to the right (northern hemisphere), relative to the wind

direction. This has to be compensated by onshore transport of water in the interior. Unquestionable, this is the most important process, but in many areas in the world this is contradictory to the observed hydrographic parameters. Referring these inconsistencies, Wooster (1981) called the classical coastal upwelling as a “upwelling mythology”.
In the meantime, there are several other processes known to induce upwelling. During the past years these got more attention by researchers. Especially upwelling induced by currents, or more precisely the interaction between currents and a sloping bottom or the bathymetry, are of interest. Because these interactions are not deducible in two dimensions, three-dimensional models are needed (Thomson and O’Brian, 1973). This demand is satisfied by the use of modelling studies with HAMSOM.

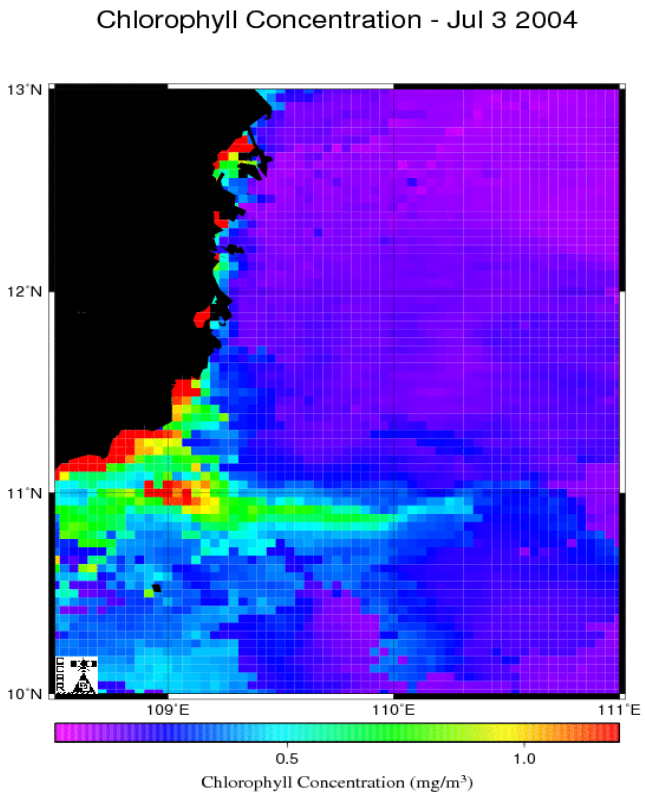

Fig. 1.1: The offshore-directed jet discovered by
the chlorophyll concentration of satellite observations

Coastal upwelling at the east coasts of oceans are a well-known phenomenon, while at west coasts upwelling is not commonly found. Nevertheless, several intensive upwelling regions at western coasts are known, like those off the coasts of Somalia, New Jersey or Yucatan.

Due to the westward intensification of ocean currents, upwelling at western boundaries is more strongly influenced by the currents of the basin-wide circulation than at eastern boundaries. In the South China Sea, western boundary currents with velocities of more than 1 m s^{-1} are not uncommon. Thus, bottom friction and interaction with bathymetric variations may have a stronger influence on the upwelling process.

1.2 Research Goals

The research goals as defined by the proposal are:

1 Analysis of the seasonal variability; especially the influence of the monsoon on the variability of the coastal processes will be studied.

2 Identification of governing processes: Here it will be analysed how the different factors, wind, topography, density field and external factors, interact in their influence on the coastal variability. To achieve a full understanding of the processes it is crucial to investigate also the interim phase between the two monsoons and the opposite situation during the winter monsoon.

3 Analysis of the inter-annual variability of the coastal activity; especially the impact of ENSO and climate changes on the coastal processes will be investigated.

1.3 Outline

This thesis contains 10 chapters. After this short introduction, the second is a short review of the South China Sea, the related monsoon system and previous research on the Vietnamese upwelling. Of course, certain information about the surface and the subsurface circulation of the whole South China Sea is necessary to understand the physical processes.
The third Chapter illustrates the methods, which were used to obtain that information, both hydrodynamic modeling and ship experiments were conducted. The surveys consist mostly of CTD measurements. The hydrodynamic simulation was performed with an adapted version of HAMSOM, which is a well-established shelf ocean model. In the fourth chapter, the regional version of the model is validated. The three-dimensional circulation in the region of upwelling will be illustrated and classified in the fifth chapter. Chapter six

illustrates the results from the five ship experiments. These, however, do not suffice to understand the physical processes, but they can confirm the simulation results. Besides the hydrographic parameters, the in-situ observations of the fluorescence are used to introduce in the impact of the upwelling on the primary production.

Next, the theoretical physical upwelling processes that are vital for this area are described. Chapter seven deals with the classical wind-driven and current-driven upwelling related to two dimensions. The magnitudes of both processes are set in relation to the simulation of the model. The monthly variability of the vertical velocities is illustrated.

With the results from the hydrodynamic model one can deduce even those processes, which can not be explained with simple two-dimensional idealizations. Chapter eight focuses on these processes. The effect of the wind-stress-curl is discussed. The effects of the boundary current interacting with the bathymetry are deduced, particularly with regard to the mechanisms which induce upwelling independent from the local forcing.

Moreover, the influence of the local wind and the riverine discharge from the Mekong river on the magnitude of the vertical velocities will be illustrated with model experiments.

Chapter nine analyses the inter-annual variability of the upwelling by using satellite-based chlorophyll observations.

The last chapter summarises the findings of this thesis and deals with unanswered questions.

2
The South China Sea

This chapter introduces in the geomorphology, the monsoon and the circulation of the South China Sea in the kind of a review. It will give the necessary understanding of the essentially external factors which influence the horizontal, and with that the vertical circulation in the area east of Vietnam. A review of the research in the upwelling regions of the SCS is given.

2.1Geomorphology

The South China Sea (SCS) is the greatest marginal sea of the western Pacific. It covers an area from the equator to 25° N and from 99° E to 122° E. The maximum depth is greater than 5000 m in the central bowl-shaped area. This deep central area has an extension of 800 km x 600 km and is surrounded by two great shelf areas: in the north from the Gulf of Tonkin to the Taiwan Street, in the south the Sunda Shelf, which includes the Gulf of Thailand. Both shelf regions are shallower than 100 m to 200 m.
In the eastern part of the SCS, near the Philippines as well as off central Vietnam the shelf is small (< 50 km) and the shelf slope is steep.
The SCS is connected with the Pacific Ocean (Philippine Sea) through the Luzon Strait (LS). The northern part of the LS is called the Bashy Channel with a sill depth of about 2000 m. It is the only place where water of such depth can enter or leave the SCS. In the southern Part of the LS several islands divide the LS into smaller channels. A typical depth for a channel is about 1000 m. The largest of these channels is the Balitang Channel between the Batan Islands and the Babuyan Islands. In the north the SCS is connected with the East China Sea by the Taiwan Street. The maximum sill depth of the Taiwan Street is less than

100 m.
In the east between the Busuanga Island and the Mindoro Island the SCS is connected with the Sulu Sea by the Mindoro Street. It has a sill depth of about 500 m. South of the Mindoro Street there are a lot of small canals like the Linapacan Strait or the Balabac Strait, all of which have depths of only a couple of meters.
In the west the SCS is connected with the Adaman Sea, a part of the Indian Ocean, by the Strait of Malacca. Near Singapore the Strait of Malacca is narrow (< 10 km) and shallow (< 20 m).
In the south the SCS is connected to the Java Sea by the Kalimanta Street. The Strait of Malacca, the Java Sea and the Kalimanta Street form the northernmost part of the so called Indonesian Throughflow, the connection between the Pacific Ocean and the Indian Ocean.
Many islands are located in the SCS. The biggest is the Hainan Island, which separates the Gulf of Tonkin from the central SCS. The Paracel Islands are located at 16° N in the central SCS. They are surrounded by waters with a depth of more than 2000 m without a shelf area.
In the southern deep-sea basin the Spratly Islands stand out like needles, coming up from a depth of up to 3000 m, and are accompanied by many reefs.

2.2The South China Sea Monsoon System

The Monsoon in general is a global circulation system caused by the contrast of the sealevel pressure between land and sea, like a sea-breeze on global scale (Lau et al. 1988). The Asian Monsoon System (AMS) is controlled by slowly varying boundary conditions, mainly the sea surface temperatures (Lau and Yang 1996, Webster and Yang 1992, Webster 1983). Monsoon systems are related to movements of the inter-tropical convergence with its band of convection. The wind direction is southwest during summer and northeast during winter. The Asian monsoon has been of interest to researchers for centuries, because of the water that the monsoon moves to the continent, which is vital to life for the whole of South Asia (Webster, 1987). The AMS affecting the clime on planarity scale, e.g. the weather and clime in Europe and even North America (Yang et al., 2002; Thorpe et al., 2002; Neale and Slingo, 2003). It seems, that this area plays a critical role in the global atmospheric circulation.
For the forcing of the circulation within the SCS the Monsoon plays an important role. Both, the wind stress itself, as well as the wind stress curl are responsible for the mean SCS circulation. Only at the northern and western boundary also the LS transport influences the circulation.
The AMS is the most significant one and extends from the western Indian Ocean to the

western Pacific (Lim et al. 2002). Depending on the geographical area it can be divided into local systems: Indian Monsoon, Southeast Asian Monsoon (SEAM) and East Asia Monsoon (EAM). The South China Monsoon is sometimes seen as a part of the SEAM or as a system of its own, located in the west of the SEAM. In the west it is connected with the Indian Monsoon and to the north with the East Asian Monsoon. There are strong connections to the Australian Monsoon System in the south.

Some investigations described most of the SCSM as a part of the AMS. Only the South Chine Sea Monsoon Experiment (SCSMEX) examined the SCSMS alone (Ding et al. 2004). This project concentrated particularly on the Summer Monsoon and the effects on the Asian continent. On average the Summer (Winter) Monsoon in the SCS starts in May (November) and ends in September (February).

Generally, the strength of the Monsoon east off Vietnam is about 8 m/s during winter and about 6 m/s during summer. The inter-annual variability of the wind speed is about 2 m/s (1 sigma) higher in summer than in winter. Between the two monsoon phases, during inter-monsoon, there are phases of low wind speeds (< 4 m/s). In the area southeast of Vietnam the monsoon has a special feature. There is a low level jet as well in boreal winter as in boreal summer, the Vietnam Low Level Jet (VLLJ). This is comparable to the Somali Jet (SJ), which was found by Findlater (1969). The SJ is the narrow southwesterly surface wind in the western Indian Ocean with a two-day average speed greater than 12 m and a cross-stream dimension of about 200 km (Halpern and Woiceshyn 1999).

While the SJ has been described by different researchers, only Xie (2003) described the VLLJ, who pointed out the importance of the upwelling at the coast of Vietnam for the behavior of the monsoon.

2.2.1The Winter Monsoon

The most important driving force for the monsoon is the strong temperature contrast of the East Asian continent and the sea in the western Pacific and the Maritime Continent (Zhang et al., 1997). Deep convection takes place in the equatorial area. The main heating sources are near the equatorial western Pacific, and in the southern part of the SCS. The latent heat release, associated with intense convective precipitation, induces the local Hadley Circulation in the meridional direction. Furthermore, the Asian Winter Monsoon is dominated by a strong anticyclone over Siberia and northern China, resulting from a cold dome. Ding and Krishnamurti (1987) and Ding (1990) investigated the genesis and development of the Siberian high. The intensity of the Siberian cold dome is affected by strong radiative cooling, the large-scale descending motion of the Siberian high, a strong

local Hadley Circulation and the persistent cold-air advection throughout the troposphere. The excessive radiative cooling, coupled with the advection of cold air and the blocking effect of the Tibetan Plateau to the southwest, cause the build-up of a huge mass of cold air over northern China. According to Chang and Lau (1980) and Lau et al. (1983) the passages of upper flows triggers the strong anticyclone, which often moves southeastward and enhances the pressure gradient. This has the consequence, that the cold air suddenly bursts out over the SCS. This is called “cold surge” (Lau and Lau, 1984; Chen et al., 2002). Lim and Chang (1981) showed that the characteristic of a cold surge is like a surface gravity wave. A cold surge can be paraphrased by a steep rise of surface pressure, a sharp drop of the surface temperature, and strong dry and cold surface wind. The outburst happens at intervals between several days and weeks. Typically two cold surges occur per month (Lau and Chang, 1987; Zhang et al., 1997, Chang et al., 2004). The southern part of the SCS winter monsoon is driven by a deep convection area over the Maritime Continent and the southern SCS. On synoptic timescales the deep convection is influenced by the cold surges, on intra-seasonal timescales by the Madden Julian Oscillation (Madden and Julian, 1971; Chang et al., 1979; Chang and Lau, 1982) and on annual timescales there are indications of a tele-connection with the ENSO (El Nino Southern Oscillation). After an El Nino, the strength of the winter monsoon is decreased (Rasmusson and Carpenter, 1982), primarily because of a shift of the convective system from the Maritime Continent towards the dateline (Lau and Chan, 1983 a, b). Weaker convection in the southern part of the SCS result in a weaker Hadley Circulation, which leads to weaker Cold Surges.

According to its strength the Winter Monsoon can be divided into three modes: First, the cold surges, with wind speeds of more than 20 m s^{-1} southeast of Vietnam. Second, something like a monsoon base level with speeds between 5 m s^{-1} and 10 m s^{-1}. Third, sometimes complete monsoon breaks occur. Then the direction of the wind is mainly from the east, with speeds of less than 5 m s^{-1}. The wind field during such phases is more similar to the wind field during inter-monsoon.

The winter monsoon in the SCS is not homogeneous, but it builds a curl. Figure 2.1 illustrates the wind stress and the wind stress curl of the winter monsoon during a Cold Surge. Due to the enhanced wind stress in the central SCS and in the Luzon Street the curl is negative in the northwestern SCS and positive in the southeast. The strongest positive curl is south of the Luzon Street, the most negative is southeast off Vietnam.

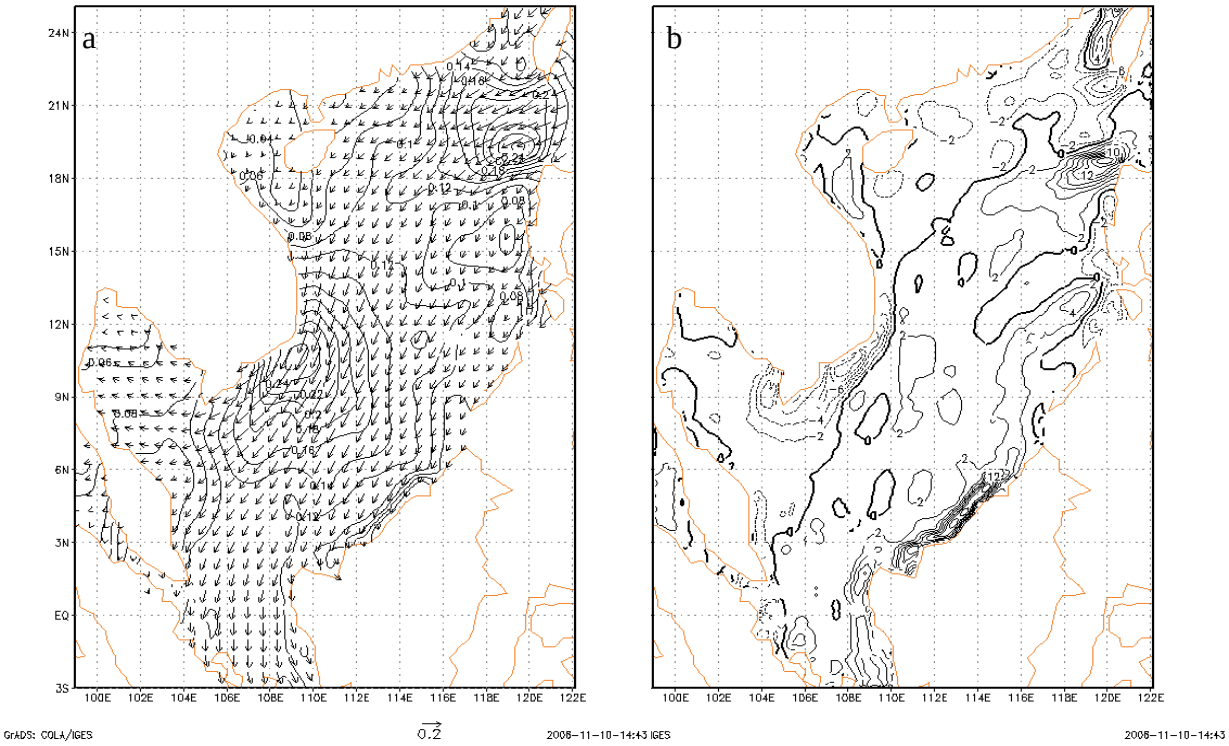

Fig. 2.1: Wind stress in the SCS during a Cold Surge, (a) wind stress vectors with wind stress magnitude contours and (b) wind stress curl. The wind stress reference vector is 0.2 PA, the contour interval in (a) is 0.02 PA. The wind stress curl contour interval is 2 x 10^{-8} m^{-1}.

2.2.2The Summer Monsoon

At boreal spring the convection zone over the Maritime Continent and the southern SCS starts to move northward. In May it suddenly jumps to the northern SCS and southern China (Lau and Yang 1997; Lau et al. 1998). At the same time the temperature gradient south of the Tibetan Plateau reverses (Yanai et al., 1992, Li and Yanai, 1996). This both together resulting in the onset of southwest winds in the SCS. This fast change in atmospheric situation combined with the reversal of the Hadley Circulation in May is seen as a major factor of the spring transition of the planetary-scale circulation by many authors in the last years (Matsumoto 1992, Lau and Yang 1997).

The specific situation of the SCS, which is surrounded by mountain ranges and has a

complex sea surface temperature distribution, results in some distinctive features in the SCS summer monsoon. There is an east-west gradient of the highly reflective clouds (HRC) in the central SCS. Wang and Wu (1997) found the HRC frequency off the coast of Vietnam is only about 30% of that in the eastern part. They suggest a sinking motion of air in the west and an upward motion in the east, resulting from the sea surface temperature differences. According to Wang and Wu this might drive a longitudinal circulation cell, a zonal overturning circulation, like it is present in the Indian Ocean (e.g. Trenberth, 1999, Meehl et al., 2003) or the Walker Circulation in the Pacific (e.g. Zimmermann et al., 1988, Geisler, 1981).

Like the winter monsoon, the summer monsoon is not homogeneous. Due to the enhanced wind stress in the central SCS the curl is positive in the northwestern SCS and negative in the southeast. The strongest curl is that off the coast of central Vietnam. Figure 2.2 shows the wind stress and wind stress curl offshore south Vietnam during July 2004. The figure illustrates the VLLJ.

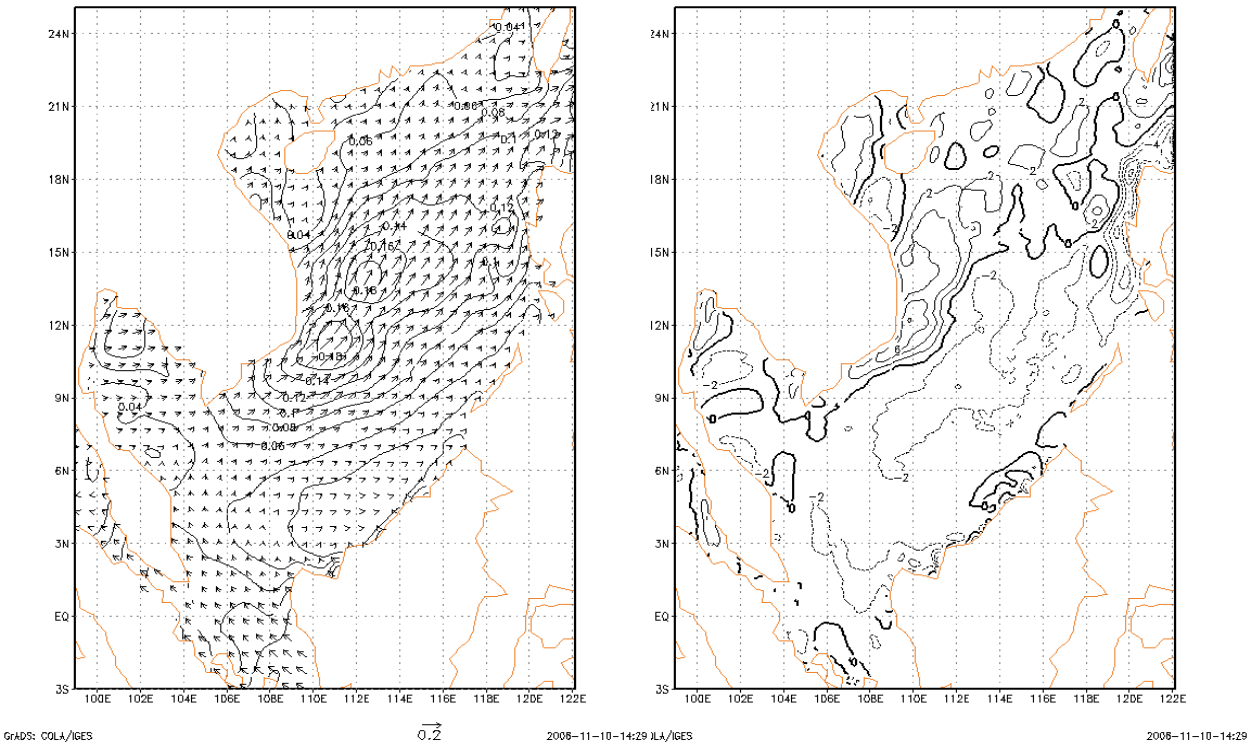

Fig. 2.2: Wind stress in the SCS during July 2004, (a) wind stress vectors with wind stress magnitude contours and (b) wind stress curl. The wind stress reference vector is 0.2 PA, the contour interval in (a) is 0.02 PA. The wind stress curl contour interval is 2 x 10^{-8} m^{-1}.

The variation of the SCS summer monsoon was subject of many studies. The intra-seasonal oscillation of the SCS summer monsoon is dominated by two timescales: a 10 to 20 day

rhythm due to convection activity and a 30 to 60 day rhythm due to the MJO. These two oscillations controlling the active and break phases of the Monsoon. However, after analyzing the temporal structure of the SCS summer monsoon Wang and Wu (1997) came to the conclusion that the variability is peculiar and different from the rest of the ASM. The deep convection over the SCS features the largest year-to-year variability compared to other tropical monsoon regions. They even found no dominant periodicity on synoptic to intra-seasonal timescales in climatological mean sense, which means that the weather rhythm changes from year to year and is highly non stationary. On intra-anual timescales there is a tele-connection with the ENSO, after an El Nino during winter, the summer monsoon is not as strong as in non-El Nino years. However, during ENSO neutral phases, this relationship disappears. By investigating the relationships between the ENSO and the 30 to 60 day oscillation, Lu and Ren (2005) found that the ENSO modulates the oscillation.

2.3 The seasonal circulation of the South China Sea

The South China Sea was the subject of many investigations. In-situ measurements, as well as many studies that analyzed satellite data took place. Moreover a lot of modeling studies took place. Due to the research goal of studying the coastal upwelling, this thesis focuses on the surface, subsurface and, in some works, the intermediate circulation of the SCS.
The first investigations were carried out by Dale (1956) and Wyrtki (1961) in the NAGA Report. They mainly deduced the surface currents from ship drift data and prevailing wind data. Both publications suspect the monsoon wind stress to be the main cause for the surface circulation. Xu et al. (1982) and Tomczak and Godfrey (1994) summarized the historical observational data from 1921 to 1970. From a first view it can be said that the general SCS surface circulation is anticyclonic during summer but cyclonic during winter. During the northeast monsoon a strong boundary current develops along the Vietnamese coast. Apparently, the northeast monsoon moves the surface water northwestward, resulting in some compensatory southward movements in the western SCS. In winter this results in a strong cyclonic circulation in the western basin. The results of the NAGA Report show a strong westward intensification, with current velocities of more than 75 cm/s. During the winter monsoon this southward boundary current follows the shelf-edge from 18°N to 5°N as the eastern part of the cyclonic circulation. During the southwest monsoon, represented by values from August, the circulation in the NAGA report is strongly anticyclonic in the southern basin, building a strong western boundary current along the Vietnamese coast up to 12° N. At 12° N it separates from the coast. The flow is building a strong eastward jet, which partly recirculates to the south. The main surface current leaves the SCS through the

LS and the Taiwan Street. North of the point of separation a cyclonic eddy is visible, building a coastal upwind current along the Vietnamese coast.

Later studies, like that from Qu (2000), verify in principle the circulation from the NAGA Report. Qu (2000) used the data from the world ocean atlas from Levitus(1994) to extract the SCS circulation.

Chu and Li (2000) used the GDEM data set to extract the circulation of the subsurface and the circulation of the intermediate layer (150m) on an isopycnal surface. GDEM is the US Navy's global climatological monthly mean temperature and salinity data set. Using the p-vector method (Chu, 1995, Chu et al., 1998a, Chu et al., 1998b) Chu and Li (2000) found a strong intrusion of the Kuroshio into the SCS during winter and an anticyclonic circulation in the Luzon Strait during summer. In the intermediate layer the circulation is always cyclonic the whole year. Due to the westward intensification a strong southwestward and a southward boundary current emerge at the shelf edge of China and of Vietnam respectively. One explanation for the circulation always being cyclonic in the intermediate could be the distribution of the wind curl over the SCS. The curl is largely positive in the annual mean.

Shaw et al.(1999), Wu et al. (1998), Wang, et al. (2000), Morimoto et al. (2000) and Hwang and Chen (2000) extracted the circulation from the sea surface elevation in the SCS using the Topex/Poseidon altimeter data. The bimonthly circulation of the SCS, deducted from sea surface heights, can be described as follows: In January and February the circulation is completely cyclonic, represented by two eddies, the stronger one in the north, covering the area from 14° N to 23°N and 110° E to 120° E, the weaker one in the southwest deep basin of the SCS from 8° N to 11° N. Between these eddies there is a bridge of higher sea surface heights near the western boundary of the SCS at 12° N. In the southeastern part of the SCS, near the Kalimantan Isle, there is an anticyclonic eddy.

From march to April the cyclonic circulation weakens, particularly the bridge between the two cyclonic eddies increases to an anticyclonic eddy. In April and May this eddy is the main dynamical area in the SCS. During the beginning of the southwest monsoon in June the whole SCS becomes one anticyclone, except the northwesternmost part of the deep basin. In July, August and September a cyclonic eddy develops offshore Vietnam, driven by the curl of the wind stress and the recirculation due to the northeastward-moving surface water, induced by the wind stress. The westward intensification let the western part of the eddy rise.

Between the northern cyclonic eddy and the anticyclone in the south from 11° 30' N to 12° N a strong offshore current is established. In October and November the cyclone increases in strength, while the anticyclonic eddy in the south is becomes weaker. During the rest of the year the winter cyclonic circulation is established. In the southeast the anticyclonic circulation is stronger than at the beginning of the year. The publications cited before come to the conclusion that the wind stress curl is the main driving force of the circulation in the

deep basin of the SCS except near the LS. The variation of the circulation in the central part of the basin can be associated well with the wind stress curl. Wang et al. (2003) investigated in the mesoscale circulation of the SCS. They extracted a lot of small eddies from satellite data, mostly anticyclonic, moving from the east to to west through the SCS.

Wang (1985) was the first who developed a numerical model to simulate a steady state of the SCS surface current fields. Pohlmann (1987) applied the first prognostic baroclinic three-dimensional circulation model to simulate the SCS circulations during the winter and summer monsoons, more or less the same did Mao et al. (1992). Li et al. (1992a, 1992b), Li et al. (1994), Liu and Su (1993), Su and Liu (1992), Zeng et al. (1989) and Zeng et al. (1992) used two-dimensional numerical models to calculate the monthly or seasonal mean SCS circulation. Although all these models have a spatial resolution of only about 50km, they reflect the mean seasonal circulation, with a mean cyclonic circulation in winter and a mean anticyclonic circulation in summer.

The first three-dimensional model, running over a longer timescale, was that of Shaw and Chao (1994). Wu et al. (1998) calculated an EOF-analysis with their model results. They confirmed the preceding results, saying that the circulation reflects the seasonal change of the wind stress and the wind stress curl. They reproduced well the southward boundary current during winter and the northward boundary current during summer, but the current velocities are less than half of the findings of Wyrtki (1961). However, the typical summer dipole structure can not be seen in their model, but Shaw and Chao (1994) yielded a subsurface counter-current that started in September. The Vietnam dipole is also not present in the model of Isobe and Nambe (2001). Nevertheless, their models do show a strong anticyclonic gyre in the southern part during August, building a northward boundary current at the edge of the Sunda Shelf, separating offshore at about 12°N. Oddly, the anticyclonic gyre doesn't comply with the wind stress curl, the zero line of which is at 9° N. Actually the curl is expected to produce a gyre 200 km farther to the south (Xie, 2003).

On inter-annual timescales the circulation of the SCS is influenced by the ENSO. During the onset of an El Nino the winter monsoon weakens and as a consequence the SCS circulation. Especially the northern cyclonic gyre diminishes (Chao et al., 1996a). Because of the influence of the winter circulation on the summer circulation there is still an influence during the southwest monsoon.

The assimilation of altimetric data into the model of Shaw and Chao, by Wu et al. (1999) shows an interesting effect. The circulation of the model now better resembles the circulation deducted from in-situ measurements or altimetric data. Wu et al. (1999) came to the conclusion that, using assimilation techniques, they could avoid the inadequate spatial resolution of the NCEP data and the uncertainness of the boundary conditions. The outstanding result of their experiment with data assimilation is the appearance of the Vietnam dipole, with a clearly bounded jet in between.

From the models reviewed so far one can conclude that the general circulation of the SCS is driven by the monsoon winds and its curl. However, some parts of the circulation, like the Vietnam dipole, are simulated insufficiently, as seen in the assimilation experiment of Wu et al. (1999). The influence of the LS transport on the circulation is not clearly known yet. Chu et al. (1999) advert that at the western boundary the LS transport does play an important role.

According to Metzger and Hurlburt (1996) and Chen and Wang (1998), three components of the Kuroshio in the LS can be identified: One branch of the Kuroshio flows directly north and passes the street. Another part of the Kuroshio flows into the LS creating an anticyclonic loop current in the SCS and then leaving the SCS in the north of the LS. Third, an intrusion current forms and penetrates along the continental margin. This is evident in hydrographic data, analyzed by Shaw (1991). In the model of Metzger and Hurlburt (1996) in the average, this intrusion current flows along the continental shelf towards the western boundary and then turns to the south. At about 12° N a part of this current turns eastward, with a maximum intrusion in summer and a minimum in winter. However, this contradicts the findings of Wyrki (1961) and Centurioni et al. (2004) who found only an intrusion during winter. An explanation for this contradiction may be the fact that Wyrki (1961) used ships-drift data and Centurioni and Niller (2003) used satellite traced drifters. Thus, both flow estimations were conducted close to the surface, whereas the upper layer in the model of Metzger and Hurlburt (2001) has a thickness of 200m. The transports from Xue et al. (2004) resemble those of Metzger and Hurlburt (2001), however, they are strongest in September and October, which means a time lag of 2 months. From observations Chen and Huang (1996) noted an all-the-year inflow in the upper layer, and an outflow at depths between 350 m and 1350m. Qu (2000) came to the same conclusion after analyzing the properties of the water masses in the SCS.

In contradiction to former estimates (e.g. Wyrki, 1961), Metzger and Hurlburt (1996, 2001) and Hu et al. (2000) could verify with model experiments that the intrusion is not a result of the monsoon wind in the SCS. Rather, the intrusion is a result of the large-scale forcing in the western pacific. From the aspect of modeling, the second important influence on the LS transports is the model geometry. Chen and Wang (1998) pointed out that the different stratification of the SCS water masses and the West Pacific water masses influences the LS transport. Metzger and Hurlburt (1996) could verify with their experiments that the LS transport is not driven by local wind, nor by the wind stress in the central SCS, but that the LS transport is related to the tropical pacific gyre. Metzger and Hurlburt (2001) used a technique to separate the effect of direct atmospheric forcing and the effect of non-deterministic mesoscale flow instabilities, the results of which indicated that in the LS and the northernmost part of the SCS the non-deterministic circulation plays a more decisive role than the wind driven circulation. Referring to these results they concluded that the

intrusion of the Kuroshio is non-deterministic.
The LS can influence the water masses in the SCS, greater water masses from the Kuroshio entering the SCS result in warming of the SCS. Moreover Qu et al. (2004) suggested that the LS transport may be responsible for the impact of the ENSO on the SCS. They calculated a significant correlation between the LS transport and the Southern Oscillation Index of 0.63. In years of an El Nino, the transport of the Kuroshio is weaker, due to the northward shift of the North Equatorial Current in the pacific. This results in a stronger intrusion into the SCS, resulting in a higher heat content in the SCS.
Hu et al. (2000) investigated the behavior of Rossby waves in the South China Sea, using satellite altimeter data. Sometimes Rossby waves propagate through the LS and influence the circulation in the SCS. Yang et al. (2002) deducted from models that the forcing of the SCS is mainly induced by the effect of the wind stress curl on baroclinic Rossby waves, which cross the SCS over a time of several months.
Metzger and Hurlburt (2001) found that alee of the Kuroshio intrusion in the LS there is a region of eddy shedding. Many of these eddies move westward and interact with the eddies in the central SCS. It is not uncommon that they reach the western boundary. Then they move to the south, in the direction of the coastal trapped waves, and amplify.

2.4 Upwelling in the South China Sea

Coastal Upwelling can be found at seven locations in the SCS: At the Chinese coast, in the Taiwan Street, south of the Luzon Street, around Hainan Island, at the central Vietnamese coast and at the southern Vietnamese coast and in wintertime at the edge of the Sunda Shelf. Huang (1994) notes that Chinese scientists found current-induced upwelling off east Guangdong in winter.
The Taiwan Street upwelling was covered in several investigations. Tang et al. (2002) and Hu et al. (2001) investigated in this area with shipboard measurements and with sea surface temperatures from satellite measurements. Among some smaller upwelling regions, there are two main upwelling areas in the Taiwan Street: coastal upwelling near Dongshan Island, and in the center of the Taiwan Street, southeast of the Taiwan Bank. The upwelling near Dongshan Island is present during summer and can extend up to 80 kilometers offshore. The upwelling southeast of the Taiwan Bank is not a coastal upwelling but important, because of its appearance in winter and summer. Cai and Lennon (1988) conducted model studies in the Taiwan Street, concentrating on upwelling, and found a complex interaction between stratification, the main circulation of the SCS, bathymetry and the direction and persistence of the wind field. Their results suggest an upward displacement of 18 m of the second layer

after a wind stress forcing over 15 days. An experiment with a penetration of the Kuroshio into the Taiwan Street enhanced the upwelling. The current-induced upwelling is about 5/6 the strength of the wind-induced upwelling in summer. In winter they can produce the upwelling in the Taiwan Street only with the Kuroshio and suggest that the Kuroshio controls the upwelling process.

During summer, upwelling is present at Hainan Island (Chu, 1999). Huang (1994) reported that, according to Chinese findings, at the eastern Hainan Island upwelling occurs also in winter, which contradicts the explanation of a monsoon-induced upwelling. There are no studies about the physical process in this upwelling region, but it will be subject of future research of the Institute of Oceanography, Hamburg (Pohlmann, personal reference).

Shaw et al. (1996) analyzed the upwelling at the northern edge of the Luzon Island with an in-situ shipboard measurements, the Levitus Ocean Atlas and modeling studies. They could not verify a coastal upwelling induced by local alongshore wind; especially there is no coastal downwind jet. Hence, they suggested a remote-forced upwelling due to the basin-wide circulation. The center of the upwelling is more than 100 km offshore and could be induced by a converging undercurrent. However, it should be pointed out that at this spatial position a strong positive wind stress curl exists, which drives an upwelling due to Ekman-pumping. Yang and Liu (2003) found vertical velocities of about 10 m/day in 500m water depths due to Ekman-pumping.

The next section deals with the upwelling at the Vietnamese coast.

2.5 The Vietnam Upwelling Area

The Vietnam Upwelling Area (VUA) is located off south-central Vietnam, between 10°30'N and 12°N. The bathymetry of this region is illustrated in fig. 2.3. The upwelling can be found in the area north of the Sunda shelf, where the shelf completely deforms its geometry. In this region the shallow and wide shelf exchanges to a deep and narrow shelf, in two steps the mid-shelf depths deepen from 40 m in the south, to 180 m in the north. In fig. 2.3 the brown dashed lines represent the crestline of the beginning Sunda shelf and the crestline of an asymmetric ridge off Cam Ranh. These crestlines are located directly south of the deepening of the bathymetry. Between these two rises a canyon-like structure can be found.

In the northernmost region a clear defined shelf edge is present. At 11°30'N, in depths of more than 300 m, the shelf widens significant, which yields a undefinable shelf edge in this region.

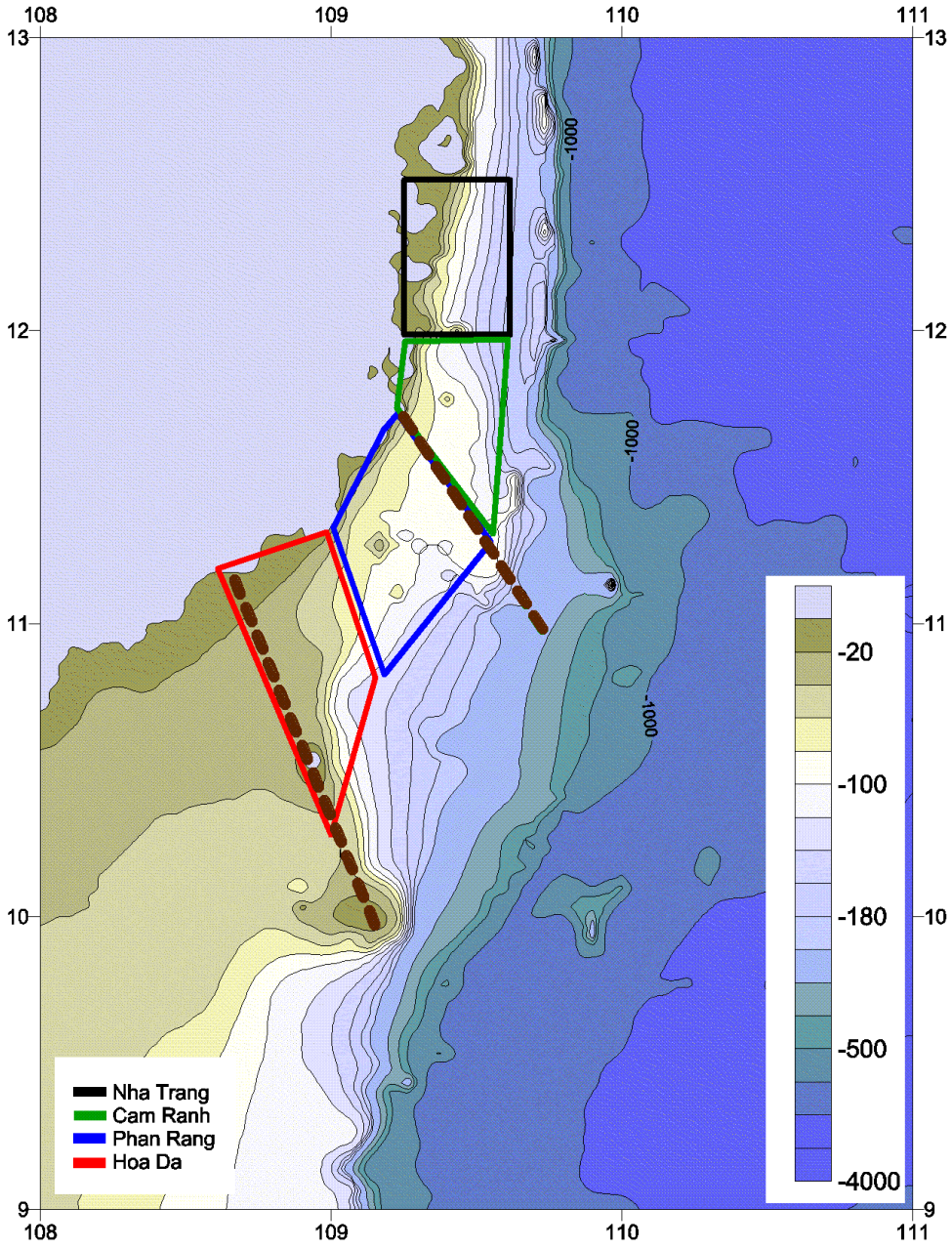

Fig. 2.3: Bathymetry of the VUA: The brown dashed lines display the crestline of the Sunda shelf and a ridge near Cam Ranh, the colored boxes represent the four regions of the upwelling area.

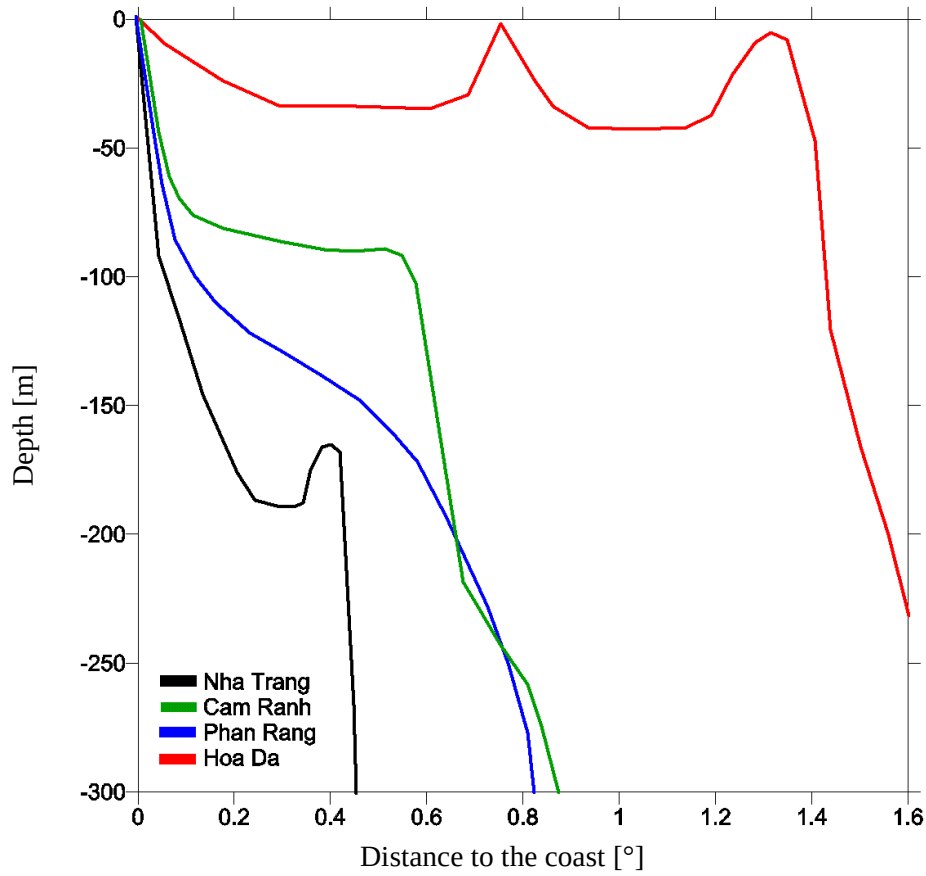

Fig. 2.4: Sections perpendicular to the coast of the bathymetry in the four different regions.

Due to the bathymetry, the VUA can divided into four regions, which are shown with the boxes in fig. 2.3. Northernmost, in the region off Nha Trang, a deep shelf and a homogeneous bathymetry in the alongshore direction characterises the geomorphology. The region off Cam Ranh represents the first step of the alongshore change in the shelf bathymetry north of the ridge. The canyon-like structure is the main morphological feature of the region Phan Rang. The southernmost region, off Hoa Da, is formed by the alongshore slope at the margin of the Sunda Shelf. Fig. 2.4 shows sections of the bathymetry perpendicular to the coast. The sections discover the change of the shelf-bathymetry and illustrate that the shelf modifies completely its morphologic structure.
Table 2.1 describes the four regions of the VUA.

Region	Geomorphology	Mid-shelf depth	Shelf width
Nha Trang	homogeneous in the alongshore direction	180 m	50 km
Cam Ranh	strong alongshore slope, ridge	90 m – 180 m	70 km
Phan Rang	canyon-like structure	90 m – 120 m	80 km
Hoa Da	strong alongshore slope, margin of the Sunda shelf	40 m – 120 m	150 km

Table 2.1: The four regions of the VUA

The upwelling at the Vietnamese coast is mentioned by many publications on the SCS circulation. But only some investigations concentrated on the upwelling phenomenon along the southern Vietnamese coast, using remote-sensing data. By this means Xie (2003) formulated an index representing the strength of the cold filament to the east of the upwelling area and found a good correlation with the ENSO-cycle with a time lag of about 6 months. Kuo et al. (2000, 2004) observed the upwelling off Vietnam using the Advanced Very High Resolution Radiometer (AVHRR). Although most of the time clouds cover the upwelling area, Kuo was able to detect a cold jet moving eastward between 11°N and 12°N. Chao et al. (1996a, 1996b) cover upwelling at the margin of the Sunda Shelf south of Vietnam in winter. Referring to the bathymetry and the basin-wide circulation, Chao et al. (1996a, 1996b) suggest an uplift of the deep water masses.

3
Methods

Methods of the physical oceanography always have to be developed according to the examination aim. The spatial and temporal scale are decisive for the choice of the means. Upwelling is usually a mesoscale process, as off the coast of Vietnam. Nevertheless it is influenced by large scale hydrodynamic processes. Building on recognized theories about upwelling processes, for the examination of the Vietnam Upwelling, remote sensing data, in situ measurements and also modelling studies are used. The aim of the combination of these methods should be the extraction of information about the upwelling process, including its physical processes and the variability of the vertical velocities and transports.
Every method has certain restrictions regarding the extraction of information. While remote sensing data only give information about the surface of the sea, in situ measurements can give information on the whole water column. However, remote sensing data are available over longer time scales with a resolution of about three to ten days. In contrast to that, in-situ measurements can provide only information for one point in time. In contrast Hydrodynamic models provide informations for the whole water column over longer times.

3.1 HAMSOM – Model description

To simulate the horizontal and vertical velocities in the SCS, the numerical model HAMSOM is used. HAMSOM was first set up in the mid-eighties by Backhaus (Backhaus, 1983; Backhaus, 1985). HAMSOM is designed to allow simulations of both oceanic and coastal and shelf sea dynamics. It is an eddy-resolving, hydro-thermodynamical model which uses a free surface. HAMSOM was used in a lot of projects, simulating several shelf seas worldwide. (Backhaus and Hainbucher, 1987; Alvarez Fanjul, 1997; Backhaus et al, 1991; Pohlmann, 1991; Becker et al, 1999; Harms, 1992; Carbajal, 1993; Pohlmann, 1996;

Hainbucher and Backhaus, 1999; Harms et al., 1999; Harms et al., 2002; Harms et al., 2000; Harms, 1997; Huang, 1995; Schrum, 1994; Schrum, 1997; Schrum, 2000; Stronach, 1993). HAMSOM has also been coupled with ecosystem models (ECOHAM, ERSEM), an atmospheric model (REMO) and both Lagrangian and Eulerian models for sediment transport (Harms, 2001; Harms and Karcher, 2001; Harms and Povinec, 1999; Luff and Pohlmann, 1996, Lenhart et al., 1996).

The numerical scheme of HAMSOM is defined in z-coordinates on an Arakawa C-grid. The governing primitive equations for shallow waters combined with the hydrostatic assumptions are implemented. The equations can be found in Pohlmann (1991). In order to calculate the Coriolis term with a second order accuracy in time, a rotational matrix is used. To solve the free surface problem, the vertical transfer of momentum and water mass properties are calculated. To reach stability even for greater time steps, several terms are solved implicitly. These are equations for the vertically integrated continuity and the barotropic pressure, the combination of which describes the surface gravity waves. The vertical shear stress and the diffusion terms are calculated implicitly as well. A non-linear implicit friction law as well as the full kinematic boundary condition is applied at the bottom.

An explicit formulation is used for the advective terms of the momentum equation and for the transport of temperature and salinity. To conserve eddies and frontal structures, an Arakawa J7 algorithm is implemented.

To parameterise horizontal sub-scale processes, a Smagorinsky Scheme is used to calculate a horizontal turbulent exchange. This allows for non-constant coefficients, dependent on the horizontal shear stress. The Smagorinsky Scheme will be discussed later in a section of its own. To calculate the vertical turbulent viscosity coefficient, the approach of Kocherin (1987) was implemented by Pohlmann (1996). The vertical viscosity influences the depths of the surface and bottom layer. As will be shown later, these layers influence the upwelling processes, hence the estimation of the vertical turbulent viscosity has to be discussed here.

For each layer on each zeta-node, the coefficient of turbulent viscosity is calculated with:

$$A_v = (c_{ML} \cdot D_M)^2 \cdot \sqrt{\left(\frac{\delta v}{\delta z}\right)^2 - \frac{N^2}{S_M}}$$

The formula includes $c_{ML} \approx 0.05$, a constant given by Kochergin (1987). The magnitude of the constant was found through physical and empirical assumptions. D_M is the depth of the turbulent mixed layer at the surface as well as at the bottom.

In the equation of the vertical turbulent viscosity coefficient A_v we see the Prandtl number S_m :

$$S_M = \frac{Ri}{0.725 \cdot (Ri + 0.186 - \sqrt{Ri^2 - 0{,}316 \cdot Ri + 0.0346})}$$

The Richardson Number (Ri) is the ratio between the buoyancy frequency and the vertical shear of the current:

$$Ri = \frac{N^2}{\left(\frac{\delta v}{\delta z}\right)^2 + \left(\frac{\delta u}{\delta z}\right)^2}$$

In this equation, N is the buoyancy frequency:

$$N^2 = \frac{-g}{\rho_0} \cdot \frac{\delta \rho}{\delta z}$$

Here ρ_0 is a reference density, $\delta \rho / \delta z$ is the vertical density gradient and g the gravitational acceleration.

If $Ri < 0.23$ then turbulent mixing is possible. This behavior is used to determine the values of D_M. This turbulent closure scheme allows a variable vertical turbulent viscosity, depending on the vertical velocity shear and on the stratification. In detail, the vertical eddy viscosity is enhanced by stronger vertical shear and reduced by stronger vertical stability. This allows for realistic turbulent layers at the surface as well as at the bottom.

The used version of HAMSOM allows for a parallel run on NEC SX-6 series multi-CPU vector supercomputers. The model was calculated on four CPUs. For this, the code of the model was parallelised with a domain splitting method. This means the model domain was split in four domains in the north-south direction. The relevant variables are exchanged between the domains at every time step. In this configuration approximately 1500 hours CPU time were required to simulate one year.

3.2 The SCS model and Boundary conditions

To simulate the vertical and horizontal currents as well as the temperature and salinity in the VUA, the model was adapted to the SCS (HAMSOM-SCS).

The goal of this thesis is the analysis of the upwelling off the coast of Vietnam. To achieve this aim, the entire SCS was covered by the model according to the findings of Metzger and Hurlburt (1996), Metzger and Hurlburt (2000), and Qu et al. (2004). They found the impact

of the Luzon Strait Transport (LST) to be of importance to the circulation and the heat budget of the SCS. Especially the western boundary currents are influenced by the LST: About 40% of the variability of the western boundary currents result from the LST. Qu et al. note that the LST is an important process conveying the impact of the ENSO to the SCS. The horizontal resolution was derived according to Metzger and Hurlburt (2001) who analysed the sensibility of the model to the resolution of the LST. In accordance with their findings, a resolution of 4' x 4' or O(7 km x 7 km) is appropriated. The resolution is adequate to represent the morphological structures in the VUA and in the Luzon Strait.

This leads to a model size of 422 points in the north-south direction and 348 points in the east-west direction. The vertical resolution is set to 36 layers, with a vertical layer spacing of 5m for the upper 50m, 10m between 50m and 160m depth and beneath a spacing of 20m increasing to a maximum spacing of 1000m, with the deepest layer at 4000m ending at. As a result of this spacing, the model contains both a well resolved mixed layer and shelf edge and on the shelf even a well defined bottom layer.

Due to the availability of the forcing data sets and the restrictions on the run time, the simulation time of the model was restricted to a period from 01.10.2001 to 30.09.2005. The first half-year is taken as spin-up time, which yields the calculation of three winter and four summer situations. Talbe 3.1 shows a overview over the used forcing data sets.

Variable	**Unit**	**Source**
U wind component	m s^{-1}	http://airsea.jpl.nasa.gov/DATA/QUIKSCAT/wind/
V wind component	m s^{-1}	http://airsea.jpl.nasa.gov/DATA/QUIKSCAT/wind/
Sea Level Pressure	Pa	http://www.cdc.noaa.gov/cdc/reanalysis/
Sea Surface Temperatures	° C	ftp://ftp.ssmi.com/tmi/
Dynamic Hights	cm	http://las.aviso.oceanobs.com/las/servlets/dataset
River discharges	$m^3 s^{-1}$	http://www.grdc.sr.unh.edu/
Temperatures at open boundaries	° C	Boyer (1998a, 1998b , 1998c)
Salinity at open boundaries	psu	Boyer (1998b, 1998v)

Table 3.1: Forcing data at the surface and boundary conditions

Initially, the temperature and salinity fields in the interior and at the boundaries were prescribed using the climatological monthly mean (Boyer, 1998).

The model includes five lateral open boundaries: the Taiwan Street, the Luzon Strait, the Mindoro Street, the Malaca Street and the Kalimanta Street. At the lateral open boundaries

the model sea surface elevations are prescribed by observations from merged satellite data (http://las.aviso.oceanobs.com/las/servlets/dataset). The dataset contains observations from several satellites: Jason-1, Topex/Poseidon, Envisat, GFO, ERS-1 & 2 and Geosat. Due to the temporal resolution of 3.5 days and the spatial resolution of O(20' x 20'), mesoscale eddies are available in the dataset.

The temperature and salinity at the open lateral boundaries were prescribed using the climatological monthly mean at the inflow regions and a radiation condition at the outflow regions. To prevent the model from showing instabilities due to the differences between the satellite data and sea surface elevation from the climatological temperature and salinity data, the climatological data was adjusted according to the satellite data. To achieve this, the sea level elevation is calculated from the temperature and salinity field as a superposition of the inverse barometric effect and the dynamic height. Using an iteration scheme, the temperature and the salinity field are changed through upward or downward vertical mixing, until the difference between both elevations is less than 5 mm. This method allows for a dynamic climatology at the boundaries. Moreover, it includes the behavior of mesoscale eddies in the Luzon Strait, which are important for the variability in the LST. The transports driven by the outflow and inflow are calculated by the sea surface elevation with the condition of a zero gradient normal to the boundary.

At lateral solid boundaries, river discharge of the five largest rivers are implemented with a climatological monthly mean. These rivers are the Pearl River at the Chinese coast, the Red River in the gulf of Tonkin, the Mekong at the coast of southern Vietnam, the Jiulong River near the Taiwan Street and the Chao Phraya in the Gulf of Thailand. The datasets are taken from the Global Runoff Data Center (GRDC) runoff composite fields (http://www.grdc.sr.unh.edu/). Due to the lack of discharge data, many small rivers could not be included in the model. Also, the use of climatological discharge data may lead to inaccurate salinity distributions. However, the inaccuracy of the used discharges influences not the general circulation of the model.

As an example, Fig 3.1 shows the discharge of the Mekong.

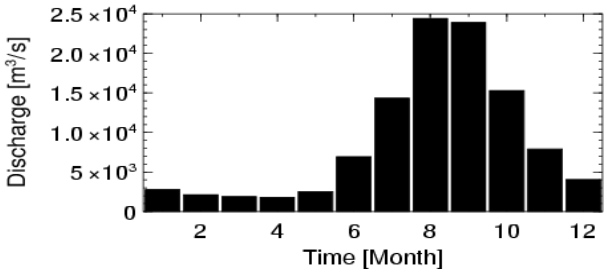

Fig. 3.1: Climatological monthly mean river discharges from the Mekong (http://www.grdc.sr.unh.edu/).

At the sea surface, the model is forced by wind stress calculated from the Quickscat Satellite 10m wind field observations (http://airsea.jpl.nasa.gov/DATA/QUIKSCAT/wind/) and with the NCEP reanalysis sea level pressure field (http://www.cdc.noaa.gov/cdc/reanalysis/). The use of the satellite observations permit the implementation of a realistic wind stress field with a higher spatial resolution than the wind field of the NCEP reanalysis. Due to the coarse resolution the low pressure level jet south-east of Vietnam is not well resolved in the NCEP reanalysis data, thus the curl of the wind stress is not realistically represented here. Hence, the wind stress data are derived from the observations by the scatterometer SeaWinds on space mission QuikSCAT of the National Aeronautics and Space Administration (NASA) which provide a resolution of 0.5° x 0.5° twice a day.

The heat flux calculations at the sea surface with components of the NCEP reanalysis and a bulk formula from Schrum and Backhaus (1999) were tested. However, the test illustrated that the variation of the sea surface temperature changed in a non-acceptable manner. It was concluded that this displacement is mainly caused due to the fact that the parameters in the bulk formula are derivied for tempered zones and not for the tropics.

Due to this, the heat fluxes were substituted by assimilating sea surface temperatures from satellite observations. This will be illustrated in a section of its own.

The main model experiment is named E0. Aside from E0, three shorter experiments were conducted. E1 simulates only one week with homogeneous wind stress to test the spin-up of the upwelling processes. E2 calculates several weekly spin-ups in the summer 2004 to estimate the influence of the local wind stress field. E3 calculates the circulation without discharge from rivers, to analyse the influence of the Mekong on the vertical velocities. A overview of the experiments is given in Table 3.2.

Experiment	**Run - time**	**Aim and characteristic**
E0	01.10.2001 - 30.09.2005	Reference run, complete forcing
E1	7 days	Test the spin-up of the upwelling process, regarding to the local alongshore wind with a homogeneous wind field
E2	01.04.2004 - 31.10.2004	Test the magnitude of the upwelling without the basin-wide forcing. The model is restarted every seven days, to inhibit a arise of basin-wide currents. Complete forcing, closed lateral boundaries.
E3	01.04.2004 - 31.10.2004	Test the magnitude of the upwelling without the Mekong river discharge. Complete forcing, but no river discharge.

Table 3.2: Model experiments in this work.

3.3 The Smagorinsky Scheme

In the HAMSOM-SCS model, horizontal sub-scale processes are parameterised by a variable horizontal turbulent exchange coefficient. For that, a Smagorinsky Scheme is used. The scheme is explained in more detail because it is newly implemented into the HAMSOM model. This allows for low values of the coefficient and vise versa which prevents instabilities in the SOR iteration. The framework established by Smagorinsky yields a non-constant viscosity coefficient in a physically consistent manner. The fundamental ideas and history behind the method are summarized in Smagorinsky (1993). The Smagorinsky scheme is based on some physical assumptions, mainly on the relevance of momentum dissipation as motivated by the elasticity theory. An introduction into the elasticity theory applied to dislocation is given by Hull and Bacon (1984) or by Landau and Lifshitz (1987). In the Smagorinsky parameterisations, the velocity shears are defined locally and are computed by finite differences between neighboring grid points.
The equation given by Smagorinsky is as follows:

$$A_h = c \cdot dx \cdot dy \cdot \sqrt{\left(\frac{\delta u}{\delta x}\right)^2 + \frac{1}{2} \cdot \left(\frac{\delta v}{\delta x} + \frac{\delta u}{\delta y}\right)^2 + \left(\frac{\delta v}{\delta y}\right)^2} \qquad (3.1)$$

The core of the equation inside the square root consist of two continuity terms (T_1, T_2)

$\left(\frac{\delta u}{\delta x}\right)^2$ and $\left(\frac{\delta v}{\delta y}\right)^2$ and a shear term (T_3) $\frac{1}{2} \cdot \left(\frac{\delta v}{\delta x} + \frac{\delta u}{\delta y}\right)^2$. c is defined as a dimensionless coefficient. In the SCS-Model it is set to 0.5, which results in most realistic preservation of frontal structures in combination with a stabilised SOR-scheme. The chosen value of *c* results in a horizontal turbulent exchange coefficient between 10 $m^2 s^{-1}$ up to 500 $m^2 s^{-1}$.
The discretisation took place on the zeta-nodes of the c-grid. Fig. 3.2 shows the geometric constellation of the distribution.
From fig. 3.2 one can deduce the implementation of equation (3.1).
In the model:

$$A_{h(i,j)} = c \cdot dx \cdot dy \cdot \sqrt{T_1^2 + T_2^2 + \frac{1}{2} T_3^2}$$

Here T_1, T_2 and T_3 are given by:

$$T_1 = \frac{(u_{i,j} - u_{i,j-1})}{dx_i}$$

$$T_2 = \frac{(v_{i,j} - v_{i-1,j})}{dy_i}$$

$$T_3 = \frac{1}{4} \cdot \left(\frac{|v_{i-1,j+1} - v_{i-1,j}|}{dx_i} + \frac{|v_{i-1,j} - v_{i-1,j}|}{dx_i} + \frac{|v_{i,j+1} - v_{i,j}|}{dx_i} + \frac{|v_{i,j} - v_{i,j-1}|}{dx_i} \right)$$
$$+ \frac{1}{4} \cdot \left(\frac{|u_{i+1,j-1} - u_{i,j-1}|}{dy_i} + \frac{|u_{i,j-1} - u_{i-1,j-1}|}{dy_i} + \frac{|u_{i+1,j} - u_{i,j}|}{dy_i} + \frac{|u_{i,j} - u_{i-1,j}|}{dy_i} \right)$$

In figure 3.2, T_1 is the blue rectangle, T_2 is the red rectangle and T_3 is the average of the green and the pink rectangle. With these equations, the horizontal turbulent exchange coefficient is calculated at every time step for every wet zeta-node at all depths. After the calculation the field of the coefficients is smoothed with an average of the surrounding dots.

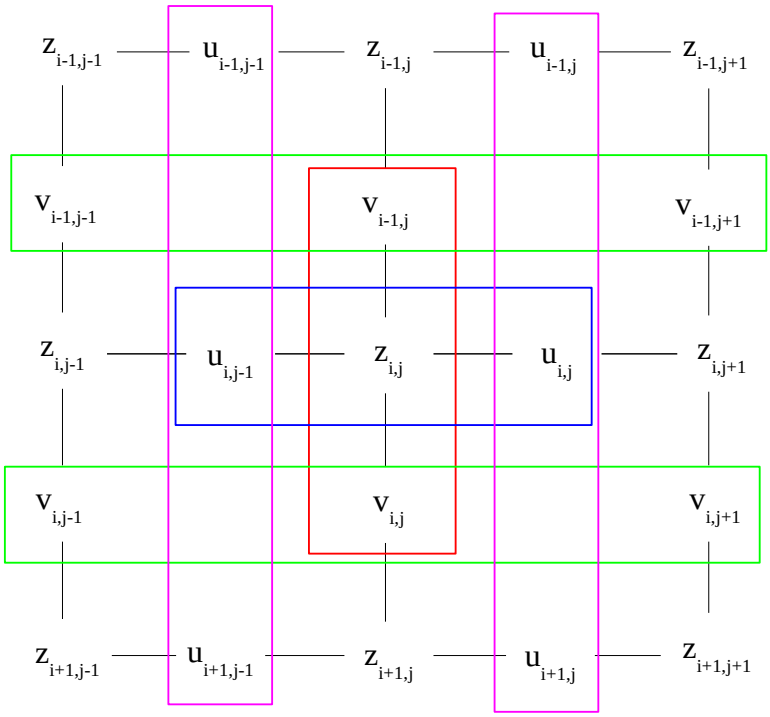

Fig. 3.2: Implementation scheme of the Smagorinsky equation on a c-grid. The blue rectangle represents the $\delta u / \delta x$, the red rectangle the $\delta v / \delta y$, the two pink rectangles the $\delta u / \delta y$ and the two green rectangles the $\delta v / \delta x$ term of the equation of the Smagorinsky Scheme (3.1)

Beyond the open boundaries, a horizontal turbulent exchange coefficient of 40 m^2 s^{-1} was implemented as a minimum value, which, combined with the Smagorinsky Scheme, form a stable calculation of the SOR-iteration in the main model area. However, near the Luzon Strait, a coefficient of 1000 m^2 s^{-1} was necessary to prevent instabilities, which is equivalent to a sponge layer in the most other model studies.

3.4 Assimilating Sea Surface Temperature into the Model

The idea of assimilating Sea Surface Temperatures (SST) into the model arose during the set-up of the model. Experiments with heat fluxes from the NCEP reanalysis were conducted, resulting in an inadequate distribution of the surface temperatures. Especially the bulk formulation used in the simulations reproduced an unrealistic cooling of the SCS. For longer timescales, the stability and variability of the SST is obviously better when using assimilations than those calculated with heat fluxes due to the atmospheric forcing. Kara et al. (2005) investigated in the relationship between heat fluxes and the SST. Their results show the general possibility of the substitution of heat fluxes with direct satellite-observed SST. However, an assimilation of temperatures may inhibit a complete prognostic physical calculation of the temperatures.

In the area between 40° North and 40° South, SST from satellite are available, measured by the Tropical Rainfall Measuring Mission Microwave Imager (TMI). This is a microwave radiometer and capable of measuring SST through clouds. Hence, the largest benefit of the TMI comes from the near all-weather sampling of SST. Other satellites, like Advanced Very High Resolution Radiometer (AVHRR), have the decisive disadvantage of data gaps resulting from clouds. The radiation wavelength at 10.7 GHz is O(3 cm) and at these long wavelengths the spatial resolution on the earth surface for a single TMI observation is about 50 km. This is a low resolution compared to the AVHRR but high compared to the NCEP reanalysis data. The forcing data from the NCEP provide only a spatial resolution of 2° 30' in latitude and longitude.

From the 5 channels of data provided by TMI, several parameters could be calculated over ocean surfaces: SST, 11 GHz 10m wind speed, 37 GHz 10m wind speed, columnar water vapor (atmospheric water vapor, integrated water vapor), columnar cloud water (cloud liquid water, liquid cloud water), 19-37 GHz rain rate (precipitation rate). In these studies, only the SST will be used. More technical details can be found in Kummerow et al. (1998).

Since the SST are a prognostic variable in HAMSOM, the general procedure of SST assimilation is to insert them into the model in an optimal way. The first simplification, therefore, is to assume that the horizontal correlations are small enough to be ignored. This

means that within the assimilation routine, the model can be treated as an array of one-dimensional vertical mixing models, and any relationship between horizontal temperature gradients and density-driven flows can be ignored. Moreover, it is assumed that the standard deviation of the model temperatures are more than twice as high as those obtained from the observations. This is supported by Gentemann et al. (2004). These assumptions reduce the problem to one of assimilating SST information in a vertical water column with a simple fixed structure.
In this work, first, the differences between the satellite observations and values reproduced by the model are calculated:

$$t_{diff} = t_{TMI} - t_m$$

with:

- t_m the temperature of the model
- t_{TMI} the temperature from satellite observations

The temperature of the new time-step, then, is the sum of the old temperature and the factorized difference t_{diff}:

$$t_m = t_m + \alpha \cdot t_{diff}$$

The assimilation factor is the length of one time step of the model divided by the factorised length of a day:

$$\alpha = \frac{(Model\,Time\,Step)}{k \cdot (Day\,Length)}$$

k is a coefficient, which is adjusted empirically to a value that yields a complete surface temperature field after two to three days, similar to the one obtained from satellite observations, under the condition, that no strong hydrodynamic processes took place.
Hence, k is set to 0.4.
Work on assimilating conventional temperature measurements into deep ocean models has been performed by Derber and Rosati (1989). Annan and Hargreaves (1999) used a Kalman filter to assimilate data from satellite temperature observations into their model. Data assimilation normally requires knowledge of the error statistics of both the model and observations (Kalman, 1960). The accuracy of the surface temperatures from HAMSOM are not well known, hence the use of a Kalman filter is not practicable. Assimilation may lead to imbalances between the thermal fields and the dynamical fields during the assimilation process (e.g. Syu and Neelin 2000; Tang and Heish 2003). In HAMSOM, an unstable stratification due to the assimilation or convectional overturning is turned rapidly into a neutral state by a strong enlargement of the vertical eddy viscosity coefficient.

3.4 Ship experiments

As said in the introduction, data sets acquired in the past have not been sufficient to address the questions about the governing process and the variability of the upwelling in the VUA. Hence, five extensive oceanographic field cruises were conducted. Two cruises took place during the boreal summer and southwest monsoon, two during the inter-monsoon in April and one towards the end of the northeast-monsoon in March. The hydrographic surveys extended alongshore from the Mekong river mouth up to Cap Varela at 13° North. This region spans the widely recognised location of the upwelling.

On the combined biological and hydrographic cruises, conductivity and temperature of the seawater were measured on a grid of stations. The first cruise even included measurements of horizontal currents. For conductivity and temperature measurements, a Seabird CTD (SBE19+) was used. The CTD was also endowed with an optical fluorescence sensor and an optical turbidity sensor.

On the first cruise, velocity profiles have been measured at all stations down to a water depth of 130 m using a current meter (NOBSKA, MAVS-2) with a sampling frequency of 1.42 Hz. The MAVS-2 Current Meter is an acoustic current meter which employs a differential travel time measurement technique across 4 acoustic axes. While the range of measurement is 300 cm s^{-1}, low speed measurement accuracy in the 0.03 cm s^{-1} to 10 cm s^{-1} range is preserved. However, this accuracy has to be seen as a theoretical (internal) accuracy. On each station only short-time observations (< 300 s) were possible, hence short-time variations of the currents strongly influence the measurements. During the latter cruises the instrument did not work satisfactorily. Moreover, meteorological observations were collected at each grid station. Interpretation of the meteorological data is difficult, because they vary in time and space, and no reference stations were available. Hence, analyses of the wind field took place from remote forced data, e.g. Quickscat wind.

Outside the scope of this study a biological study took place, which is illustrated by Dippner (2007). At oceanographic standard depths, water samples were taken which have been analysed on board for nutrients (nitrate, nitrite, phosphate and silicate), oxygen, pH, alkalinity, and dissolved inorganic carbon (DIC) and chlorophyll *a*. At selected stations, water samples were taken for incubation experiments with respect to primary production, nitrogen fixation and new production. Vertical hauls of phytoplankton, zooplankton and ichtyoplankton were taken with different mesh sizes. During daylight, Secchi depths were observed.

A complete description of the station grid and an interpretation of the hydrographic data as well as the fluorescence data is presented in chapter 6.

3.5 Remote sensing

The NASA publishes chlorophyll *a* concentrations, observed by the Sea-viewing Wide Field-of-view Sensor (SeaWiFS) (http://reason.gsfc.nasa.gov/OPS/Giovanni/ocean.seawifs.2.shtml). Due to the longer wavelength of the backscattering signal, the observed chlorophyll concentration is not only limited to the skin of the sea surface, as SST are.

Although the observations were often disturbed by cloud cover, the concentrations can provide information about the magnitude of the upwelling on monthly scales. They may not give information about the magnitude of the physical process, but they do give good information on its effectiveness on the primary production. The SeaWiFS chlorophyll *a* values are used for the estimation of the inter-annul variability. Therefore, the relationship between the ENSO and the magnitude of chlorophyll *a* is calculated.

4
Validation of the model

4.1 General circulation of the South China Sea

Though the goal of this thesis is to analyze the Vietnam upwelling process, the circulation of the SCS has also been proven to be correct. To get a realistic distribution of the currents in the region of upwelling, the main circulation of the SCS has to be reproduced well by the model. While basin wide observations of currents are not available, Sea Surface Heights (SSH) observed with satellites are a possible means to validating the model. The sources of the satellite data are the same as for the open boundaries. During the adjustment process, the satellite data was used to optimize the circulation of the SCS. One of the most important circulation feature is the northern cyclonic eddy which is present the whole year. The eddy is noticeable in the simulation in most cases. Especially in summer, the strength of this eddy is of importance to the current distribution in the VUA. In experiments it was noticeable, that this eddy is sensitive to the Luzon Strait transport and can be calibrated with small manipulations of the boundary conditions in the northern Luzon Strait. In this region, the lack of satellite data due to the small distance to the Taiwan Island is problematic. Hence, the SSH in the northern Luzon Strait are determined by an extrapolation process. Several experiments with differently extrapolated SSH for the northern Luzon Strait were conducted. The results were compared to the satellite data, for a runtime of up to about 12 months. The best representation of the SSH, especially in the western SCS, was used in the final experiment of the simulation (E0).
An example for the distribution of the SSH during summer and winter of E0 and the satellite data is given in fig. 4.1a-d. Figure 4.1a illustrates the distribution of the SSH form the model, averaged for the period from December, 13th 2003 to December, 17th 2003, fig. 4.1b the SSH observed by satellite for the same period. According to fig. 4.1a, b, the

simulation is able to reproduce the SSH reasonably well. The main features can be found in both figures, the cyclonic eddy northwest of Luzon is also present, as is the raised sea level at the mouth of the Gulf of Thailand. Moreover, the raise of the sea level at the coast of Borneo appears in the model, as well as the small cyclonic band at the western shelf. However, some of the observed eddies on the mesoscale are absent from the model. Considering the resolution and the diffusivity and with respect to the stability of the model, this has to be accepted as a trade-off.

The SSHs during summer are illustrated in fig. 4.1c and fig. 4.1d, from simulation and observation, respectively. A four day average from the first week of August is illustrated, representative of the complex circulation in late summer. In both figures, the northern basin is dominated by cyclonic eddies, the strongest is found south-east of Luzon Island. In the southern basin an anticyclonic eddy is present, which can be seen as well in the simulation. This eddy forms the southern part of the Vietnam dipole, with a cyclonic eddy at about 12° 30' N, near the coast of Vietnam. The dipole structure is the most obvious phenomenon in the VUA during late summer. However, in the data from observations, this structure is much stronger and the cyclonic eddy is orientated in a further offshore direction. The simulated horizontal mixing of the light water in the south, influenced by the Mekong, with the dense water in the north may be too strong reducing the strength of the barocline flow. The SSHs on the Sunda Shelf are reproduced also acceptably well. However, in the central SCS, the model simulates a relatively strong anticyclonic eddy, which is to be found further to the west in the satellite data. The simulated sea level on the northern shelf and the Gulf of Tonkin is definitely too high. The sea level built-up due to the monsoon seems to be too high during most of the simulation. This may be due to a to homogeneous wind field.

Appart from these last two features, the distribution of the SCS fits quite well, even in summer, when the situation is more complex.

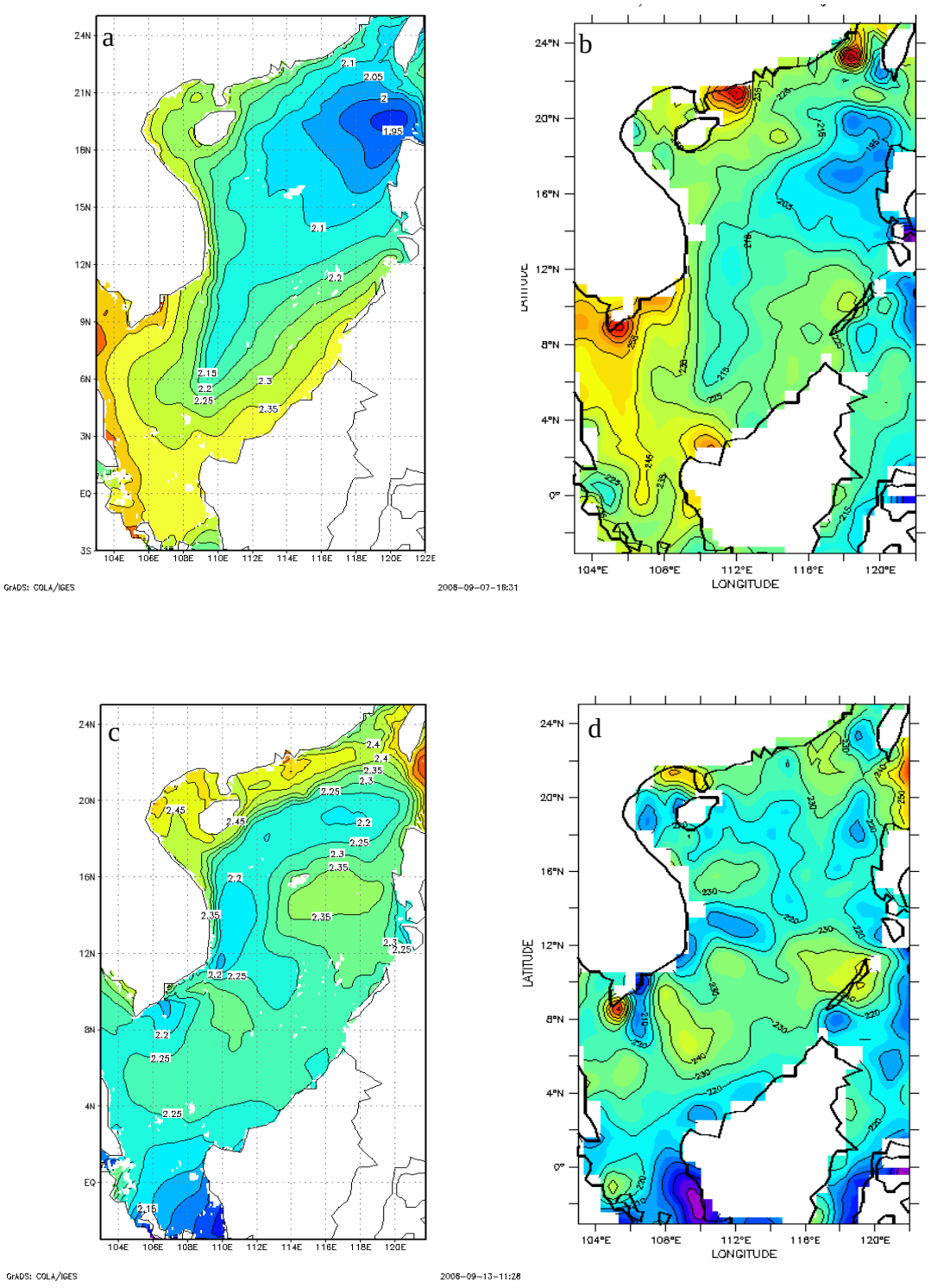

Fig. 4.1: Sea surface heights measured by satellite (b, d) and reproduced by HAMSOM (a, c), during winter (a, b) and summer (c, d)

Fig. 4.2 shows a time series of the reproduced SSH and the satellite SSH in the center of the upwelling, at 11° N, 109° E. Both time series are averaged over a period of 15 days to prevent interferences from mesoscale circulations. Both curves match reasonably well. The correlation is significant, at a value of 0.75. However, in summer of 2002, the simulated sea level is too low, resulting from a slightly too strong cyclonic circulation in the northern basin. In winter of 2004, the sea level is about 10 cm higher than in the satellite data. As mentioned before, the sea level built-up due to the northeast monsoon seems to be overestimated in the simulation.

Metzger and Hurlburt (2001) separated the effect of direct atmospheric forcing and the effect of non-deterministic flow instabilities on the mesoscale in the SCS. In the VUA the fraction of non-deterministic circulation is about 45 %. According to Metzger and Hurlburt, who compare the SCS with the western Pacific, this ratio is relatively high and thus difficult to reproduce. Pohlmann (2006) analysed the impact of the model resolution on the mean energy and the eddy kinetic energy. He used a large scale model with a resolution of 20 km and a mesoscale model with a resolution of 3 km. His conclusion is, that the mean kinetic energy in the mesoscale model is about 100% - 200% higher than in the large scale model. If the circulation is strongly non-deterministic, as in the VUA, this may cause problems: if the mean kinetic energy is not high enough, the model may not solve all mesoscale current interactions sufficiently well.

Considering these difficulties posed by the complex circulations in the SCS, the result of the SCS simulation are acceptable.

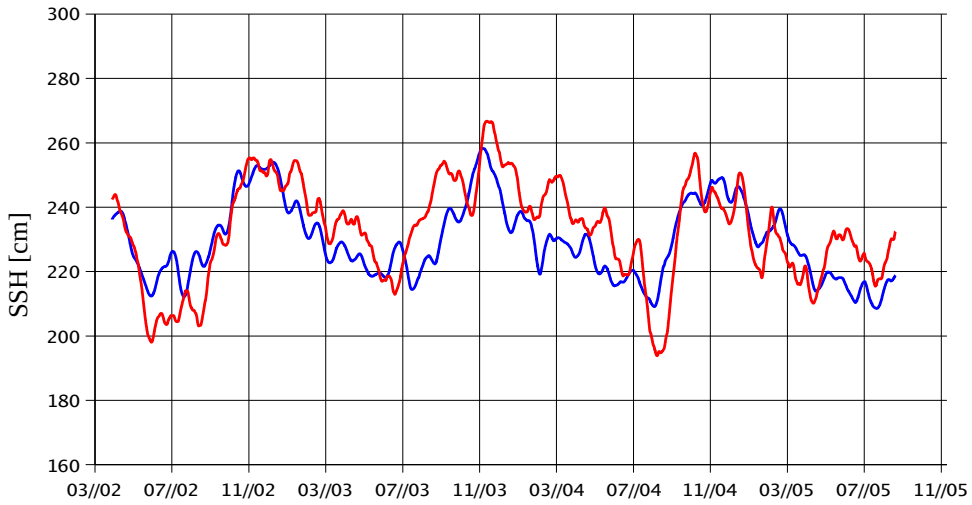

Fig. 4.2: Time series of the satellite measured (blue line) and reproduced (red line) SSH at 11° N, 109° E.

4.2 Validation by the means of the cruise data

To validate the model circulation with the focus on the VUA, the model results will be compared with the in situ measurements from the cruises of this project.

Fig. 4.3a and fig. 4.3b show the distribution of the simulated and the measured surface currents during the cruise VG03 (Juli, 2003). The currents are depth-averaged from the surface down to 40 m.

First, it should be mentioned that the magnitudes of the observed currents is O(40 %) higher than those of the simulated ones. However, the direction of the currents are congruent. On the outer shelf, a boundary current is present. Inshore the boundary current north of 12° N, a recirculation forms a cyclonic eddy. This can be found in the observations as well as in the simulated currents. Although it is not as clearly visible, the offshore rotation of the boundary current at 12° N is reproduced reasonably well. Moreover, the divergence of the currents at 11° 30' N can be seen in fig. 4.3a and fig. 4.3b.

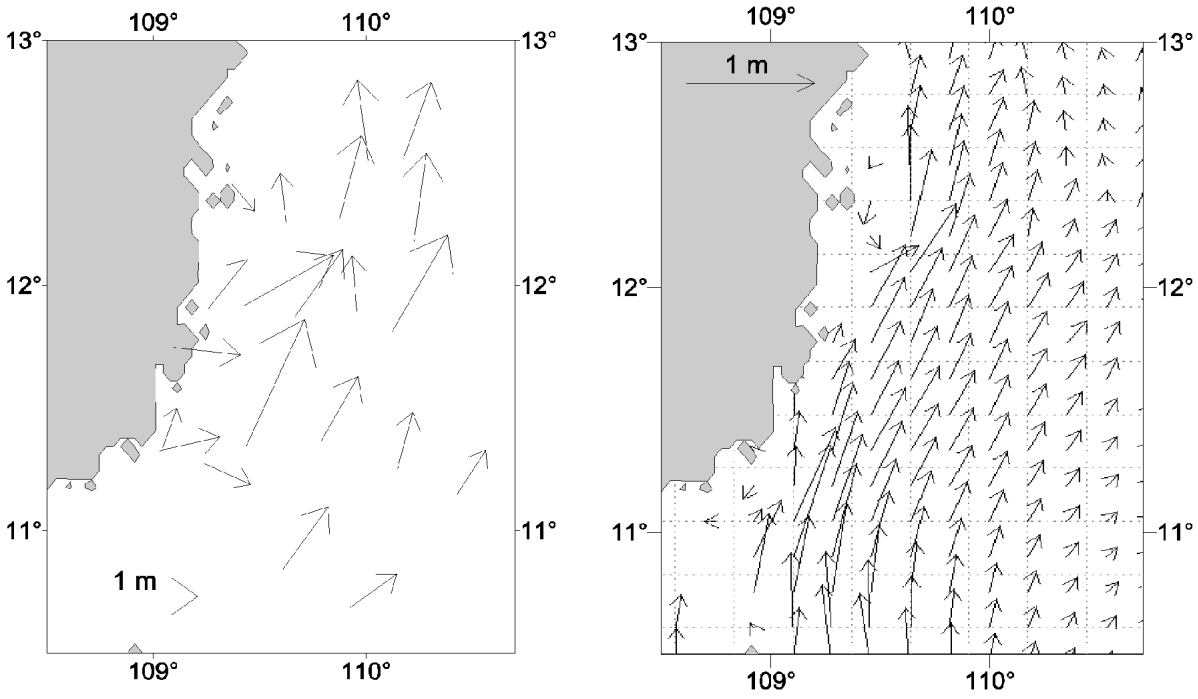

Fig. 4.3: Distribution of currents in the simulation (a) and in the observations (b)

In the summer 2003 a well-defined plume of low salinity water influenced by the Mekong spread through the VUA. Fig. 4.4a, b illustrate the observed distribution of salinity and also

the one reproduced by the model. In both illustrations the plume is discernible, as well as the offshore displacement of the water masses at about 12° N. The frontal zone between the plume and the surrounding water is less well-defined in the simulation. Considering also the distribution of the SSH, numeral diffusion may be responsible for this fact.

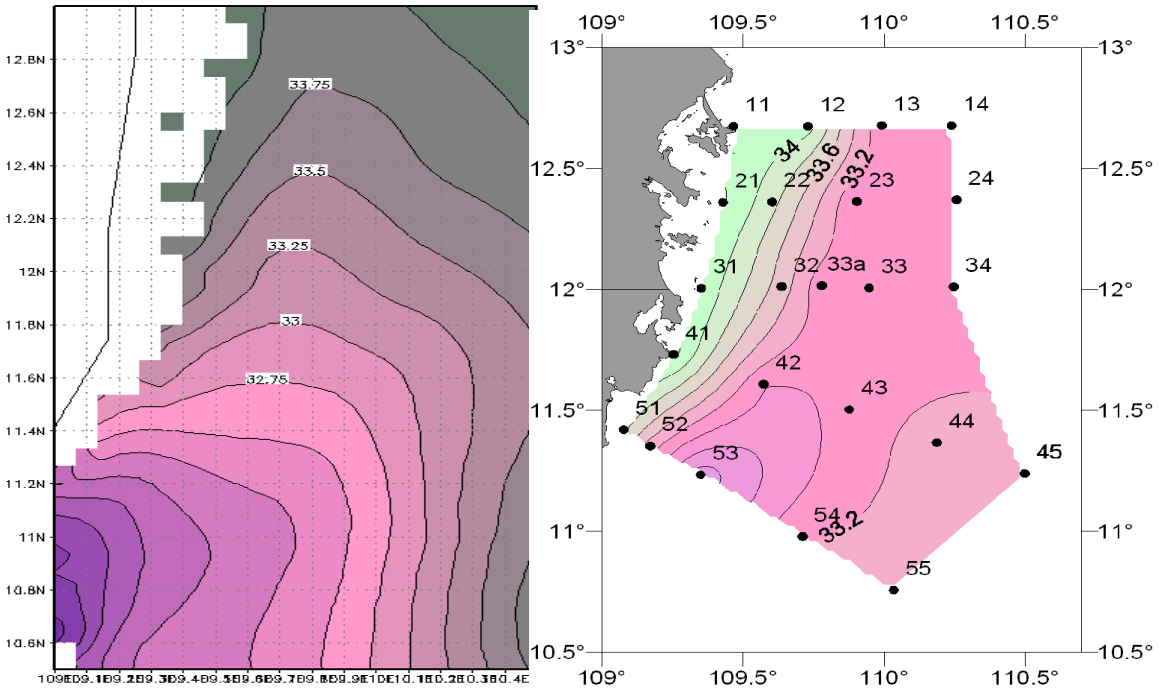

Fig. 4.4: Distribution of salinity [PSU] of the simulation (a) and the CTD measurements (b)

The temperature field from the CTD measurements in a section perpendicular to the coast in April 2004 (VG04) and Juli 2004 (VG07) illustrate upward tilting of the isotherms (fig. 4.5b, d). Fig. 4.5a, c illustrate the reproduction of the temperature fields for the same times by the model. The upward tilting of the isotherms can also be seen, but the thermocline is less distinctive than in the observations. Moreover, the reproduced uplift of the temperature layers and the salinity layers near the coast is always smaller than in the measurements.
Overall, the validation illustrates that the circulation of the SCS and in the VUA are simulated acceptably well. The horizontal circulation during VG03 can reproduce the main features of the mesoscale currents.

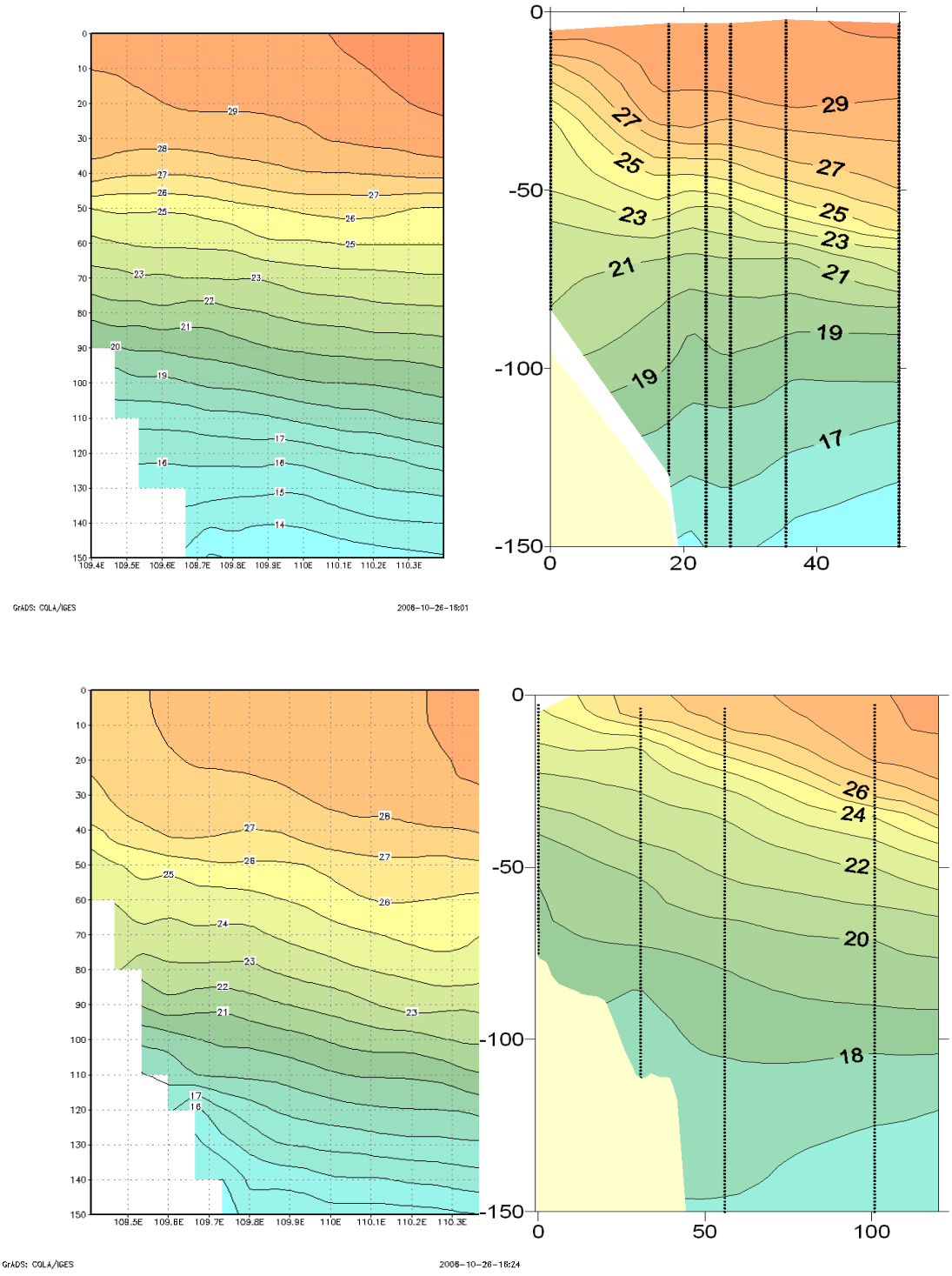

Fig. 4.5: Distribution of temperature [°C] of the simulation (a, c) and the CTD measurements (b, d) perpendicular to the coast at 12° N in April 2004 (a, b) and at 11° 45' N Juli 2004 (c, d)

5

The three dimensional circulation in the Vietnam Upwelling Area

Due to the changing wind forcing, the bathymetry and the southward and northward boundary currents, a complex current system is present throughout the year. This section tries to give an overview of this three dimensional system. The horizontal circulation down to 130 m in the VUA is illustrated, and classified into six states. The pattern of the depth-averaged vertical velocities for each of these states is given and the coherence between horizontal and vertical velocities is explained.

5.1 States of the horizontal circulation in the VUA

The horizontal circulation of the VUA can be classified by six different states. Apart from the direction of the local wind stress, these states depend mainly on the direction of the boundary currents of the basin-wide circulation. In winter three consecutive states can be found, according to a cold surge, a weak north east monsoon and a total monsoon break, respectively. During the winter-to-summer transition, for about one or two weeks, a separate state appears, representing the transition from a cyclonic to an anticyclonic circulation. The fifth state, caused by the anticyclonic circulation of the south and central SCS, usually can be found from late April to June or July. At that time of the year, only in the northern part of the SCS the circulation is still cyclonic, but this is irrelevant to the VUA. With the magnification of the cyclonic circulation in the north and the amplification of its southward boundary current, a sixth state is established. The appearance of either of the summer states depends on the existence of the southward boundary current, which may be present in late summer, as it was in the years 2003 and 2005. However, in the years 2002 and 2004 it appeared earlier, in June. In these years a switch back to state 4 sometimes occurred, which

means that the southward boundary current disappeared south of 13° N, but was still present in the northern part of the SCS. State 6 has a strong variability, depending on the strength of both boundary currents. In the inter-monsoon between summer and winter a fast switch between state 6 and state 2 occurs. For a few days, again, a separate state may be present. However, this will be neglected here, because no significant vertical circulation is present during that time. All the results shown here present situations, which are, depending on the state, averaged over 10 to 30 days.

For each state the surface circulation (0 m – 20 m, L1), the circulation from 40 m to 60 m (L2), from 70 m to 80 m (L3) and from 110 m to 130 m (L4) are shown. To relate the text with the figures, the described features are numbered with F1, F2, F3, etcetera. Significant main currents are highlighted with arrows.

Figure 5.1a shows the distribution of the horizontal currents at the surface of state 1. The convergence of the currents near the shelf edge (F1) is the most striking property of this state. Due to the strong northeast monsoon, which forces an Ekman drift current in the open sea, the surface water is driven towards the shelf. On the shelf, a southward boundary current is present with a high-velocity core on the mid-shelf of more than O(120 cm s^{-1}). The boundary current and the off-shelf drift current converge north of 12° N. The strongest velocities can be found here (F2). South of this position, the boundary current disperses (F3) and further to the south, the core follows the shelf edge (F4). On the shelf itself the velocities are decreased to O(80 cm s^{-1}). In L2 (fig. 5.1b) the direction of all the velocities is southward; north of 11° 10' N (F5), no convergence is present anymore. The velocity of the current is O(70 cm s^{-1}) across the whole area. At F6 the current follows the curvature of the shelf edge, as in L1 the velocities on the shelf (F7) are lower than those off the shelf, where a weak cyclonic circulation is visible (F8).

The circulations of L3 (fig. 5.1c) and L4 (fig. 5.1d) show the boundary current flowing along the bathymetry with velocities of O(50 cm s^{-1}). At certain positions (F9) the homogeneity is disturbed due to interference of sea mountains. A significant inshore deceleration can not be found anymore. The cyclonic circulation (F8) off the shelf is slightly stronger in L3 and L4.

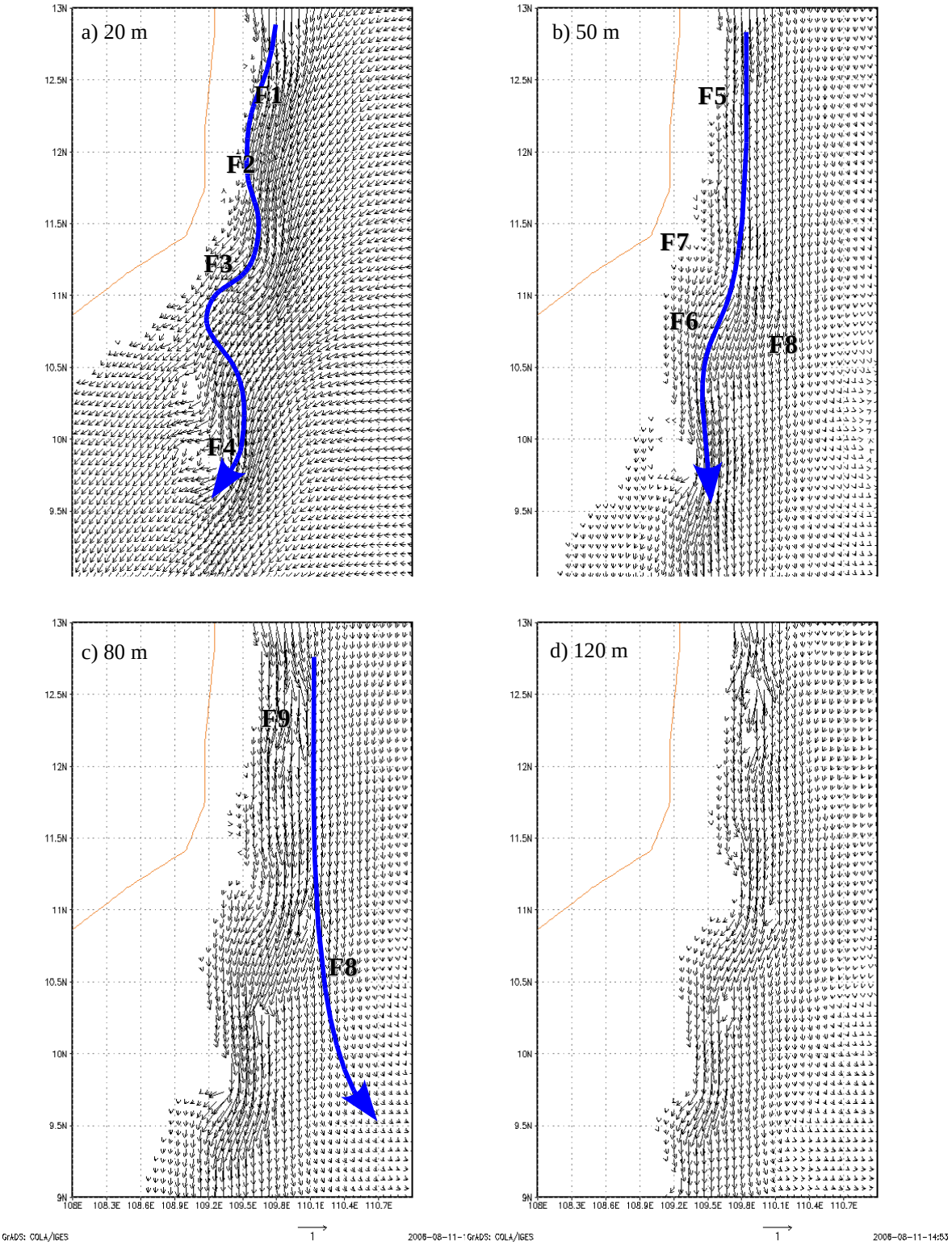

Fig. 5.1: The horizontal circulation reproduced by the model during state 1, the main currents are highlighted with arrows, units: m s^{-1}

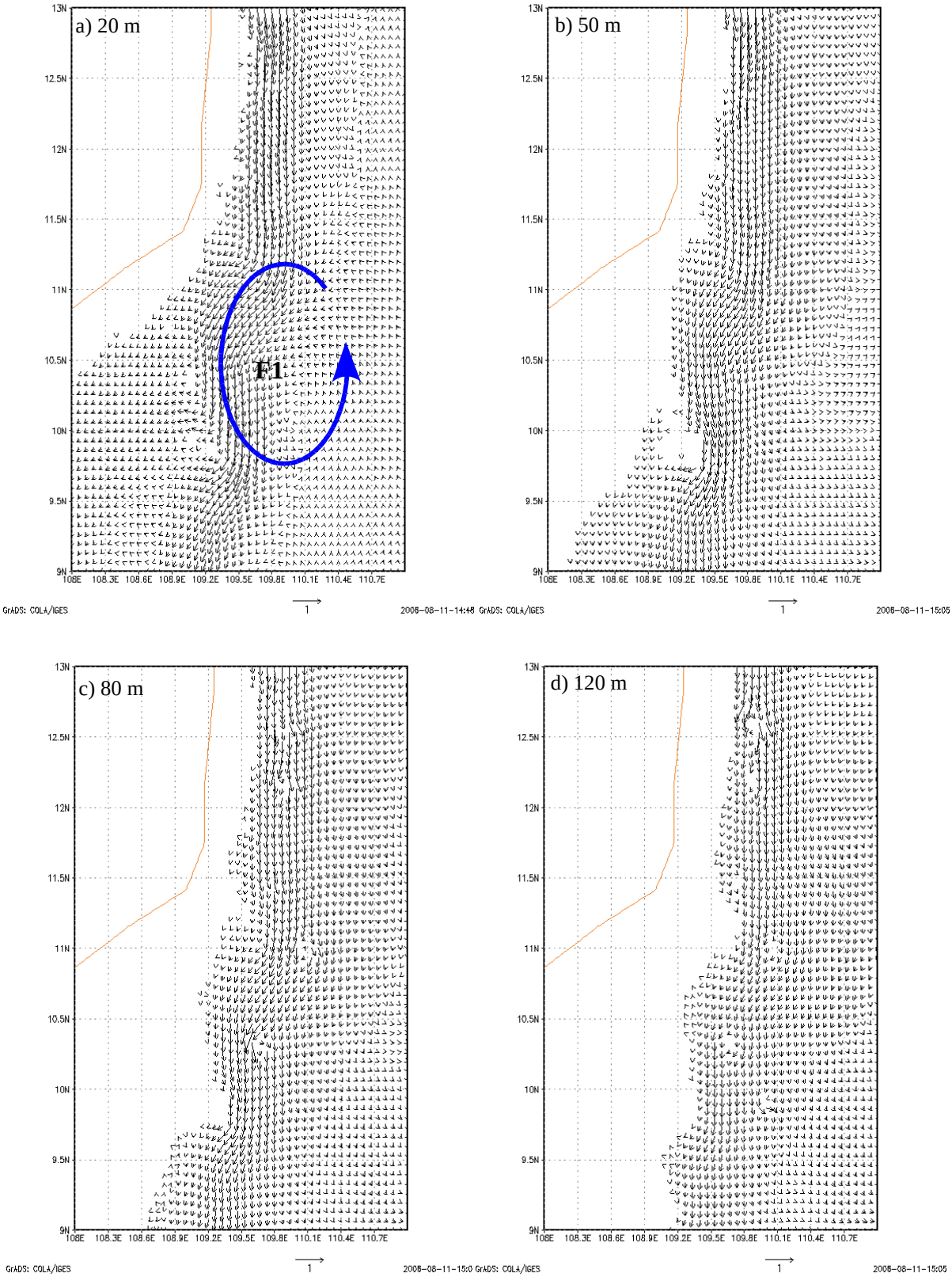

Fig. 5.2: The horizontal circulation reproduced by the model during state 2, the main currents are highlighted with arrows, units: m s^{-1}

State 2 appears when the northeast monsoon is weak, as well at the beginning or the end of the winter monsoon, as during periods in which the monsoon is not influenced by a cold surge. The distribution of horizontal velocities at the surface (L1) during state 2 is illustrated in Figure 5.2a. The boundary current is present, as in state 1, but the convergence due to Ekman drift currents can not be found. The velocities of the main current are O(60 cm s^{-1}). Off the shelf only a low onshore drift current is indicated. Moreover a significant acceleration caused by the converging currents is absent. The core of the boundary current follows the shelf edge with a homogeneous velocity. At O(10° 20' N / 110° E) a cyclonic recirculation of the southward boundary current is indicated (F1).
The distribution of the currents in L2 (fig. 5.2b) is, roughly speaking, the same as that in L1. The core of the boundary current flows along the shelf edge with an average speed of O(30 cm s^{-1}). Off the shelf, there is no significant cyclonic recirculation and the currents are directed offshore. At the deeper levels (fig. 5.2c, fig. 5.2d) the structure of the currents is similar to that in L2. The current speed of the core of the boundary current in L2 and L3 is O(30 cm s^{-1}) and O(25 cm s^{-1}), respectively. Throughout the water column, the velocities of the currents of state 5 are only O(60 %) of those of state 1.
During a complete break of the northeast monsoon, after a cold surge, state 3 is present for approximately one week. Fig. 5.3a shows the complex surface circulation (L1) of this state. On the outer shelf the southward boundary current (F1) is present, with a magnitude of O(50 cm s^{-1}). On the inner shelf a weak counter current (F2), with a strength of O(10 cm s^{-1}), appears. At 11° 30' a stronger (O(30 cm s^{-1})) northward current can be found as a part of an anticyclonic recirculation, which rotates offshore and joins the southward boundary current. Both build a meandering current along the shelf edge (F4). In L2 (fig. 5.3b), off the shelf, an anticyclonic eddy builds a closed circulation (F5). The distribution of the currents in L2 (fig. 5.3b) is very similar to that at the surface. The southward boundary current can be found (F5, F6). No counter current is present on the inner shelf in the north, but the anticyclonic eddy (F7) appears more clearly than at the surface. At 80m (L3, fig. 5.3c) the southward boundary current can be found on the shelf through the whole area (F8, F9). In the central part (F10) the boundary current widens and the strong sheer on the offshore side disappears almost completely. In the north, at about 12° N, a small part of the boundary current turns anticyclonicly in the direction of the coast (F11). In the canyon-like structure a counter current is present (F12), with a slightly onshore component as well. In L4 (fig. 5.3d), the boundary current is present as in the water column above. No clear meandering of the current occurs, even at a changing alongshore bathymetry, it flows without significant rotation. Off the shelf, two weak cyclonic recirculations (F15, F16) are built.

The fourth state appears during inter monsoon, it is only present for about ten days. The southward boundary current is still active, but at the beginning of April an anticyclonic eddy

moves westward towards the shelf, and interacts with the boundary current. In L1 (fig. 5.4a), the southward boundary current (F1) is present up to 11° 30' N with values of O(30 cm s^{-1}). At this position it rotates cyclonicly and builds a northward recirculation. In the canyon-like structure a strong (O(30 cm s^{-1})) mesoscalic eddy (F3) is obvious, disturbing the current from the north. In the southern region, a cyclonic circulation (F4) is established, resulting in a southward boundary current south of 10 ° N.

In L2 (fig. 5.4b) the southward boundary current (F5) is also present up to 11° 30' N. South of 11° N (F6) the entire currents flow westward, rotating southward on the shelf. One might conclude, that the southward boundary current (F7) forces the flow in an onshore direction. In between, a mesoscalic anticyclonic eddy (F8), emerged from the interaction of the westward current and the southward current, is present.

At a depth of 80 m (L3, fig. 5.4c) the southward boundary current (F9) can be found across the whole area. A part is moving onshore, near 11° N, where it merges with the current resulting from the anticyclonic eddy (F10). South of 11° N the currents from the offshore anticyclonic eddy rotate cyclonicly (F11) and coalesce with the boundary current (F12). The mesoscalic anticyclonic eddy on the shelf can not be found at this depth. The circulation in L4 is comparable with that of L3, so it is not shown here. Instead, fig. 5.4d shows the anticyclonic eddy at L3, before it reaches the shelf. Due to the larger spatial extent in this figure, only every second grid point is shown. The eddy in the deep central area of the SCS is well recognizable (F13). From this figure to the confluence situation it takes one weak. The circulation is comparable with that of state 3, with an additional component, the offshore anticyclonic eddy.

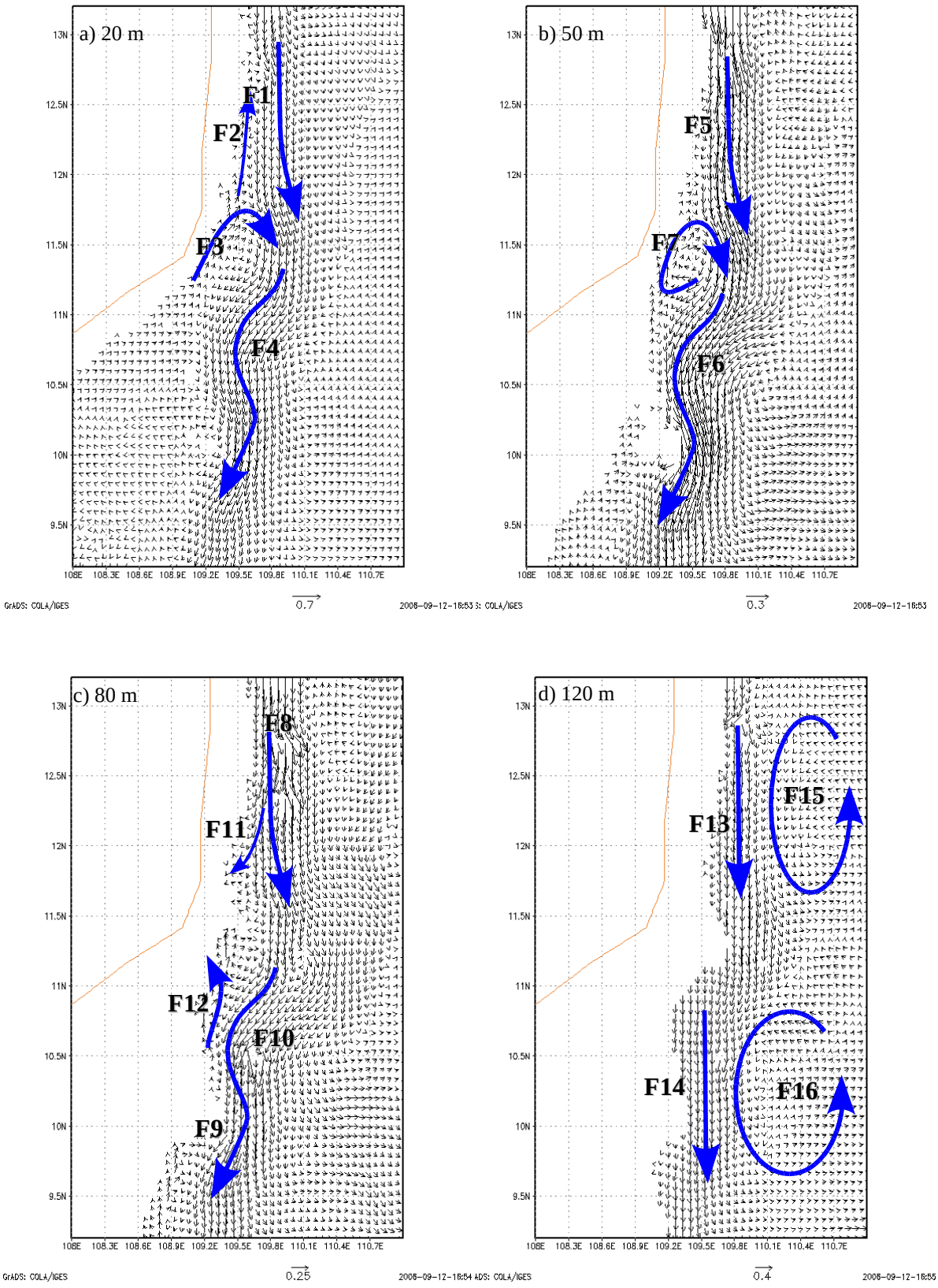

Fig. 5.3: The horizontal circulation reproduced by the model during state 3, the main currents are highlighted with arrows, units: m s^{-1}

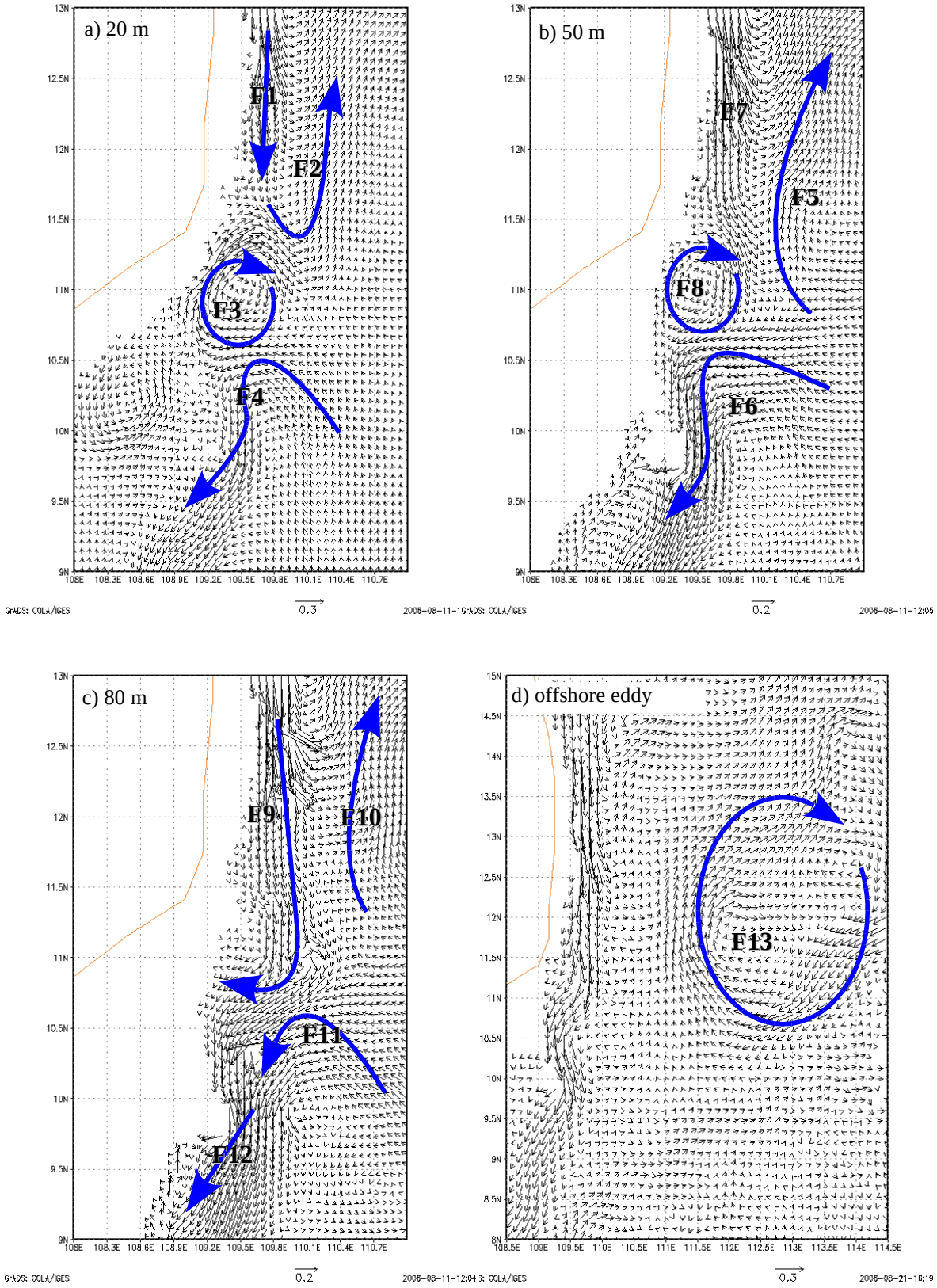

Fig. 5.4: The horizontal circulation reproduced by the model during state 4, the main currents are highlighted with arrows, d) shows an anticyclonic eddy two weeks before state 4, units: m s^{-1}

At the end of the inter-monsoon, in May, the southward boundary current is replaced entirely by the anticyclonic eddy, and thus a new boundary current to the north is built.

This distribution of currents in the fifth state can appear from May to July. This state is dominated by a strong northward boundary current which can be found through the whole water column on the shelf. The velocities of the core are typically O(70 cm s^{-1}), but they can reach values of more that O(100 cm s^{-1}). Fig. 5.5a covers the boundary current at the surface (L1). It can be found on the shelf, north of 9° 30' N, meandering along the bathymetry. Off the shelf, two weak mesoscalic recirculations (F1, F2) appear. North of 12° N all the currents are in an offshore direction (F3). At a depths of 50 m (L2) and 80 m (L3) (fig. 5.5b, fig. 5.5c), one might say, that the boundary current is the western part of an anticyclonic eddy (F4, F5), covering the whole western deep basin of the SCS. The recirculation eddies, which can be found at the surface, vanish from the figure. More interesting is the circulation at 120 m (L4), shown in fig. 5.5d. At this depth, the boundary current is significantly weaker than in the layers above. On the other hand, an offshore anticyclonic eddy (F6) joins the boundary current north of 12° N. In the canyon-like structure at 10° 20' N the currents are mainly directed onshore (F7).

With the continuing southwest monsoon, a southward boundary current develops. This causes the sixth state. Figure 5.6a shows the distribution of the horizontal currents for this state at the surface (L1). It is dominated by the confluence of the two boundary currents (F1, F2). They meet at 11° 30' N and build an offshore current (F3). The velocities of both currents are approximately O(50 cm s^{-1}), that of the offshore flow is slightly higher with O(60 cm s^{-1}). In the center of the confluence zone the currents are weak (F4). Below the surface at a depth of 50 m (L2, fig. 5.6b) the most obvious current is the southward boundary current (F5), with a velocity of O(60 cm s^{-1}). Between 11° N and 11° 30' N it turns anticyclonicly and flows in an onshore direction. The northward current from L1 can only be found in the southernmost part (F6), the flow being slightly directed onshore. In the whole offshore area, an anticyclonic eddy (F7) is present. A specific property of this state is a mesoscalic anticyclonic eddy (F8) in the canyon-like structure at 10° 30' N and 109° 30' E. It is strong O(40 cm s^{-1}) near the bathymetric boundary to the southwest and barely noticeable on its southeastern border. This eddy (F9) remains at a depth of 80 m (fig. 5.6c), however with a noticeable change of its structure. Compared to L2, the region with the strongest currents in this layer is further upstream. At this depth, the southward boundary current (F10) and the anticyclonic eddy (F11) are present, as they are in L2.

At 120 m, the offshore anticyclonic eddy still remains. Now, the southward boundary current (F12) covers the whole distance up to 10° 10' N, where it turns anticyclonicly towards the coast. Between these two main currents, near the shelf edge, the velocities are negligibly low.

Interestingly, in this state, again, a mesoscalic anticyclonic eddy appears in the canyon-like

structure. It seems to be comparable to the mesoscalic anticyclonic eddy of state 2 and state 3. However, during inter monsoon the eddy is to be found at smaller depth. The description of the mesoscale eddy is difficult, but one could describe it as a three-dimensional spiral in the canyon-like structure, mainly forced by the southward boundary current and totally steered by the bathymetry. Incontrovertibly, it is the main feature of the local circulation and is independent of the season.

Due to the decreasing southwest monsoon during September or October, the southward boundary current gains rapidly in strength, and with it, the northward boundary current is weakened, until only the southward current remains. This circulation structure is again that of state 2, thereby ending the seasonal cycle.

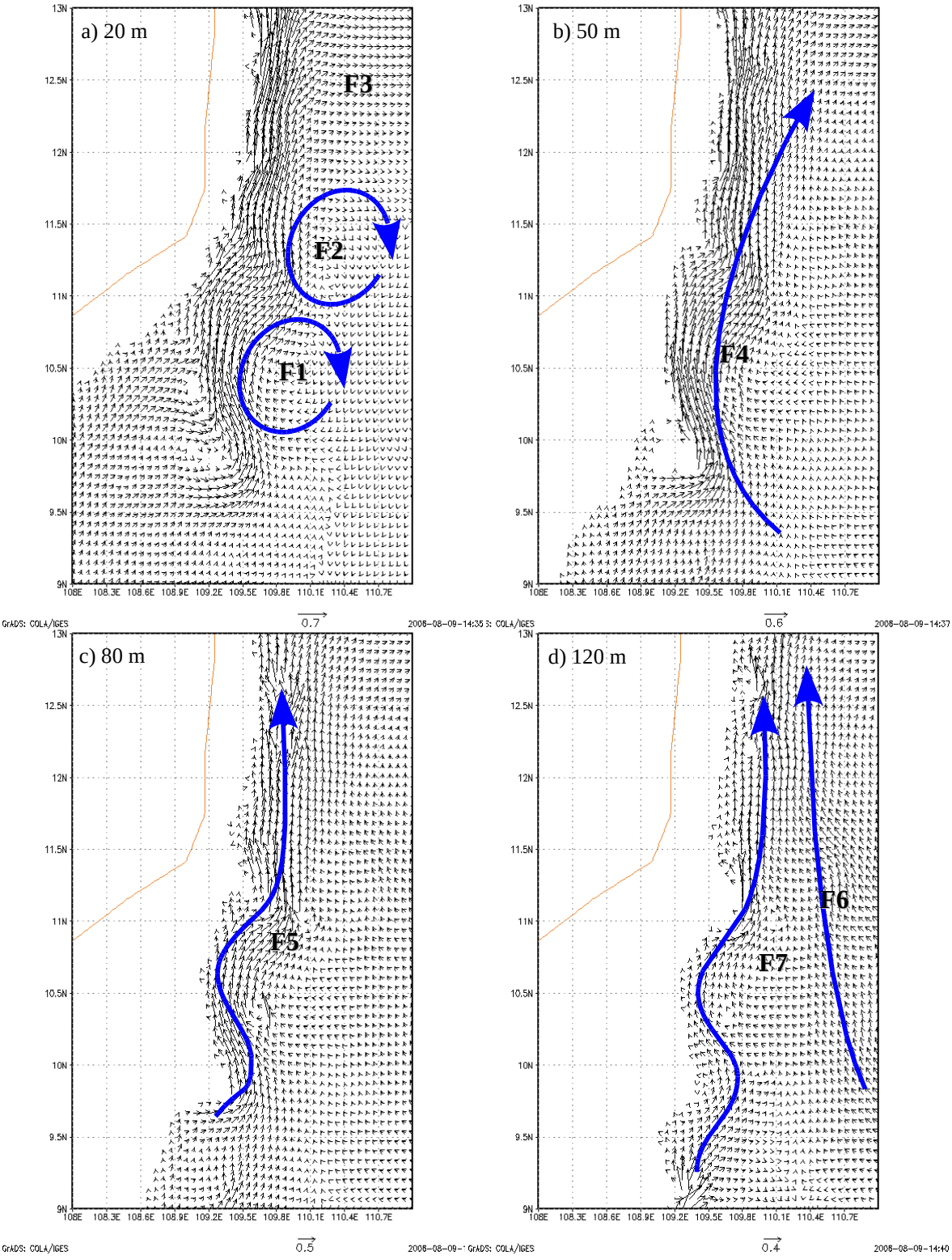

Fig. 5.5: The horizontal circulation reproduced by the model during state 5, the main currents are highlighted with arrows, units: m s^{-1}

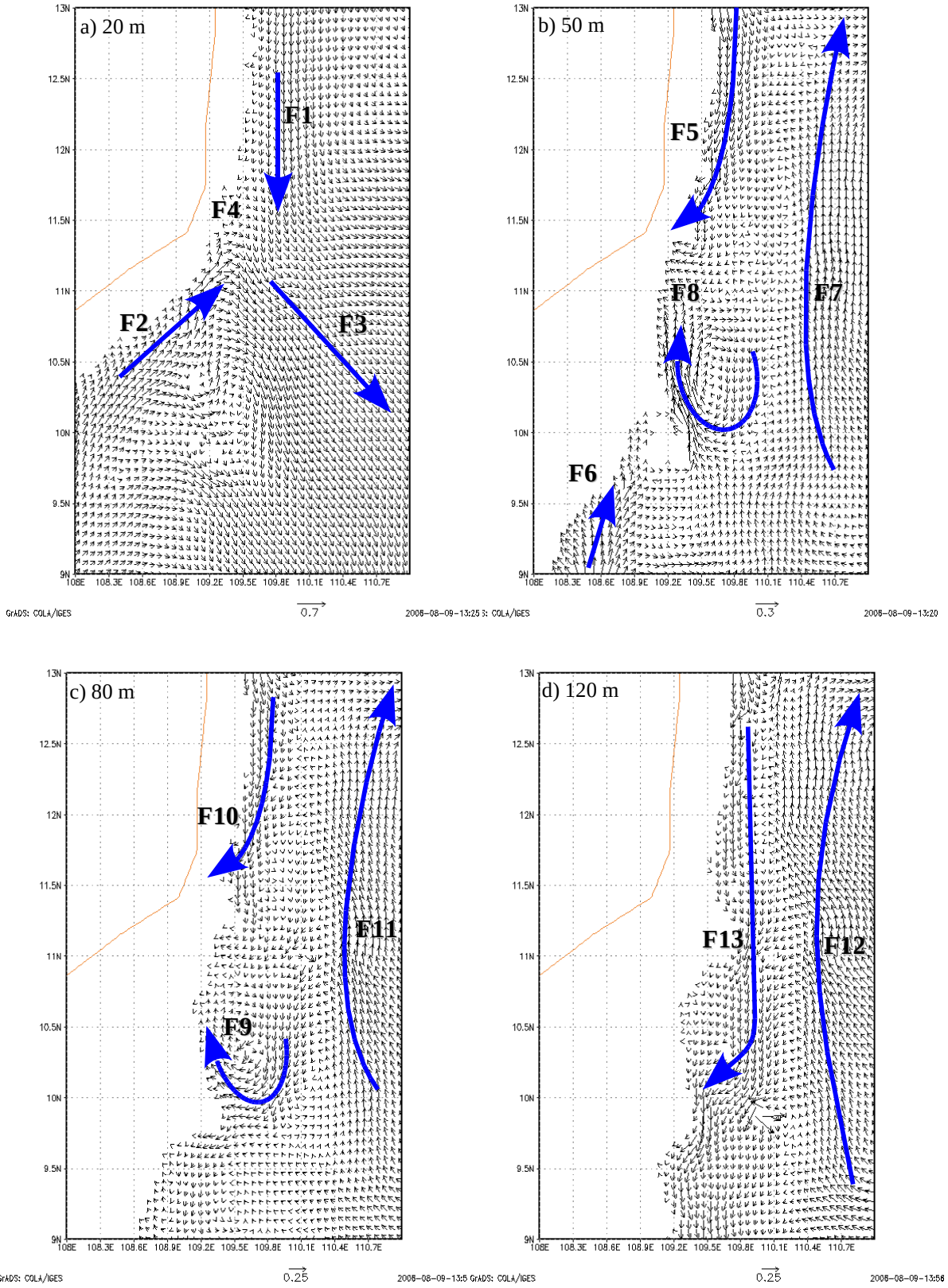

Fig. 5.6: The horizontal circulation reproduced by the model during state 6, the main currents are highlighted with arrows, units: m s^{-1}

5.2 Vertical Velocities in the VUA

The different horizontal velocities of each state affect the vertical velocities. This section will present the areas that show upwelling or downwelling. For illustration, a horizontal distribution of vertical velocities and three vertical slices are shown for every state. The horizontal distribution is defined as the average vertical velocity through the water column down to 250 m. This allows for a good view of the structures on the shelf. In the figures, blue areas illustrate upwelling, red areas downwelling. The position of the three slices is the same for all states and can be seen in the horizontal distribution.

Of the vertical slices, one is in alongshore direction (S1), to illustrate the alongshore components of the upwelling process. In this slice the isolines show the cross-shelf component of the flow, while the arrows indicate the along-shelf and the vertical velocities. The other two slices (S2, S3) show the cross-shelf direction, perpendicular to the coast. In these slices, the isolines show the along-shelf component of the current, while the arrows describe the velocities in the cross-shelf and vertical directions. These figures indicate circulation cells perpendicular to the coast.

The times used for each state are the same as those for the horizontal velocities. As in the discussion of the horizontal velocities, the described features are numbered with F1, F2, F3, etcetera.

Fig. 5.7a shows the distribution of the vertical velocities of state 1. First, it illustrates a mixed set of upwelling and downwelling. Due to the northeast monsoon and Ekman transports, during this state, one would expect to find downwelling at the coast. However, there are two areas where positive (upward) vertical velocities with a value of more than 10 m day^{-1} can be found (F1, F2). Both areas extend across the whole shelf and, surprisingly, both touch the coast. Moreover, F2 shows a maximum at the coast. The alongshore slice (fig. 5.7b) shows a strong upward-flowing current (F3) around 11° 30' N, following the slope of the ridge. Slice 2 (S2, fig. 5.7c), which is in an orientation perpendicular to the coast, shows a nearly closed cyclonic circulation cell (F4) with downwelling near the shelf edge and upwelling off the shelf. Below 80 m the currents are directed offshore, with a small upward component (F5). At the shelf edge (F4) at a depth of 80 m (F5) the boundary current builds a second core (F6) with a maximum speed of O(110 cm s^{-1}). As suggested in the horizontal distribution of vertical velocities (fig. 5.7a), upwelling can be found (F7) on the shelf. Here, the velocities are directed upward through the whole water column, and in the upper 50 m are directed onshore. Hence, the necessary offshore compensation, to achieve the equation of continuity, takes place in the downstream direction. Slice 3 (S3, fig. 5.7d) is dominated by a strong downwelling circulation (F8) near the shelf edge and the

outer shelf. The vertical circulation rotates around the core (F9) of the current. In this slice, being further to the south, the velocities of the deeper core, with only O(80 cm s^{-1}), are lower than those of the northern slice. However, as in S2, near the coast, upwelling is present. Some part of the boundary current flows onto the Sunda Shelf, with a significant upward component.

The horizontal distribution of vertical velocities for state 2 can be seen in fig. 5.8a. A band of downwelling stretches along the coast (F1). Only at the edge of the Sunda Shelf (F2), weak upwelling at the coast can be found. Due to the lower dynamics in this state, the overall vertical velocities, both positive and negative, are lower than those of state 1. In the alongshore slice (fig. 5.8b) downwelling is obvious (F3), the same can be found in slice 2 (fig. 5.8c). A typical downwelling circulation (F4), with onshore flow at the surface and offshore flow beneath, is to be seen. It may be a special feature that the offshore current (F5) can be found down to 150 m, combined with only low vertical velocities below 50 m. A second deep core (F6) of the boundary current is present in this state as well, but the magnitude of the velocity is only one third of the corresponding velocity of state 1. Slice 3 (fig. 5.8d) shows the same strong downwelling (F7) at the outer shelf as in state 1, but the circulation is located closer to the coast. The weak upwelling, as it was discovered in fig. 5.8a, can be seen near the coast (F8).

During the third winter state (fig 5.9a), positive vertical velocities appear north of 11° N. At 11° 30' N an upwelling center (F1) with values higher than 10 m day^{-1} is present. At this position, the horizontal currents build an anticyclonic circulation with onshore flow in depths between 50 m and 80 m. In the north (F2), increased positive vertical velocities are to be found. At this position, the counter-current alone cannot explain such high values, but they may be a result of the combination with the anticyclonic rotation of the boundary current below. In the offshore region of the beginning of the Sunda Shelf (F3), also vertical velocities with values of more than 7.5 m day^{-1} can be found. At the shelf edge (F4, F5), a band of weak downwelling is present.

The alongshore slice (S1, fig. 5.9b) shows the offshore flow (F6) near the surface, as it could be seen in the distribution of horizontal currents. Beneath the offshore flow, a weak onshore flow can be found, with significant positive vertical velocities (F7, F8). The alongshore currents are weak compared to those of the two other winter states. The northern slice of the two perpendicular to the coast (S2, fig. 5.9c) shows strong upwelling on the shelf (F9), associated with offshore flow at the surface. On the outer shelf and off the shelf the flow is directed offshore through the whole water column (F10, F11). As it can be seen in the horizontal distribution of the vertical velocities (fig. 5.9a), in the south (S2, fig. 5.9d) in this state neither significant vertical nor cross-shelf flow is present.

The horizontal distribution of vertical velocities of the transition between the northeast

monsoon and the southwest monsoon (state 4), are illustrated in fig. 5.10a. A band of weak upwelling (< 5 m day^{-1}) develops along the coast north of 11° N. Stronger (> 7.5 m day^{-1}) upwelling (F1) can be found at the northwestern side of the mesoscalic eddy, which was detected in the horizontal velocities (fig. 5.4a, F3). A zone of downwelling (F2) can be found at the northern shelf edge. The alongshore slice (S1, fig. 5.10b) shows that the main upwelling (F3) takes place beneath the offshore flow of the mesoscalic anticyclonic eddy (F4). A second location with higher positive vertical velocities appears north of 12° N between 80 m and the surface (F5).

The first cross-shelf slice (S2, fig. 5.10c) shows a coastal upwelling region, which spans the whole water column (F6). On the outer shelf and off the shelf the entire flow is directed offshore (F7), with the strongest currents in the uppermost 60 m.

The southern slice (S3, fig. 5.10d) shows positive vertical velocities on the mid-shelf (F8), while in the outer shelf region the flow is directed onshore. This eastward current is strong near the surface and weak in depths below 60 m. Interestingly, the currents on the inner-shelf are directed offshore, without any significant vertical motions (F10).

In the fifth state, which is dominated by the northward boundary current, upwelling spreads along the whole coast, with vertical velocities of O(2.5 m day^{-1} – 5 m day^{-1}), which can be seen in fig. 5.11a. At some pronounced locations the vertical velocities are increased (F1, F2, F3). Offshore of F1 and F2, the horizontal velocities at the surface show a westward flow at the northern sides of the recirculation eddies (fig. 5.5a). Remarkably, upwelling in these regions can be found not only near the coast, but also across all the shelf (F4, F5).

The alongshore slice (S1, fig. 5.11b) illustrates that the strongest upwelling (F6) takes place beneath an offshore flow (F7). The deeper onshore flow (F8), further to the south, seems to compensate for the offshore flow in the cross-shelf direction. Evidently, the compensation does not necessarily have to be perpendicular to the coast.

Slice 2 (fig. 5.11c) shows a closed vertical circulation (F9, F10). But while near the bottom (F7) it is dominated by strong currents, both vertical and horizontal, the vertical offshore recirculation is weak. The upwelling appears at the inshore side of the boundary current, with a speed of more than O(80 cm s^{-1}) in the core. The third slice (fig. 5.11d) shows an offshore flow through the whole water column. Down to a depth of 80 m, around the core of the boundary current and near the shelf, the vertical velocities are intense. In these depths, the figure shows a slight downwelling off the shelf (F10). In intermediated depths, upwelling is present near the shelf, but no downwelling can be found offshore. Below, most of the currents are directed offshore, with only a weak positive vertical component near the bottom.

The horizontal distribution of the vertical velocities of the second summer state, state 6, is shown in fig. 5.12a. As in state 5, weak upwelling occurs almost along the whole coast, but

in contrast to the former state, here, the upwelling is only increased significantly at a single location. F1 shows a wide area of high vertical velocities of more than 10 m day^{-1}. This area is congruent with the confluence zone of the two boundary currents. In the two areas with the greatest variability of shelf depth, the vertical velocities can be found across the whole shelf (F2, F3). Just as on the shallow Sunda Shelf (F4), the upwelling is not only a coastal phenomenon. The vertical velocities in the southern region (F4) may be explainable with the on-shelf movement of the northward boundary current (fig. 5.6b, F6).

The alongshore slice (S1, fig. 5.12b) shows that in this state, in contrast to the fourth state, the upward-moving water comes from the north (F5, F6). This may be important for the property of the uplifted water. As it can be seen in the distribution of the horizontal velocities, the horizontal and vertical velocities are low in this area. Slice 2 (fig. 5.12c) shows upwelling near the shore (F7), combined with eastward flow in the upper 30 m. Below, the currents are slow and directed southward, with only a small vertical component (F8). As it can be seen in the horizontal distribution of the vertical velocities, strong upwelling (F9) near the coast takes place, in slice 3 (fig. 5.12d). The mesoscalic spiral-like eddy, which is present in fig. 5.6b, fig. 5.6c and fig. 5.6d, is displayed well at F10. The most striking vertical velocities are just at the inshore side of this eddy, supporting the theory that the southward boundary current rotates onshore at 10° 20' N and continues to flow in a spiral-like manner with a strong vertical component through the canyon-like structure.

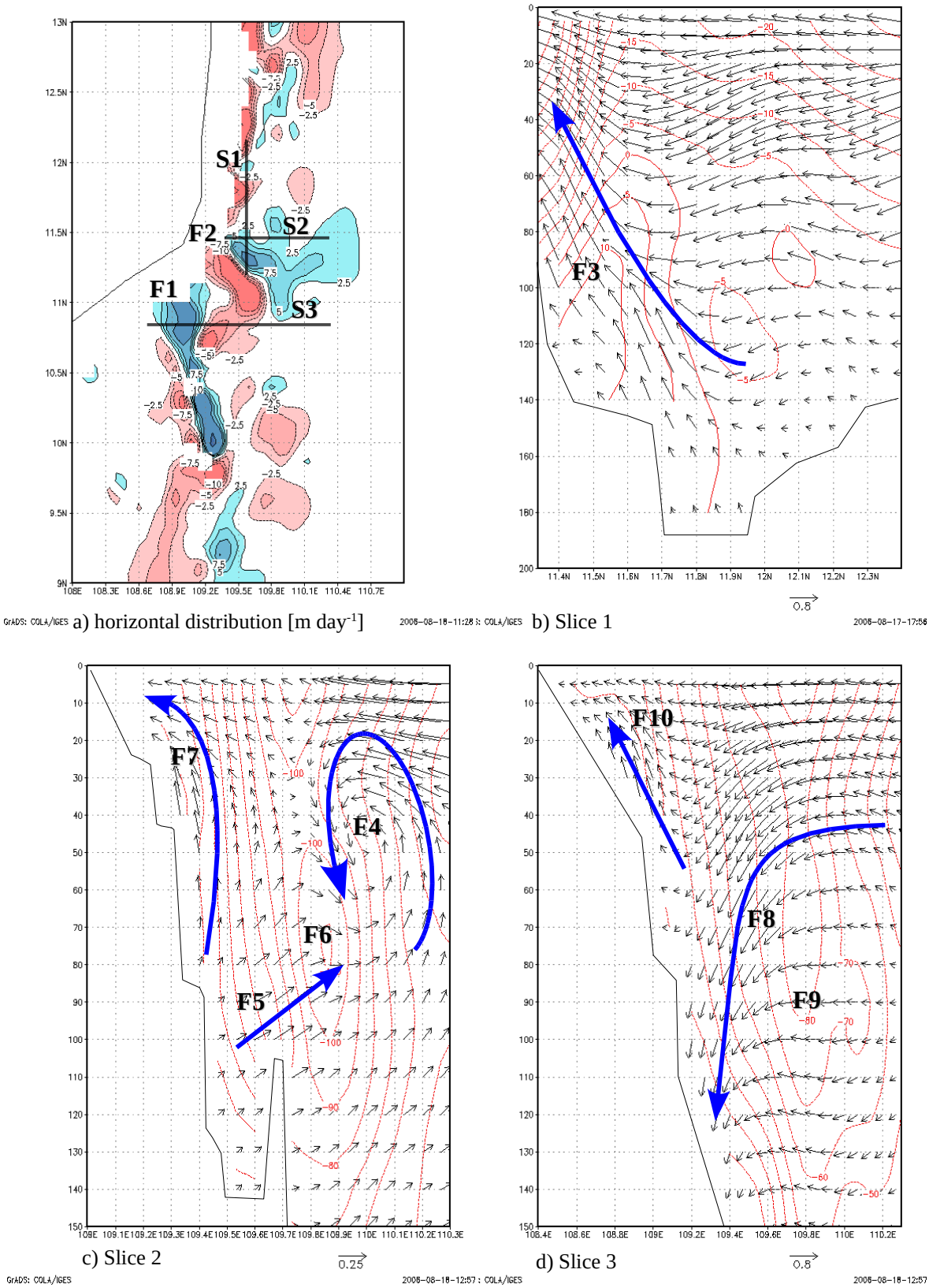

Fig. 5.7: The vertical and horizontal circulation reproduced by the model during state 1, the main currents are highlighted with arrows, units horizontal components: m s^{-1}.
Units vertical velocities a) m day^{-1}; b), c), d) m $hour^{-1}$

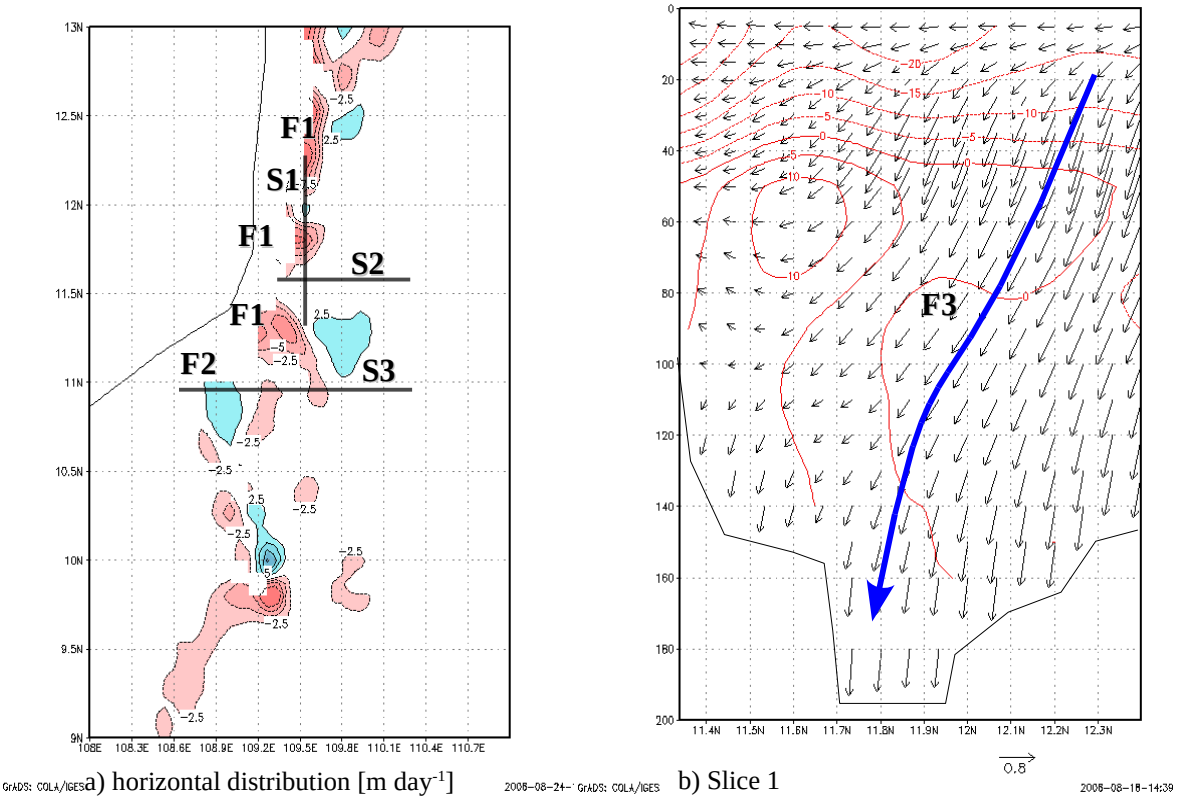

a) horizontal distribution [m day^{-1}] b) Slice 1

c) Slice 2 d) Slice 3

Fig. 5.8: The vertical and horizontal circulation reproduced by the model during state 2, the main currents are highlighted with arrows, units horizontal components: m s^{-1}.
Units vertical velocities a) m day^{-1}; b), c), d) m hour^{-1}

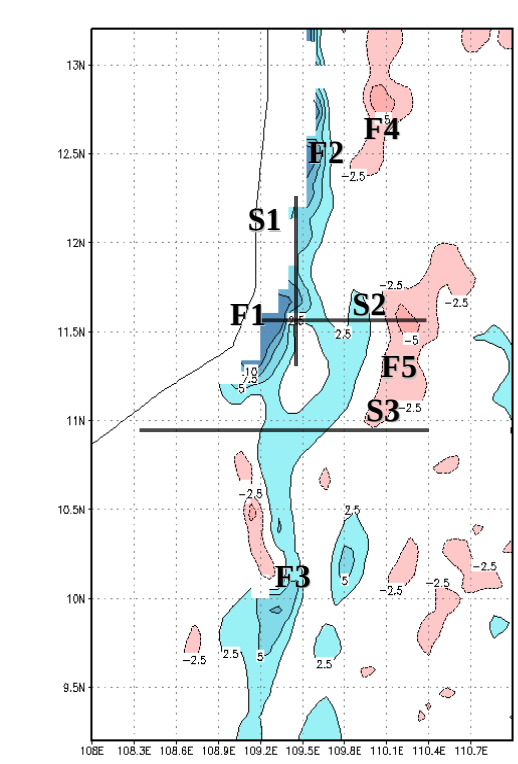

a) horizontal distribution [m day^{-1}]

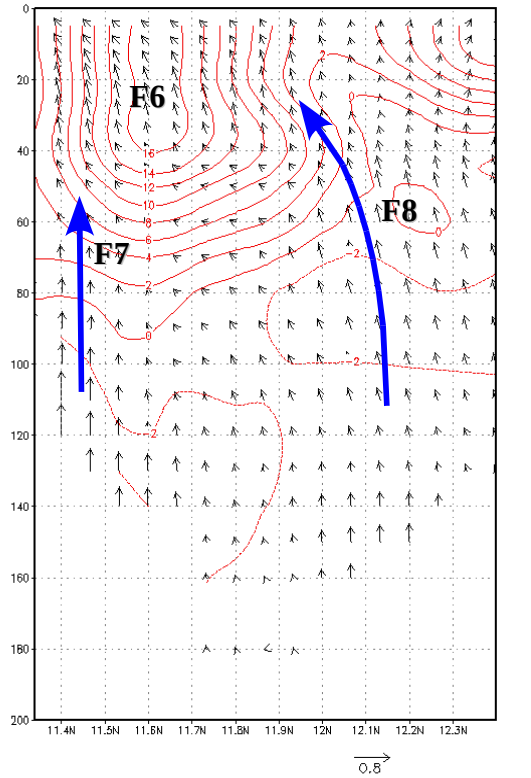

b) Slice 1

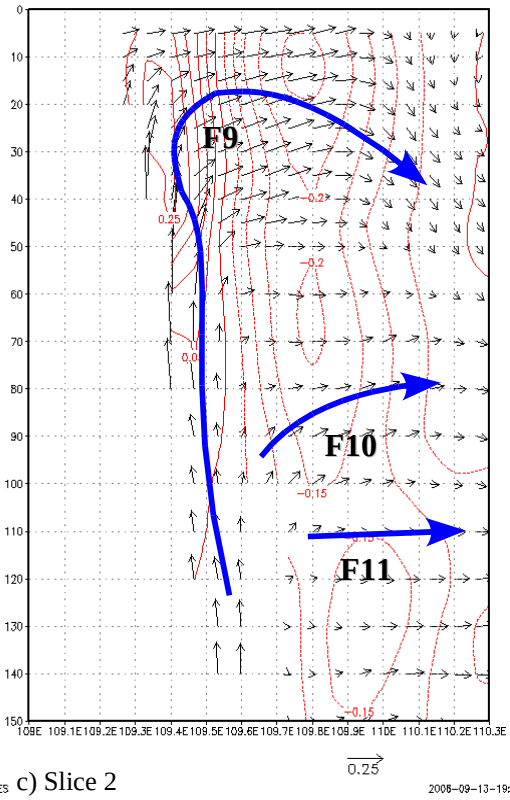

c) Slice 2

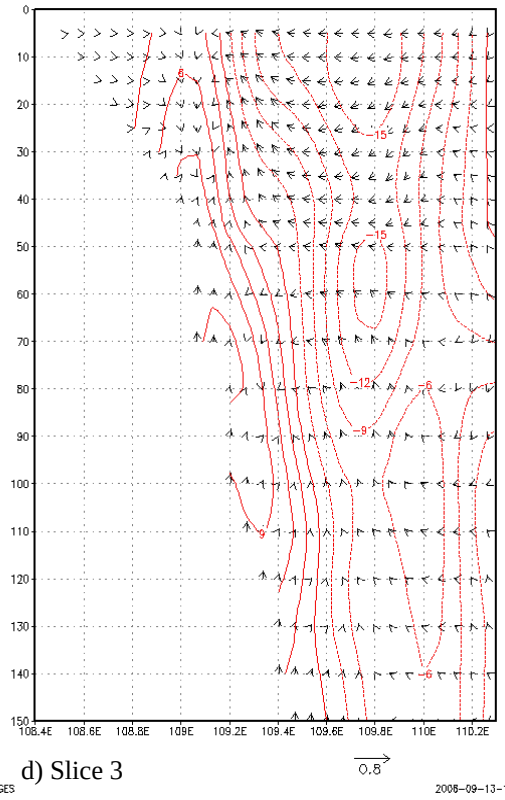

d) Slice 3

Fig. 5.9: The vertical and horizontal circulation reproduced by the model during state 3, the main currents are highlighted with arrows, units horizontal components: m s^{-1}.
Units vertical velocities a) m day^{-1}; b), c), d) m hour^{-1}

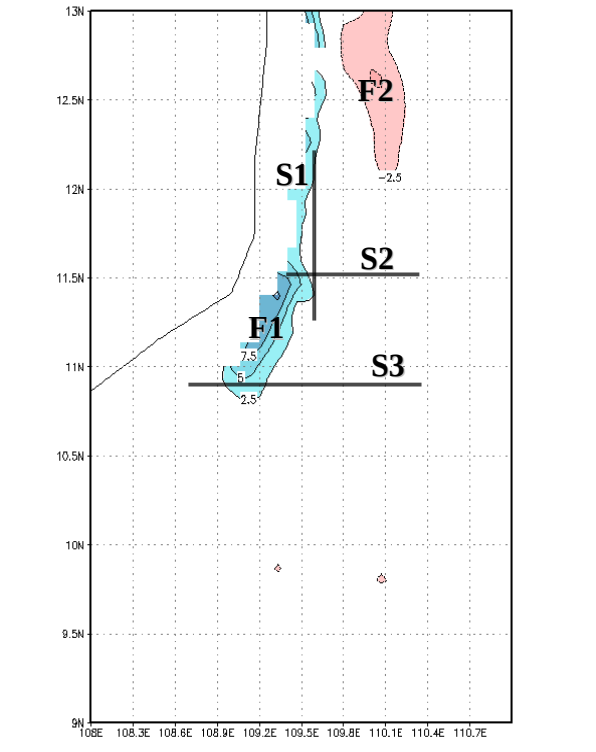

a) horizontal distribution [m day^{-1}]

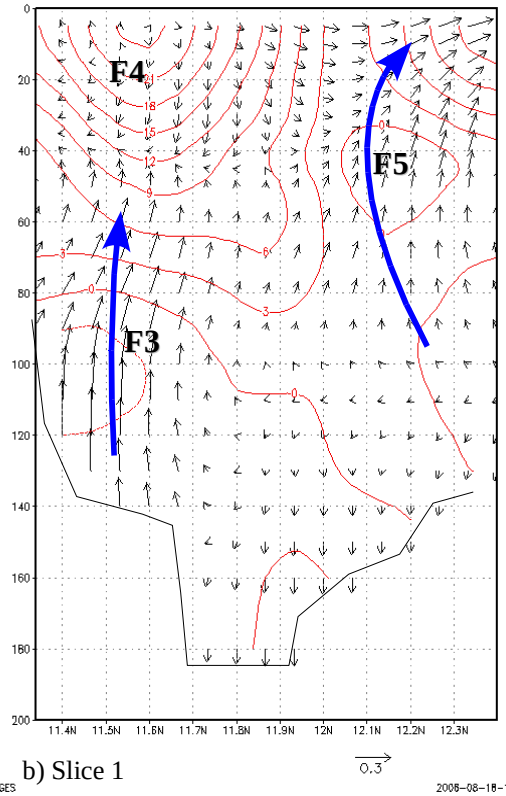

b) Slice 1

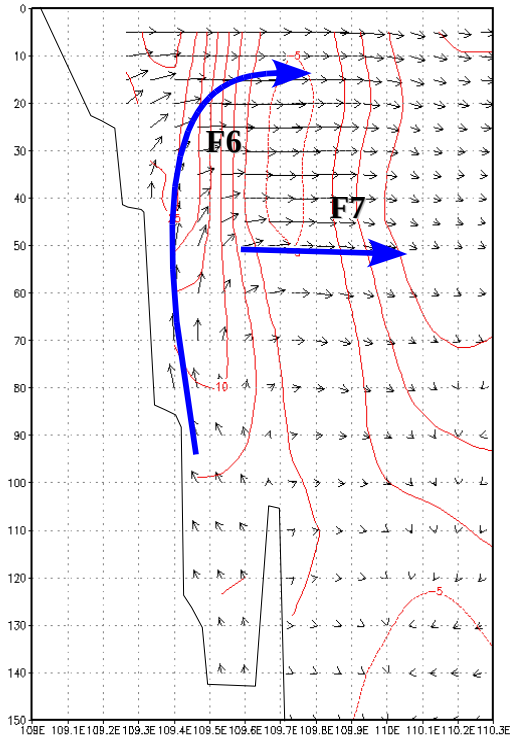

c) Slice 2

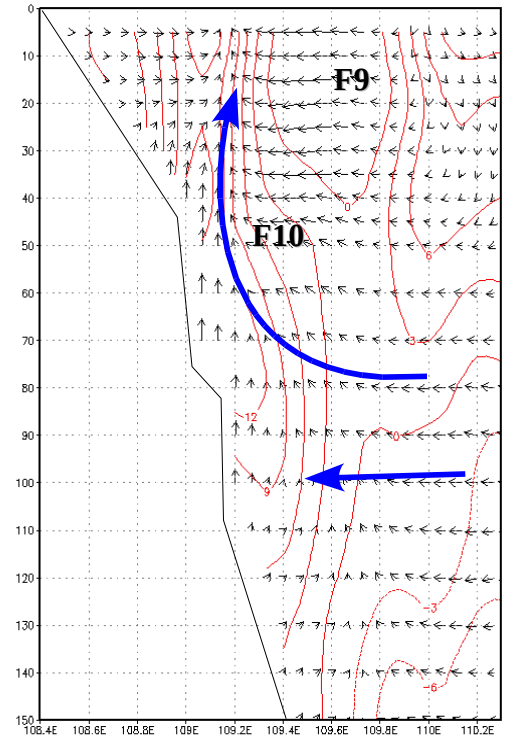

d) Slice 3

Fig. 5.10: The vertical and horizontal circulation reproduced by the model during state 4, the main currents are highlighted with arrows, units horizontal components: m s^{-1}.
Units vertical velocities a) m day^{-1}; b), c), d) m hour^{-1}

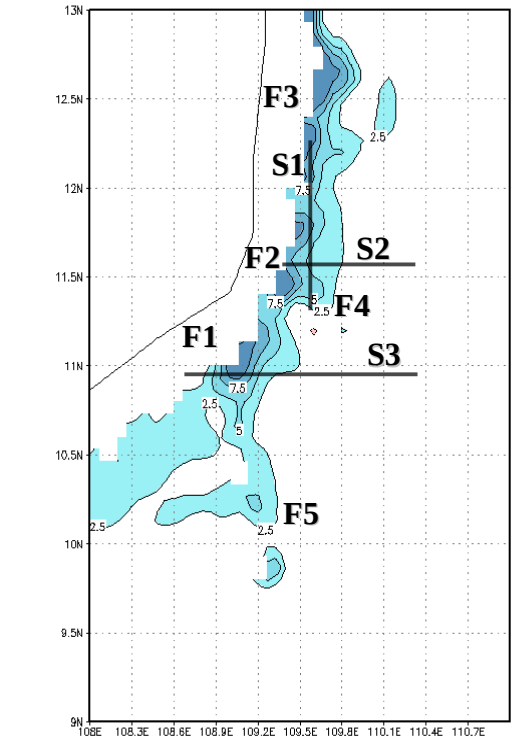

a) horizontal distribution [m day^{-1}]

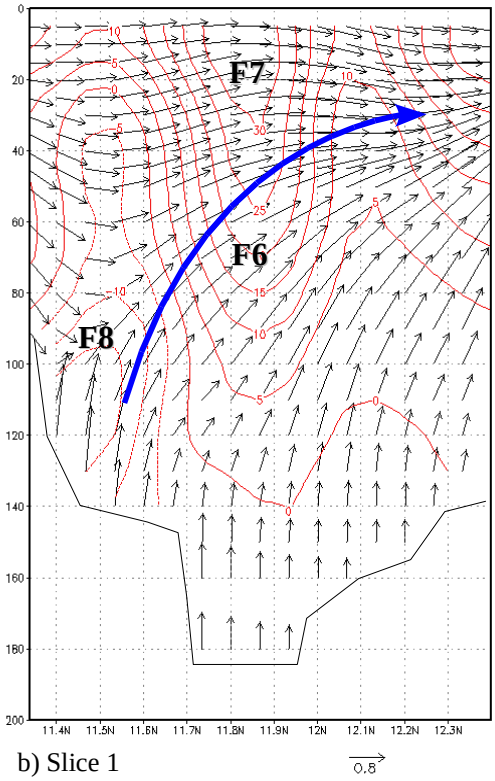

b) Slice 1

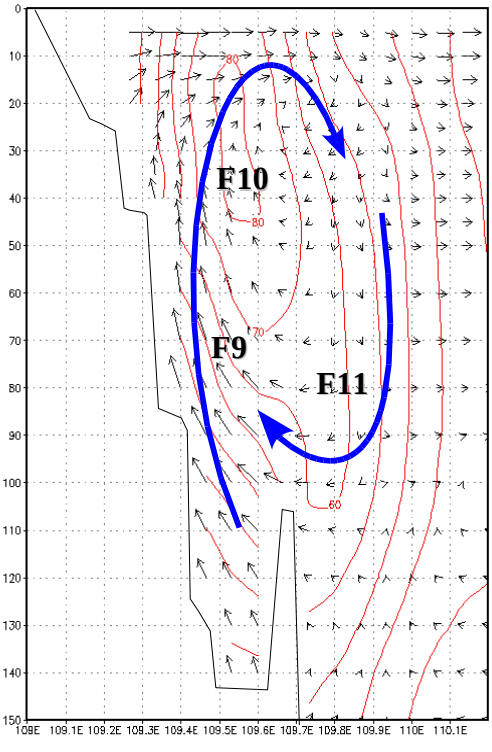

c) Slice 2

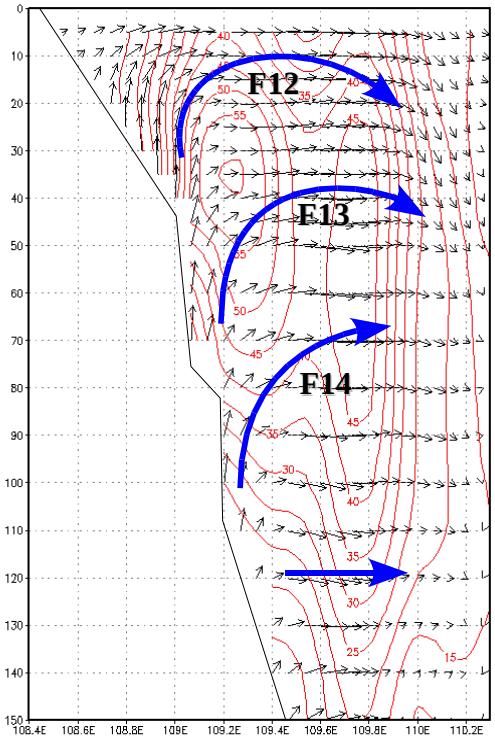

d) Slice 3

Fig. 5.11: The vertical and horizontal circulation reproduced by the model during state 5, the main currents are highlighted with arrows, units horizontal components: m s^{-1}.
Units vertical velocities a) m day^{-1}; b), c), d) m hour^{-1}

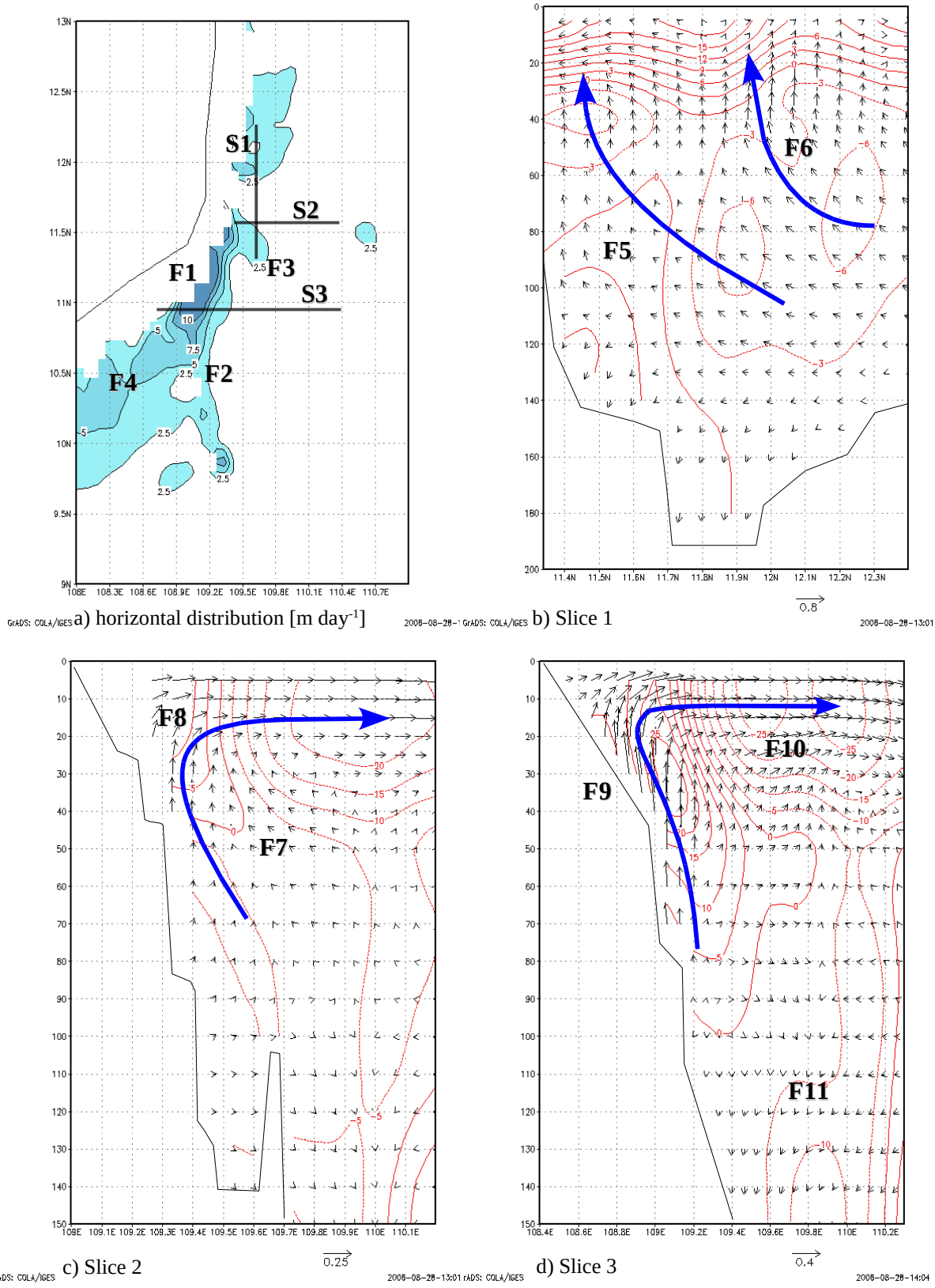

a) horizontal distribution [m day^{-1}] b) Slice 1

c) Slice 2 d) Slice 3

Fig. 5.12: The vertical and horizontal circulation reproduced by the model during state 6, the main currents are highlighted with arrows, units horizontal components: m s^{-1}.
Units vertical velocities a) m day^{-1}; b), c), d) m hour^{-1}

5.3 Classification of the vertical circulation

In this section the distribution of the vertical velocities found in the last section will be classified by comparison to other upwelling areas in the SCS and at western boundaries in general.

Incontrovertibly, all states have the ability to produce positive vertical velocities, except for state 2. Surprisingly, upwelling takes place in pronounced areas even in winter and spring. During summer, upwelling appears along the whole coast, even though, outside the pronounced areas, only at low velocities (< 5 m day^{-1}). The magnitude of the vertical velocities at the pronounced locations are in the same range O(> 10 m day^{-1}), both during summer and winter. During a strong northeast monsoon (state 1), the vertical velocities in these areas extend from the coast across the shelf. During summer, the upwelling is rather confined to the coast, but upwelling across the shelf is still present at the same positions as in winter. These locations share a strong gradient in the slope of the alongshore bathymetry. This leads to the conclusion that the topographic steering has an influence on the vertical velocities.

In spring the vertical velocities are slightly lower O(75 %) than those of the monsoon seasons. In mode 3, the distribution of upwelling is very similar to that in spring and is present north of 11° 30' N.

The magnitude of the vertical velocities simulated for state l are high, compared to other upwelling areas. For comparison, it is useful to mention the magnitude of the vertical velocities in other regions of the SCS and at western boundaries in general.

For the upwelling in the SCS northwest of Luzon, Jayvee et al. (2001) approximated a vertical velocity of 0.8 m day^{-1} by using the displacement of the 18°C isotherm between October and January. These values are comparable to the estimations of Shaw et al. (1996) who used a flow convergence scenario. However, Yang and Liu (2003) found vertical velocities of about 10 m day^{-1} at a depth of 500 m at the same position. The model of Cai and Lennon (1988) calculates values of 1 m day^{-1} – 2.5 m day^{-1} in the Taiwan Street. Chao et al. (1996) simulated vertical velocities of about 2 m day^{-1} – 6 m day^{-1} at the margin of the Sunda Shelf in November and Dezember at a depth of 200 m. With respect to the coarse resolution (0,4° in both horizontal directions), this is an impressive result.

Table 5.1 gives some examples of estimated vertical velocities for upwelling areas at western ocean boundaries. The average vertical velocities O(5 m day^{-1}) are comparable to those of eastern boundaries. Only in the Yucatan Upwelling Area the vertical velocities are in the same order of magnitude as those found in the VUA. However, the values may depend on the used method of estimation.

Vertical velocities $[m\ day^{-1}]$	***Region***	***Method***	***Publication***
≈ 4 - 6	East Australia	approximated from CTD and current measurements	Roughan and Middleton, 2004
≈ 3 - 5	Somalia	large scale hydrodynamic model	Schott et al., 2002
≈ 2 - 6	Northwest Arabian Sea	hydrodynamic model experiments	Keen et al., 1997
≈ 8 - 9	Yucatan Current	approximated from CTD measurements	Merino, 1997
≈ 4 - 6	average		

Table 5.1: The magnitude of upwelling at western boundaries

6
Ship experiments

6.1 Overview

In this project five cruises in the VUA took place, the first four on the Vietnamese vessel “RV Nghien Cuu Bien”, the last one on the German vessel “Sonne”.
The first cruise was in Juli 2003 (VG 3), and it is an example of the situation during a summer after an El Nino. Xie (2003) shows a correlation of the SST during summer with the ENSO during the winter 2002 / 2003, where was a warm phase of the El Nino Southern Oscillation (ENSO). However, the strength was incomparable lower then during the El Nino in winter 1997 / 1998.
The second cruise was conducted in April 2004 (VG 4). Thus it can be regarded as an example for the distribution of the hydrography during inter-monsoon.
The third cruise was conducted in summer 2004 (VG 7), which can be regarded as an example for a “normal” year, the winter before, the ENSO status was neutral. During both summer cruises (VG 3 , VG 7) a break phase within the summer monsoon season was present, thus the wind stress was noticeable lower than in the seasonal average.
The fourth cruise was carried out in March 2005 (VG 8). This cruise is to be seen as an example for the late winter monsoon situation. The cruise took place directly after a cold surge, i.e., a strong outburst of the winter monsoon. Offshore Vietnam a magnitude of the wind speed up to 30 m s^{-1} was observed.
The last cruise, on “Sonne” took place in April 2006 (SO 187/2). The main focus of this cruise was related to the Mekong river estuary. However, some stations have carried out in the upwelling area.
All observations were realised on a horizontal grid with a resolution of about 20 nautical miles. Fig. 6.1 illustrates the locations of the stations.

In the next sections the properties and relations of the water masses in the VUA are discussed. Moreover, the results of the hydrographic measurements, in horizontal sections as well as in vertical sections will be illustrated. Using the results from the reproduction of the simulation the hydrography is analyzed in more detail.
The surveys confirm several informations about the inter-anual, seasonal and spatial distribution of the upwelling.

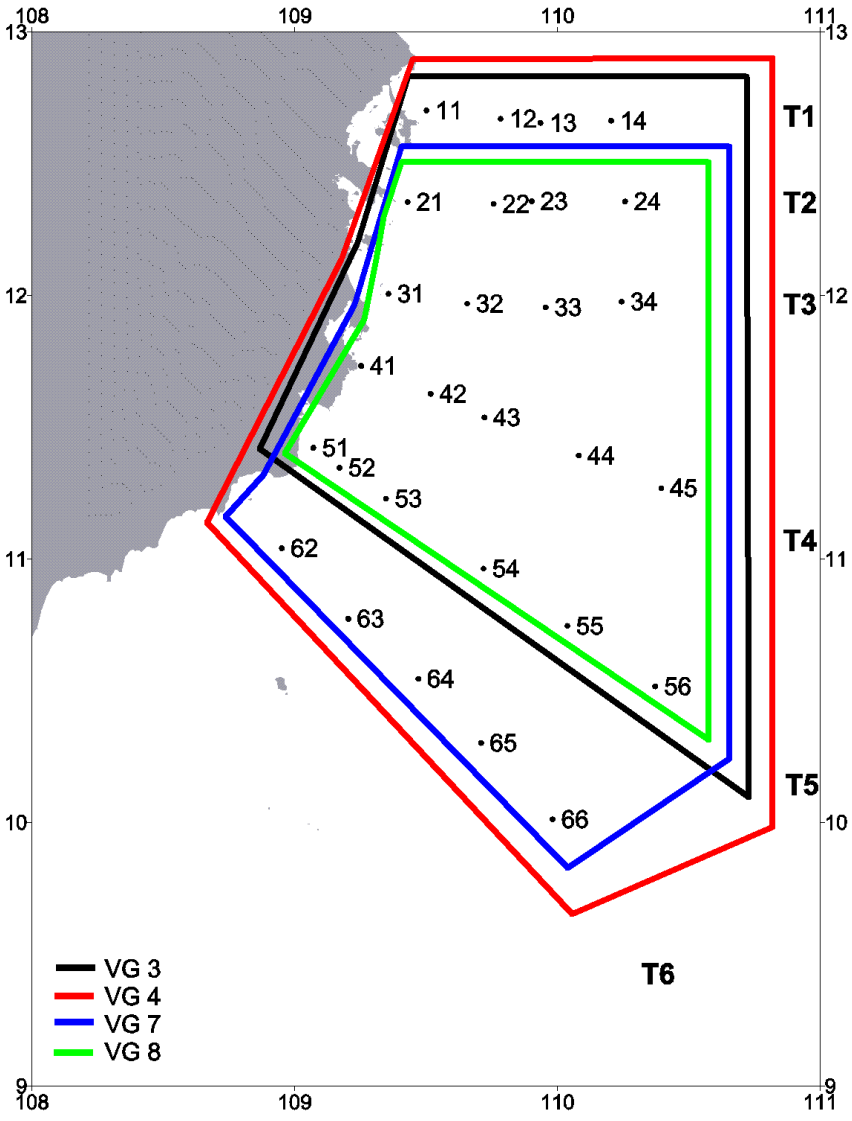

Fig. 6.1: Overall station map of the first four cruises.

6.2 Water Masses in the VUA

The CTD profiles of the first four cruises are plotted in an overall TS-diagram (Fig. 6.2). The figure reveals seven different water masses and several mixed water bodies. Tab. 6.1 illustrates the characteristics of the seven water masses. The main water source of the water in the SCS originates from the western Pacific. However, rivers and strong mixing processes modify the original water masses.

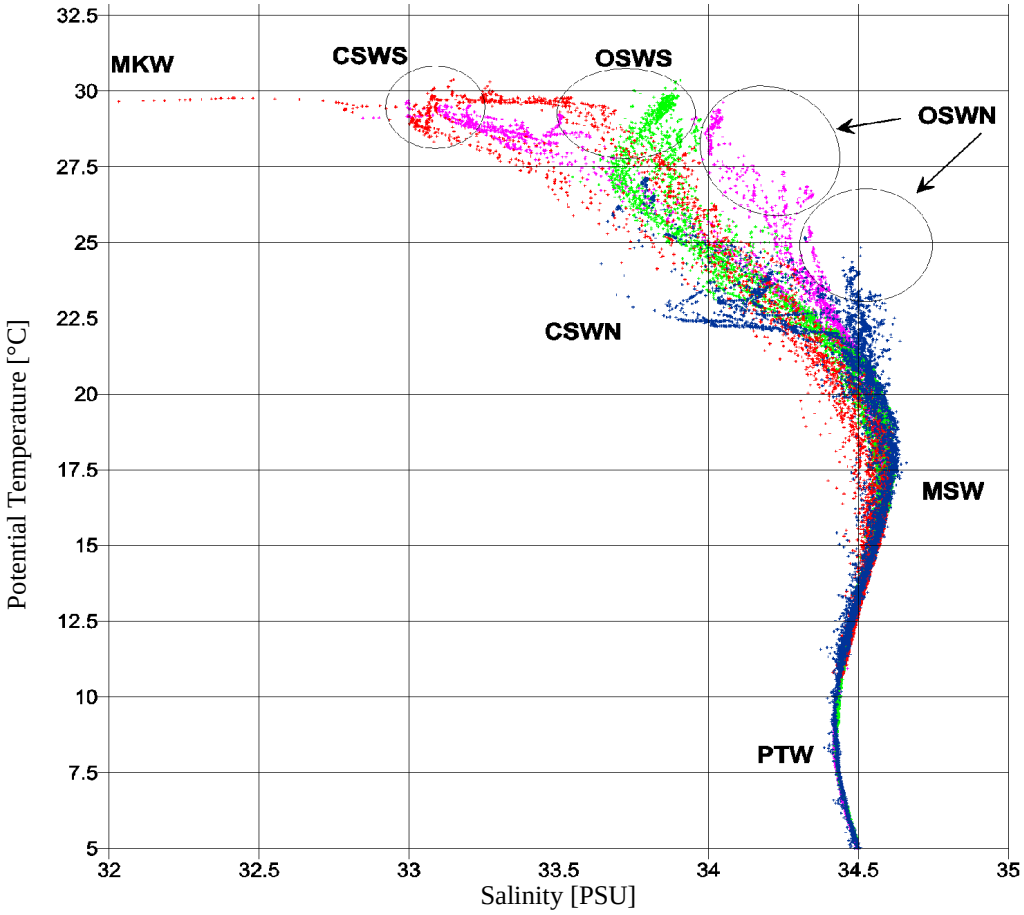

Fig. 6.2: Overall TS-Diagram of the first four cruises and the assigned water masses.
VG3: red, VG4: green, VG7: pink, VG8: blue

During a cruise in spring, by Rojana-Anawat et al. (2001), four of these water masses could be identified as Open Sea Water (OSW), Maximum Salinity Water (MSW), Permanent Thermocline Water (PTW) and Continental Shelf Water (CSW). Rojana-Anawat separated the CSW in two parts, one originating from the Gulf of Tonking in the north (CSWN) and one from the Sunda Shelf in the south (CSWS). During the observations of Ronjan-Anawat

the CSWN was present only north of 15° N. However, during the winter cruise (VG8) this water mass was found also in the VUA. The distribution of the salinity at the surface (0 m - 10 m) from the simulation two weeks before the cruise (VG8) illustrate the flow of the southward CSWN near the coastline to the south (fig. 6.3).

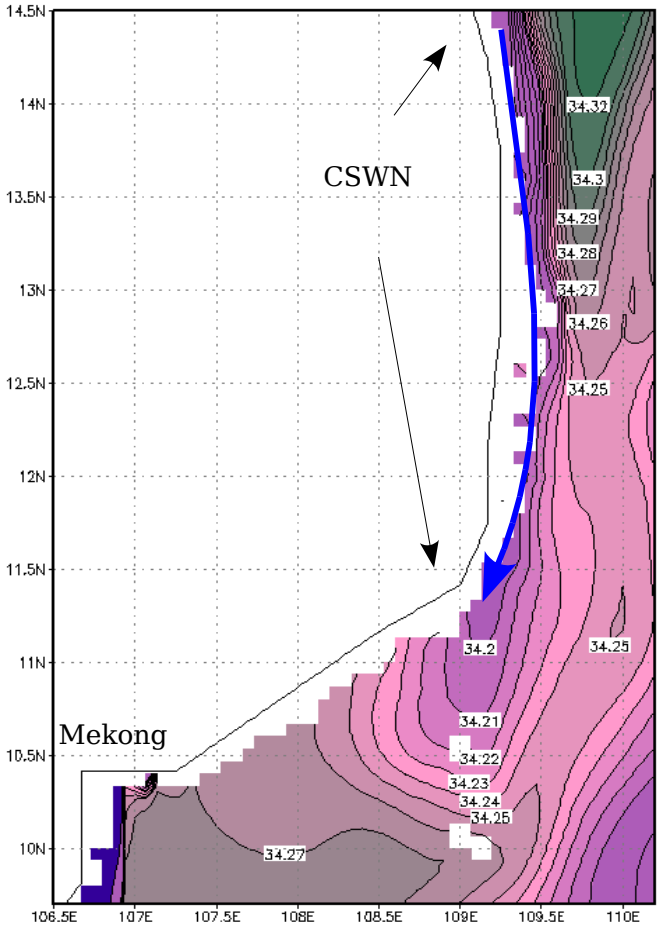

Fig. 6.3: Advection of the northern continental shelf water in the VUA during winter at 10m water depth. Units: PSU

In this project, CSWS was found during both summer cruises. During VG3 a water mass, influenced directly by the Mekong was present (MKW) on station 51, together with the OSW this water mass form the CSWS. Due to the lower salinity in the south of the SCS the OSW can divided into two parts, the Open Sea Water South (OSWS) and the Open Sea Water North (OSWN). OSWS originates from a mixing between CSWS and OSWN. The OSWN was found during VG7 and VG8. Due to the different seasons the temperature of the OSWN is of about 5°C colder during winter. OSWN was absent during VG4 and during VG3, which is can be explained by the existence of a anticyclonic circulation in the southern and central SCS during both records. OSWS were observed almost at all stations during VG4 and on the most south-eastern stations during VG3 and VG8. During VG7 on the

south-eastern stations CSWS was found, the strong offshore jet of state 6 of the horizontal circulation (chapter 5) transports the CSWS far offshore. Interestingly, a mixing between CSWS and OSWS was found during VG 3 but not between CSWS and OSWN during VG 7. At the later cruise, the uplifted water is was seen between CSWS and OSWN, thus a mixing is not possible because the two water masses do not directly adjoin. The MSW shows only a marginal difference in the southern and the northern of the SCS. During VG7 and VG8 MSW is advected from the north. In contrast the MSW during VG3 and VG4 is transported from the south, thus the salinity is slightly decreased.

Water-mass	**Depth (m)**	**Temperature domain [°C]**	**Salinity domain [PSU]**
MKW	0 -20	≥ 28	≤ 32.5
MSW	50 - 200	$15 \leq x \leq 20$	≥ 34.5
PTW	150 - 300	< 15	$34 \leq x \leq 34.5$
OSWN	0 - 80	≥ 27 (summer) $23 \leq x \leq 25$ (winter)	≥ 34
OSWS	0 - 80	≥ 28 (summer) ≥ 27 (winter)	$33.5 \leq x \leq 33.8$
CSWN	0 - 40	$22.5 \leq x \leq 25$	≤ 33.8
CSWS	0 - 50	≥ 28	$32.5 < x \leq 33.5$

Table 6.1: Water-masses in the VUA as deducted from the overall TS-Diagram

Fig. 6.4. illustrates the relations between the water-masses in the VUA. Particularly on the Sunda Shelf complex mixing processes occur. Likely due to tidal stirring, the Mekong discharge itself builds together with the CSWS the MKW. The CSWS itself originates from mixing of the MKW with the OSWS or OSWN during summer or winter, respectively. However, the OSWS is not independent of the CSWS as it originates from mixing between OSWN and CSWS.

The processes behind this complex modification of the water masses on the Sunda Shelf, due to the riverine discharge is part of the second phase of the Vietnam project and will not discussed in this thesis.

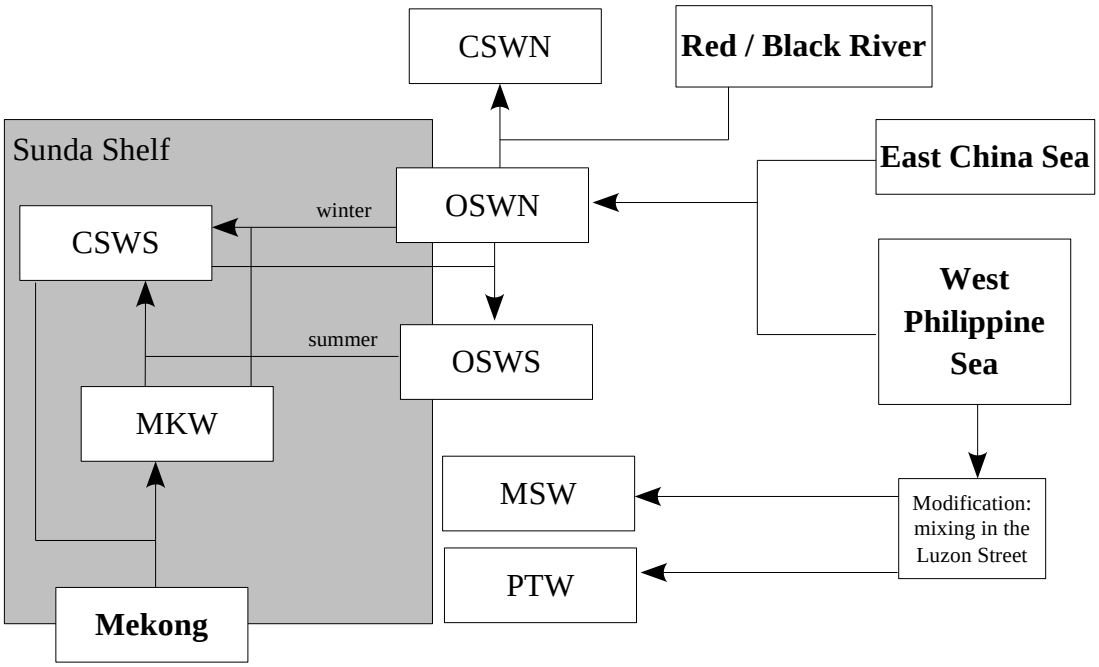

Fig. 6.4:Water-masses in the VUA, their origin and their relationship

Upwelling is always a process accompanied by stirring, i.e. the uplifted water are modified by mixting processes during and after the upwelling. Fig. 6.5 illustrates the origin of the upwelled water (UW) which is a combination of different water masses during each cruise. During VG3 a simple mixing between CSWS and MSW could be observed. During VG 4 the anticyclonic eddy, which is illustrated in fig. 5.4d, transports OSWS onto the shelf, thus the UW is related to OSWS and MSW. During VG7 and due to the circulation of state 6, the UW has its origin in three water-masses: CSWS, OSWN and MSW. Due to the advection of CSWN into the VUA during winter the UW during VG 8 originates from mixing between CSWN, OSWN and MSW.

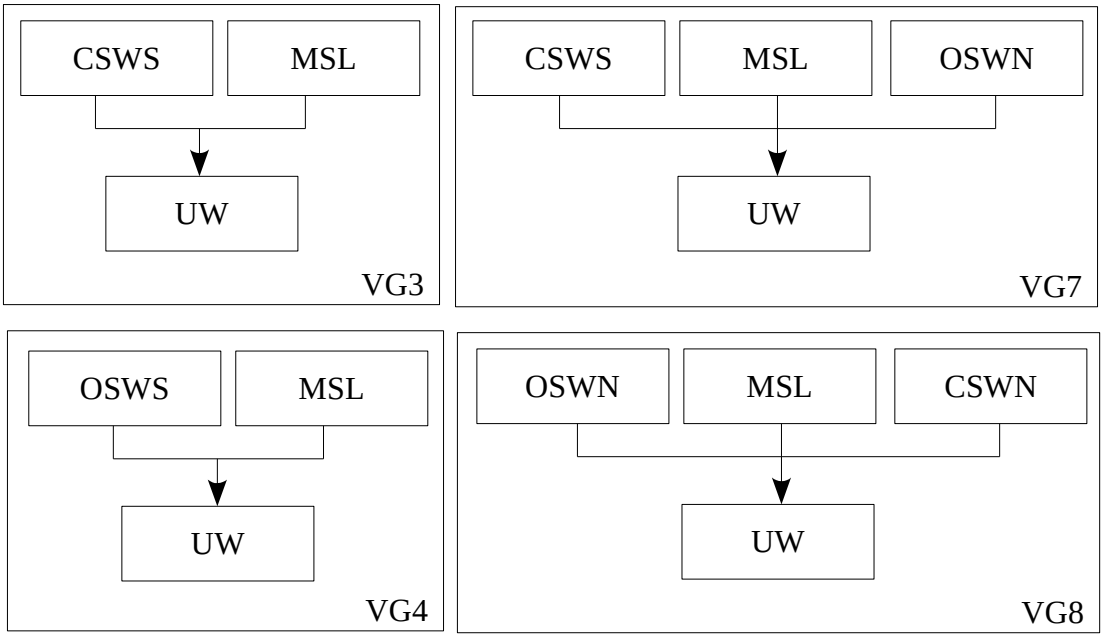

Fig. 6.5: The origin of the uplifted water during the cruises: VG3, VG4, VG7 and VG8

6.3 The summer cruises (VG 3 / VG7)

In this section the distribution of the hydrography, observed during the two summer cruises, is illustrated. During VG 3 (summer 2003) the focus is set on the sections T1 to T5 (fig. 6.1), which were surveyed in one closed leg. After this leg, two typhoons in the SCS with wind speeds of more the 30 m s^{-1} prevented offshore observations, only some stations on the Sunda Shelf were possible to accomplish.

During the first leg of VG7 (summer 2004) the sections from 2 to 6 were the object of research. In the second leg an alongshore section and a second observation of section 6 were realized.

With the results from the simulation (E0), a classification of the cruises is possible. In several figures of this section blue arrows illustrate the main currents of E0, as they were shown in chapter 5.

According to the results of the simulation the two cruises took place during two different states of the circulation, the cruise during summer 2003 (VG3) is related to state 5, whereas the cruise during summer 2004 (VG 7) is related to state 6.

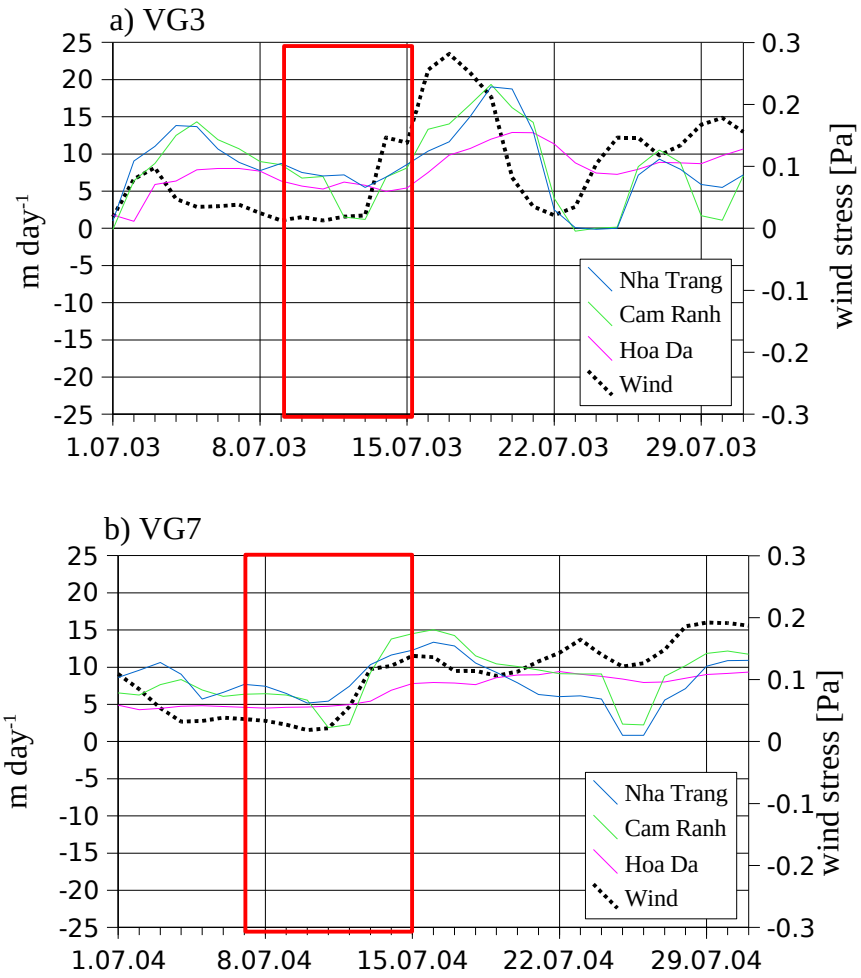

Fig. 6.6: Reproduction of the vertical velocities [m day^{-1}] from E0
and the alongshore wind stress (black dashed lines) during the cruises VG3 (a) and VG7 (b)

Fig. 6.6a illustates the vertical velocities for the regions, which are congruent with the observation area and the alongshore wind stress during VG3. The definition of the regions can be found in chapter 2. Fig. 6.6b illustrate the same parameters during VG7. The red boxes illustrate the period of the first leg of the cruises.

The wind-stress shows that both cruises took place during a monsoon break. Thus, the wind-stress is relatively low. The vertical velocities are O(7 m day^{-1}) during VG3 and O(6 m day^{-1}) during VG7, i.e. in a comparable range. The average vertical velocity reproduced by E0 during summer (June, July and August) is O(9 m day^{-1}).

During VG3 current observations on each station took place. The distribution of the vertical averaged current are presented in chapter 4 (fig. 4.3).

Figure 6.7a – 6.7e presents the vertical distribution of temperature on the sections T1 to T5 at VG3 perpendicular to the coast. An upward tilting of the isotherms to the coast at all sections was observed, with the strongest tilt angle of the isotherms can be found in section T4. Interestingly, at the inshore stations 41, 21 and 11 beneath a depth of 50m a downward tilting of the isotherms is illustrated. At this stations a southward undercurrent was observed. The vertical sections T1 to T4 illustrate that the cold band of water moves slightly offshore toward the north and the sharp front which exists in the south is more diffuse in the north. Fig. 6.7f, 6.7g shows the vertical distribution of salinity perpendicular to the coast at section T1 and section T5. At the southernmost section (T5) a clearly defined plume of water with low salinity exist near the coast. This plume is shifted offshore in the northern section (T1).

Fig. 6.4a shows the distribution of temperature at 20 m depth. A cold band of water exists at the inshore stations (station 51, station 41, station 31, station 21, station 22, station 11 and station 12), which expands more offshore towards the north. This correlates well with the offshore shift of the boundary current, which was observed and simulated (fig. 4.3). The blue arrow shows the main pathway of the boundary current from the simulation of E0.

The station with the coldest temperature at 20 m depth was observed on station 41 with a temperature of O(24°C), offshore the temperature is O(29°C). Hence, a cooling of the water of about 5°C due to vertical advection can be assumed. Moreover, the slight offshore movement of the cold water to the north is visible, as well as in the vertical sections. In the distribution of salinity (fig. 6.8b) a low salinity plume, flowing thought the area can be observed. The lowest salinity is less than 32 PSU on station 53. Following the plume to the north, the low salinity is mixed to a value of 33.2 PSU and the sharp front of the plume disappear in the north. With respect to the deducted water bodies this water is directly influenced by the Mekong river. Comparable to the temperature distribution, a band of high salinity with values of more than 34 PSU exist near the shore.

At 40 m depth (fig. 6.8c) the coldest temperatures were observed at the stations 51, 41 and 31. The distribution of salinity (fig. 6.8d) at 40 m depth suggest a offshore movement of the low salinity water.

At 80 m depth (fig. 6.4e), a band of colder water is present near the coast, which extends parallel to the coast. The magnitude of the strongest temperature difference is O(7°C), with the coldest water can be found at station 41 and station 21. At 150 m depth (fig. 6.4f) the water was observed 2°C colder in the northwest than in the northeast.

The distribution of temperature and salinity perpendicular to the coast observed during VG7 are presented in fig. 6.9. The distribution of the temperatures along T2, T3, T4 and T5 are displayed in fig. 6.9a - 6.9d. As in fig. 6.3 the isotherms tilt upward in the direction of the coast, with the strongest slope at T3 and T4. Although, the temperatures at the surface are lower (O(24°C)) than at VG3 (O(26°C)) the inclination is clearly smaller. During VG3 the UW advects with a strong alongshore component, whereas during VG7 the currents are

directed more offshore. Thus, in the sections perpendicular to the coast during VG 7, UW was observed not only near the coast but also offshore.

The distribution of salinity of section 5 suggests that during VG7, the low salinity plume exists more offshore and is more salty (> 33 PSU), than during VG3 (< 33 PSU).

The offshore advection of the UW is well illustrated in the horizontal distribution of the temperature at 20m depth (fig. 6.10a). The difference between UW and the offshore water is approximately 6°C. During the cruise in summer 2004 (VG 7) the UW does not form an alongshore band, but the cold water spreads over the shelf. At station 42 an upwelling jet (blue arrow) in the direction of station 24 is indicated. The horizontal distribution of the salinity (fig. 6.10b) illustrates the same offshore movement of the high salinity water in the northeastern direction. According to the results of the simulation, station 31 and station 41 are in the region where the two boundary currents confluence. At 40 m depth, the distribution of temperature (fig. 6.10c) and salinity (fig. 6.10c) are similar to that at 20 m, with the difference that the area of cold and saline water is extends further to the north. The distribution of temperature at 80 m depth (fig. 6.10d) discovers well the influence of the different states of the horizontal circulation. While at VG3 the gradient of the temperature at 80 m is directed parallel to the coast, that of VG7 is more perpendicular to the coast. The temperature field at 150 m depth prevents the peculiar pathway of the southward boundary current at state 6 of the simulation.

VG7 gave the possibility to observe section T6 twice (8.7.2004 and 21.7.2004). Fig. 6.6b illustrates that the first measurement of this section was performed during a monsoon break and the second during an active monsoon. During the active monsoon the vertical velocities of E0 are twice them during the monsoon break. The distribution of the temperatures of both observations validate the stronger magnitude of the upwelling, hence the inclination of the isotherms is stronger during the second observation. However, the difference of both (observation 2 – observation 1) suggests, that near the coast, the temperatures are not significantly colder during the second observation. The stronger upward tilting of the isotherms is explainable with 3°C warmer water offshore. This warmer water is explainable by an strengthening of the northward boundary current. Due to that, the anticyclonic circulation becomes more important. This prevents downward mixing offshore in the center of the anticyclone. Second, due to the strengthening of the northward boundary current less colder water from the north will be transported to the south. This is also a reasonable explanation for the fact that during VG3, the observed UW was warmer than during VG7, although the vertical velocities are comparable.

The distribution of the salinity in section 6 from both observations shows, that with the strengthening of the northward boundary current, a significant plume of Mekong influenced water was observed inshore .

Although the wind-stress forcing differs only slightly between both summer cruises, the

observations discover a number of differences in the distribution of temperature and salinity. Moreover, the distribution of the temperature reflects the spatial distribution of the upwelling, but not the magnitude of the vertical velocities.

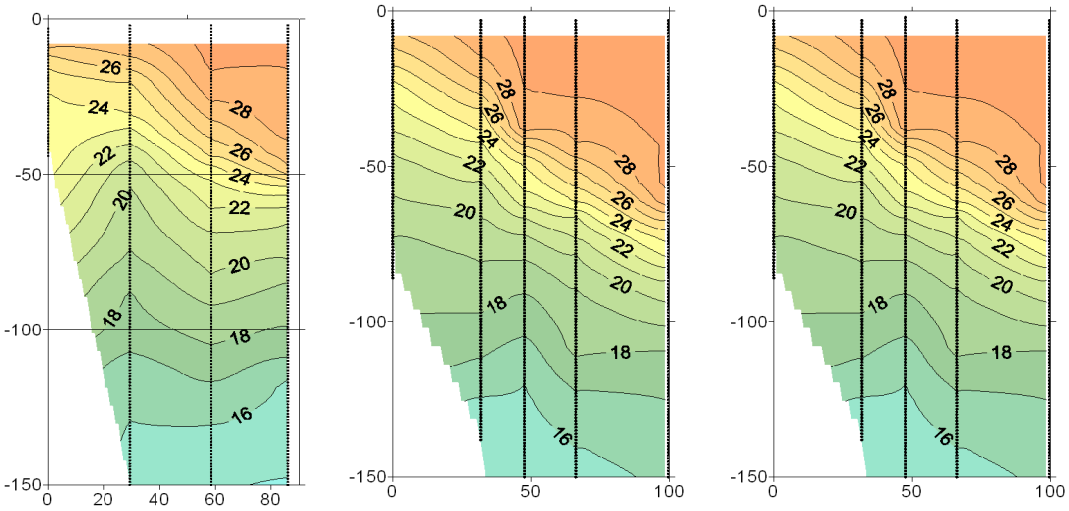

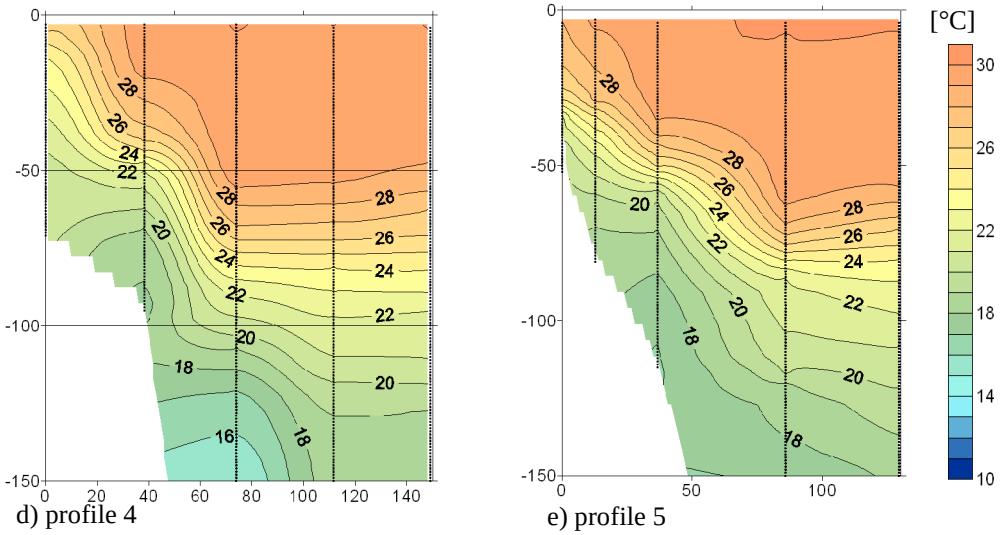

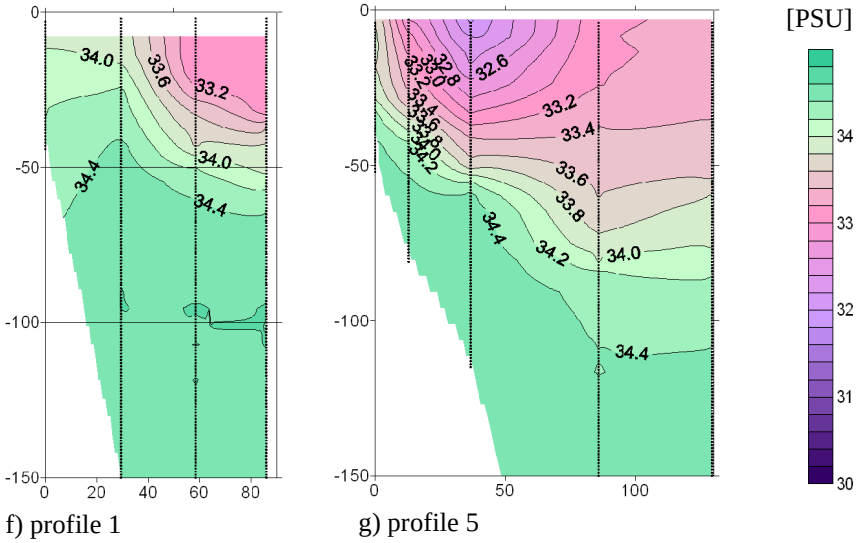

Fig. 6.7:Vertical sections of temperature (a, b, c, d) and salinity (f, g) at VG3

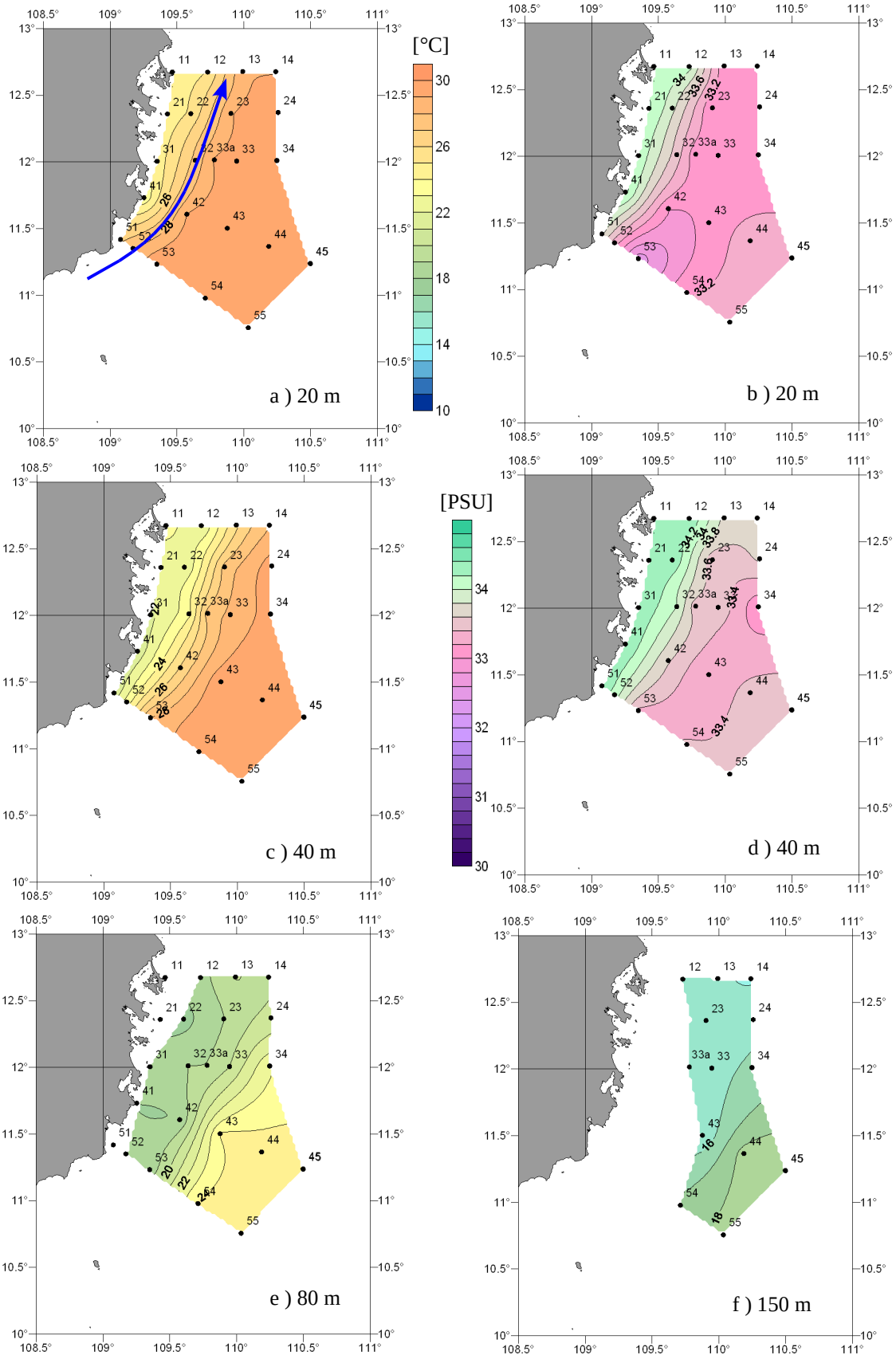

Fig. 6.8:Horizontal distribution of temperatures (a, c, e, f) and salinity (b,d) at VG3

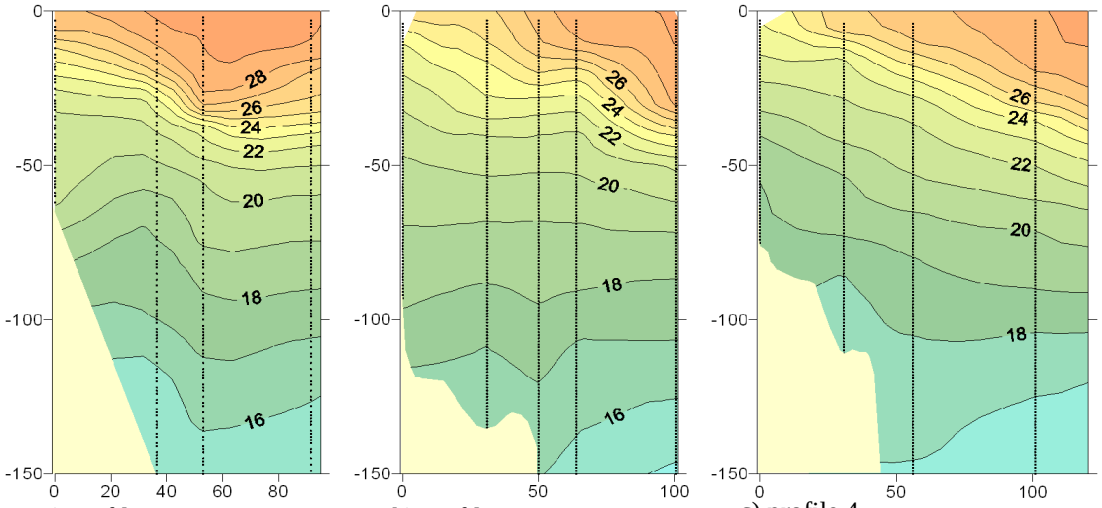

a) profile 2 b) profile 3 c) profile 4

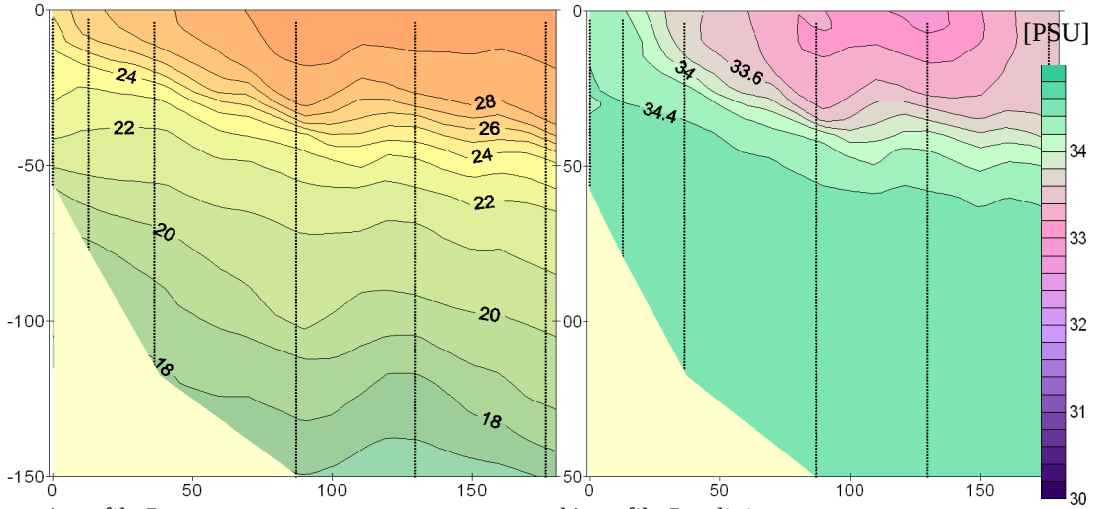

a) profile 5, temperature b) profile 5, salinity

Fig. 6.9:Vertical sections of temperature (a, b, c, d) and salinity (e) at VG7

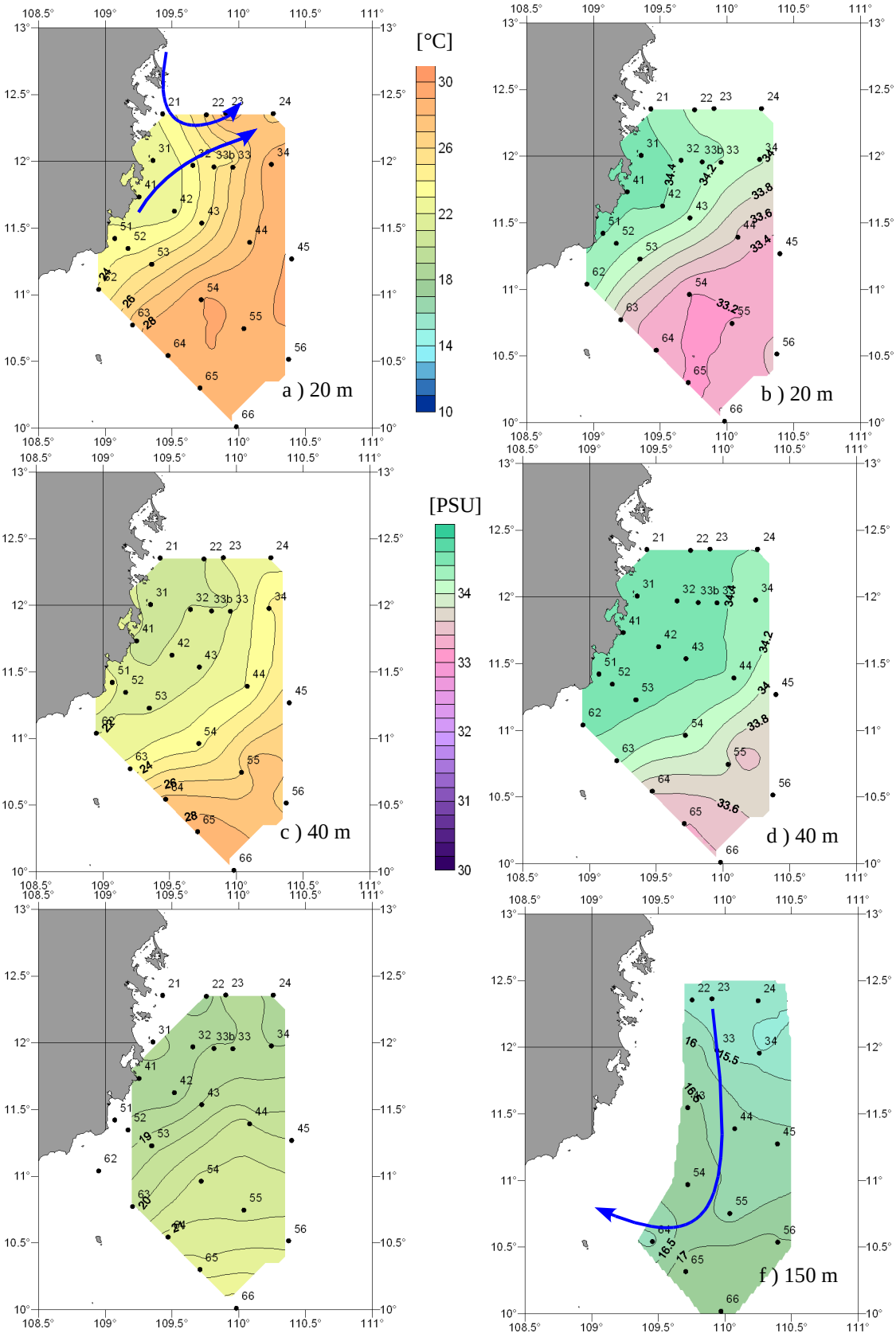

Fig. 6.10: Horizontal distribution of temperatures (a, c, e, f) and salinity (b,d) at VG7

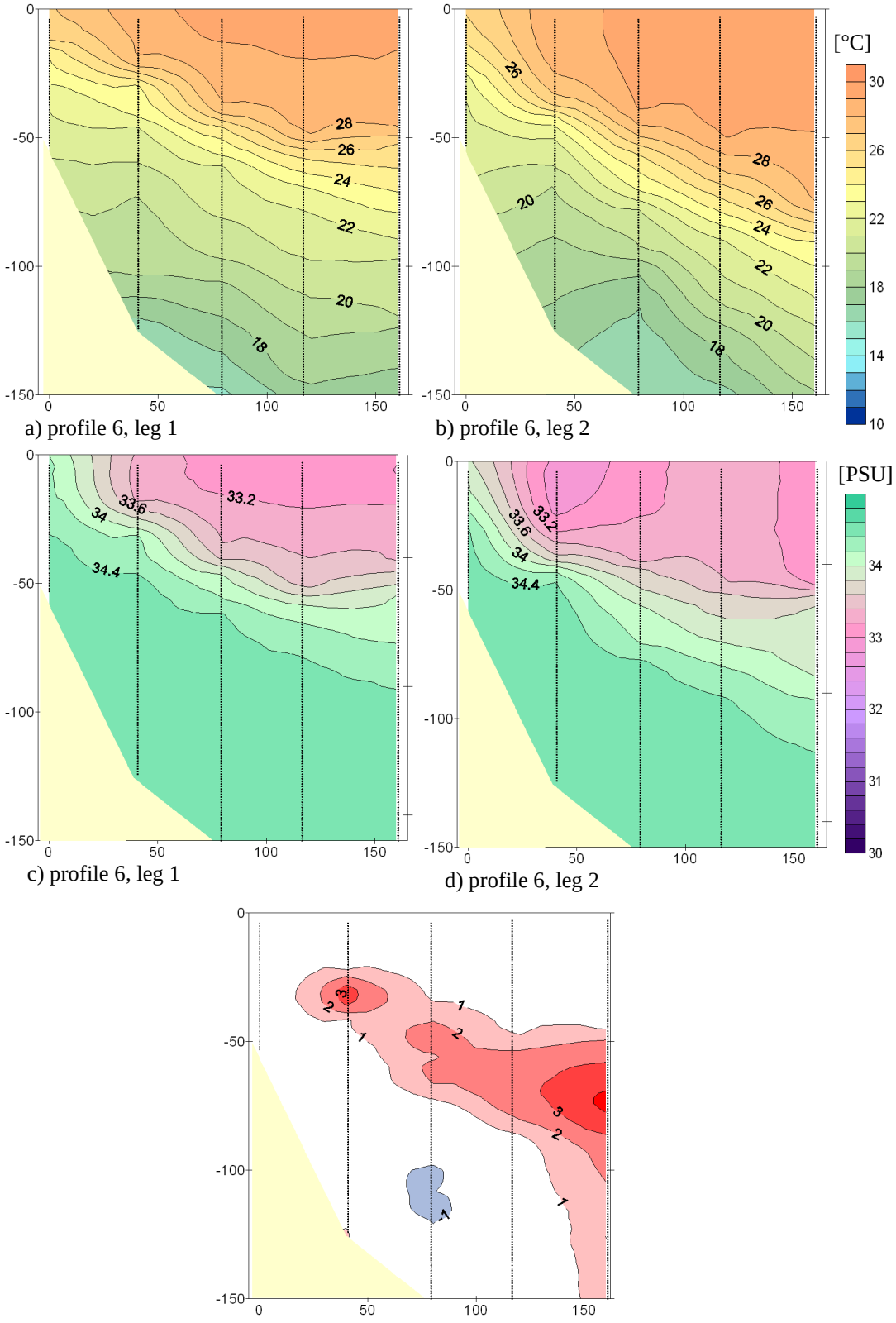

Fig. 6.11:Vertical section 6 of temperature (a) and salinity (b) at leg 1, temperature (c) and salinity (d) at leg 2 and the temperature difference (e) at VG7

6.4 The inter-monsoon cruises (VG 4 & SO 187/2)

Two inter-monsoon cruises in the VUA took place. Here the main focus is put on the cruise VG4. During SO 187/2 only a few observations in the VUA, and until now no numerical reproduction of this period, took place. At VG4 three more sections were observed in the north of the VUA, but they are not of hydrographic relevance, because they are located outside the upwelling region.

According to the result of the simulation, VG4 took place during the rapid change between state 4 and state 5. Hence, the offshore anticyclonic eddy is impinging onto the shelf and the northward boundary current starts to establish. The distribution of the reproduced vertical velocities during April 2004 of the Cam Ranh and and the wind stress in the along- and cross-shore direction are given in Fig. 6.12.

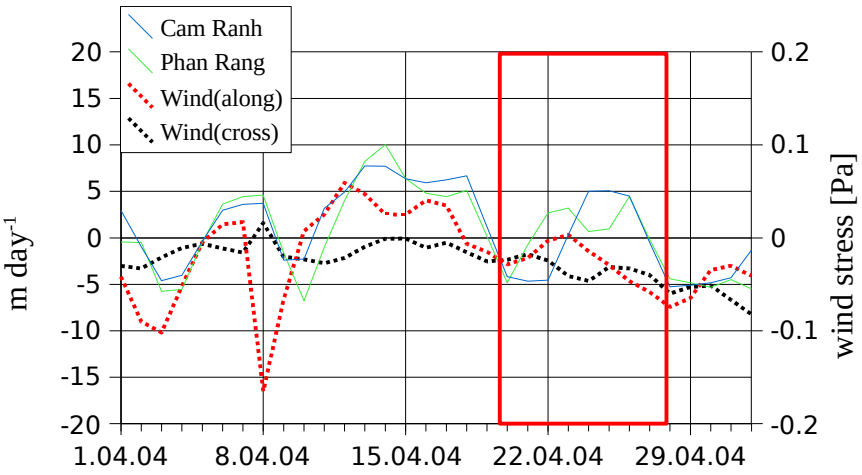

Fig. 6.12: Reproduction of the vertical velocities [m day^{-1}] from E0
and the alongshore and cross-shelf wind stress (dashed red and black line) during VG4

It can be seen that the cruise took place after an upwelling event, in accordance with a fully established state 4. The reproduced vertical velocities are O(6 m day^{-1}) for one week, hence they are comparable with the magnitude simulated during the summer cruises. During this upwelling event the wind was directed from southeast, hence in the positive alongshore direction with an onshore component. At the beginning of the cruise, the wind was directed to the onshore direction and rotates towards the northeast direction during the cruise. Contrary to the wind-stress forcing the vertical velocities of E0 are still positive with values in the average of O(3 m day^{-1}). Fig. 6.13a-e show vertical sections of temperatures perpendicular to the coast. The strongest upward tilting of the isolines can be found at section T3, further to the north (section 1) the upward tilting is only weakly visible. At section T4, near the surface a pool of warmer water can be found in the center of the section

and colder water near the coast. Section T5 shows a complex variation of the isotherms, a cyclonic eddy on station 54 might be suggested. On the southernmost section a significant upward tilting of the isotherms can be found not direct by the coast, but on the mid-shelf.
Fig 6.13f illustrates the distribution of salinity along this section. The isohalines demonstrate much clearer an overturning circulation and offshore advection of the uplifted water. Moreover, the upwelling reaches the surface only at section T4.
The horizontal distribution of the temperature (fig. 6.14a,c,d,e), super-imposed by the currents as they are simulated in E0, discovers the complex circulation during the cruise. The blue arrows illustrate an average circulation during this time. Because of the rapid change between state 4 and state 5, the variability of the currents is large during VG4. The offshore anticyclonic eddy is visible in the distribution of temperatures in the first 60 m, represented by a warm pool off the shelf. On the shelf the southward boundary current is displaced by the anticyclonic circulation. In the canyon-like structure the anticyclonic eddy vanishes. The circulation simulated by the model can help to explain the distribution of the temperature and the salinity. The complex structure of section T5 can be explained by the means of an offshore transport of the UW, originating from an upwelling event a few days before the cruise. This offshore advection is also responsible for the lower temperatures, which were observed on station 45. The distribution of the temperatures at 80 m depth indicate upwelling at the shelf-edge, due to the anticyclonic eddy (blue arrow).
The distribution of salinity at 20 m and 40 m depth (fig. 6.14b, c) confirms the same two upwelling areas, which have been deduced from the temperature field. Moreover, the offshore advection of the UW can be observed.
Although the second inter-monsoon cruise (SO 187/2) focuses on the Sunda Shelf off the Mekong river, a few sections were taken in the VUA. The distribution of temperature in section 4 (fig. 6.15a) shows, that also during this cruise, the isotherms tilts slightly upward towards the coast. Nearest to the coast, at the bottom, the isotherms incline downward, like it was found during VG3. In section 6 a mesoscale anticyclonic eddy can be assumed, like it was demonstrated at this location in state 4 of the horizontal circulations. On the Sunda Shelf itself (T8) a slight upward tilting of the isotherms was observed (fig. 6.15c). The distribution of the salinity demonstrates a northward movement of Mekong influenced water (CSWS).

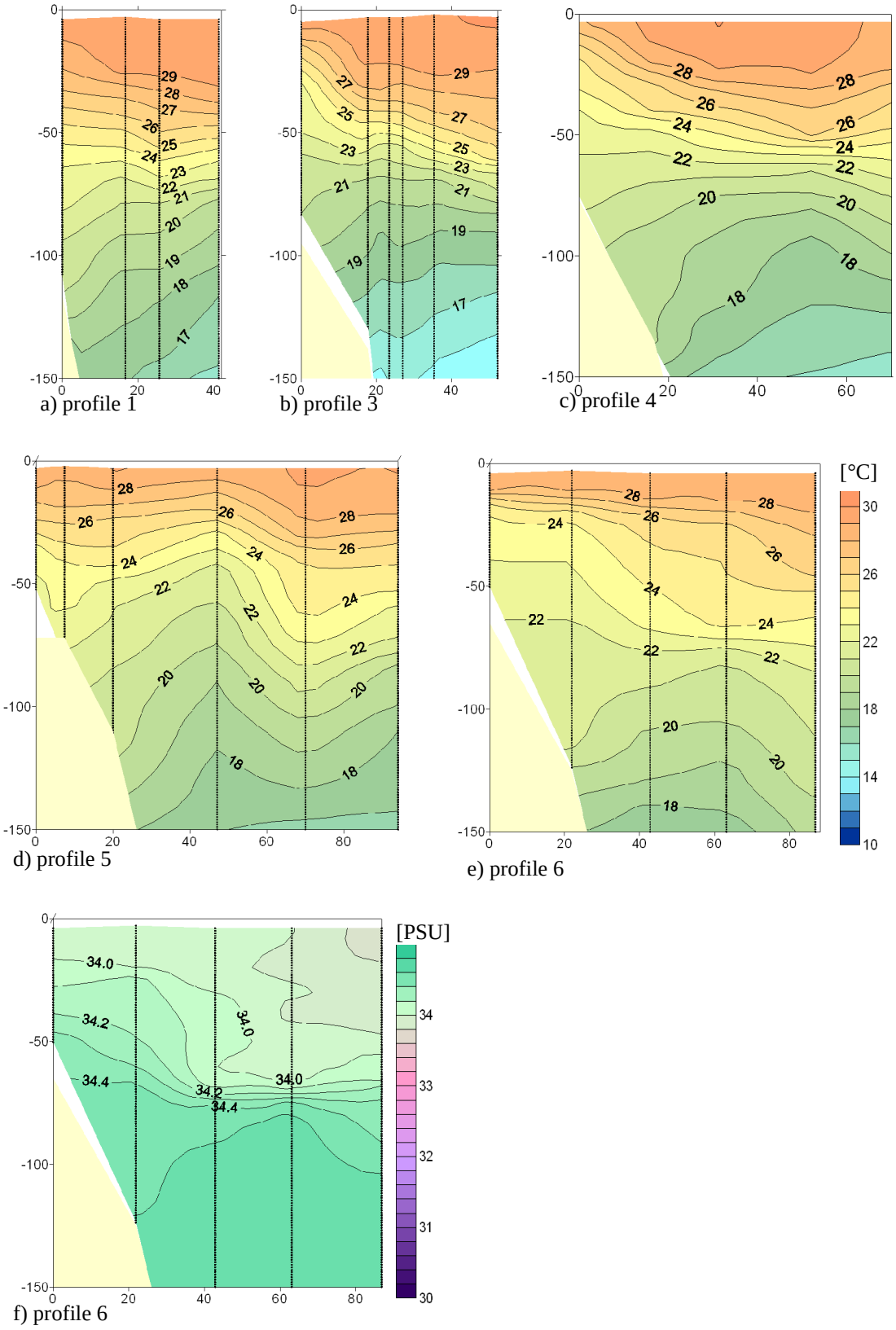

Fig. 6.13:Vertical profiles of temperature (a, b, c, d, e) and salinity (f) at VG4

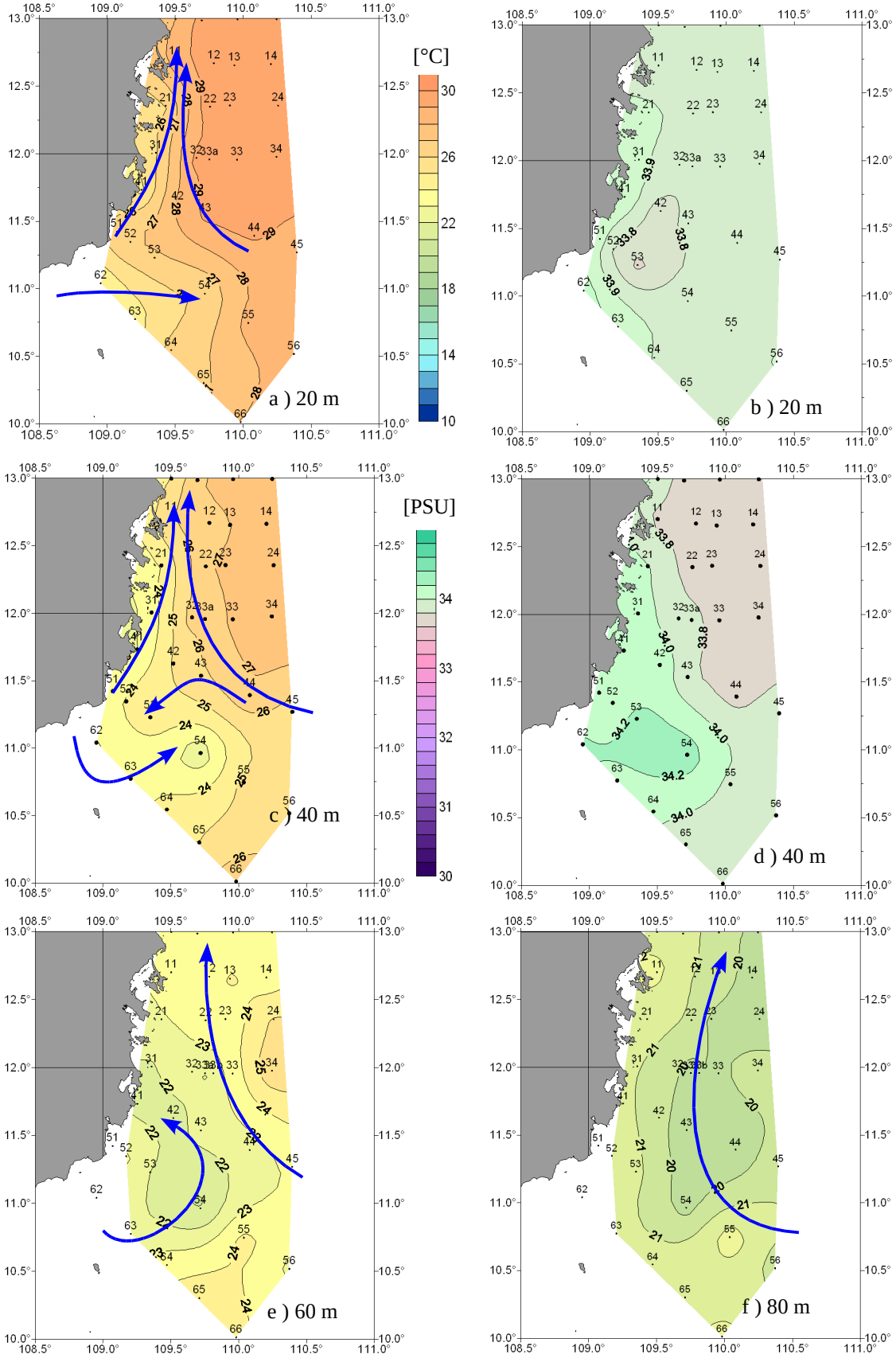

Fig. 6.14: Horizontal distribution of temperatures (a, c, e, f) and salinity (b,d) at VG4

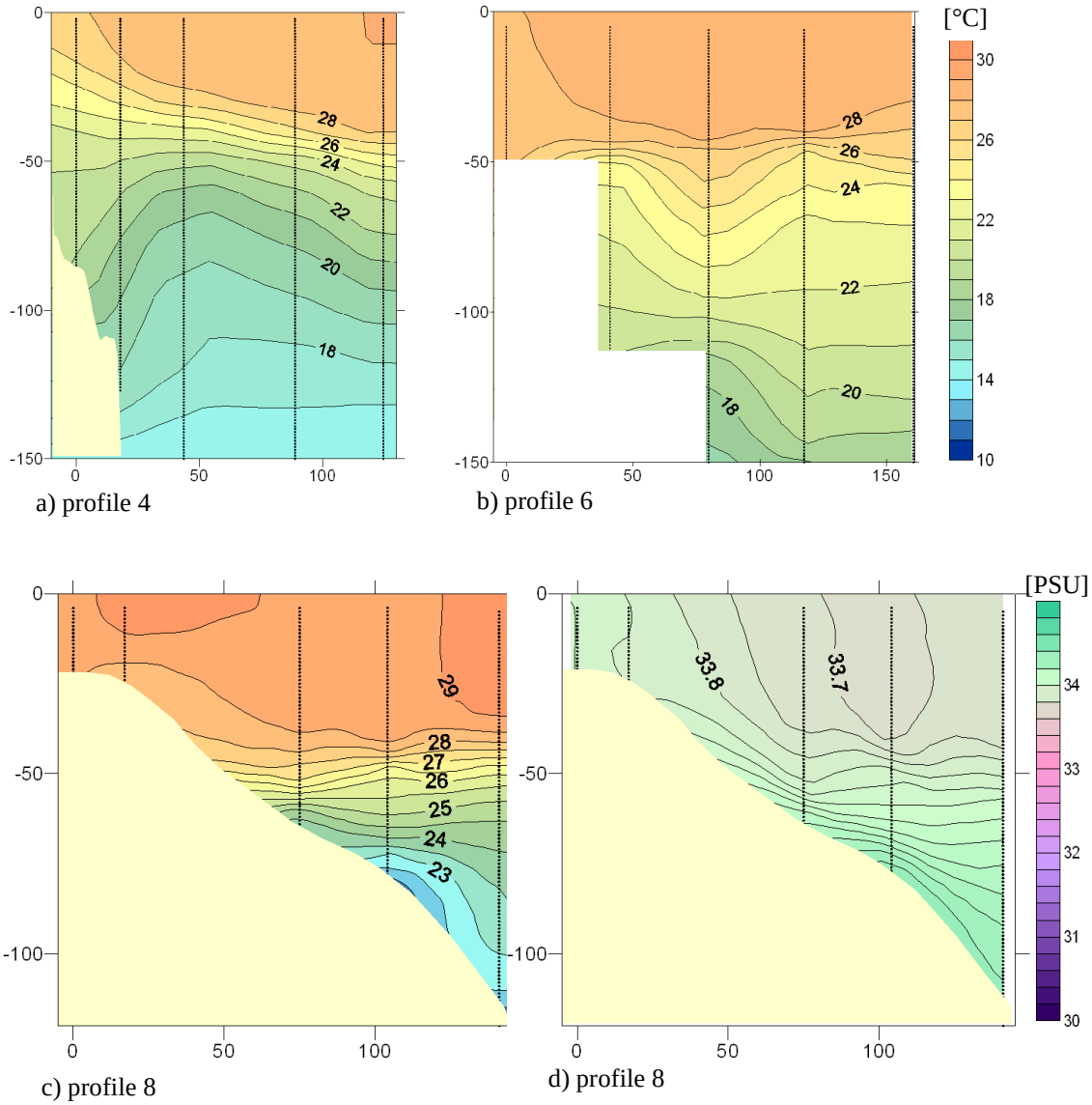

a) profile 4

b) profile 6

c) profile 8

d) profile 8

Fig. 6.15:Vertical sections of temperature (a, b, c) and salinity (e) at SO187-2

6.5 The winter cruise

The winter cruise started directly after a cold surge, i.e. An outbreak of the winter monsoon, hence directly after the establishment according to state 1 of the horizontal circulation. The model reproduce strong positive vertical velocities in this state at pronounced locations. During the cold surge, vertical velocities with the magnitude O(9 m day^{-1}) are simulated in the area of Cam Ranh (fig. 6.16. During the cruise, the monsoon shuts down and the circulation was switched rapidly into state 2. This complicates the interpretation of the observations in this manner, because by this means UW is advected horizontally away from its origin. At the beginning of the cruise off Cam Ranh and even off Nha Trang vertical velocities of O(3 m day^{-1}) are reproduced.

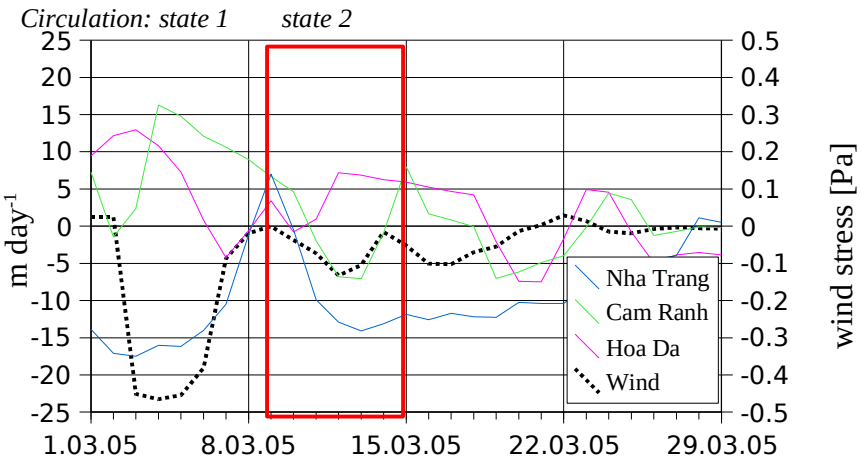

Fig. 6.16: Reproduction of the vertical velocities [m day^{-1}] with E0 and the alongshore wind stress (red line) during VG8

The distribution of the temperature in the sections perpendicular to the coast illustrate nicely the simulated downwelling at the shelf edge (fig. 6.17). A dome of cold water on the mid-shelf was observed in section 4 and section 5. Strong mixing throughout the whole water column was found. The distribution of salinity of section 5 shows offshore lower salinity (OSWS).

As in last the sections, the horizontal distribution of the temperature in combination with the horizontal circulation from the simulation is most suitably for the interpretation of the observed hydrography. Fig 6.18a shows the temperatures at 20m water depth, superimposed with the currents by the simulation (blue arrows). The pool of cold water is well illustrated. Interestingly, it was not observed in the area, where E0 reproduces upwelling. However, using the horizontal circulation the distribution can be explained. Following the simulation results, the water was uplifted before the cruise at the ridge south of Cam Ranh (near station

41 and station 42). The blue arrows show, that after the upwelling, the horizontal circulation transports the UW into the regions where it was observed. With horizontal velocities of O(0.5 m day^{-1}) and approximately a time leg of 2 to 3 days after the upwelling event, a transport of approximately 0.5° can be achieved. Noteworthy, the UW was found 0.5° from its formation. The distribution of salinity (fig. 6.18) reflects well the circulation pattern simulated by the model. The low salinity pool (<34 PSU) observed on station 32, was transported from the north and belongs to CSWN. The offshore displacement of the southward boundary current, which is influenced by the salinity rich water originating from the western pacific, can be found in the northern offshore region. The distribution of temperature at 50 m depth illustrates a 1°C colder area in the north compared to the south. The distribution of the salinity (fig. 6.18d) shows a low salinity pool (< 34.1) on station 42.
At 150 m depth(fig. 6.18e) temperature field shows a well defined west-east gradient, which can be explained by downwelling at the shelf-edge.
Fig. 6.18e shows the wind field and the distribution of the cold dome (<23°C) at 20 m water depth. This figure illustrates, that surface cooling due to evaporation and mixing can not explain the temperature field, since the strongest wind stress is located more to the south-east. An horizontal advection between this regions is not realistic, as demonstrated by the model.

Nor the results from the model, neither the distribution of vertical velocities reproduced by the model can answer the question of the effectiveness of the upwelling process on primary production. For this reason the next section illustrates the distribution of the fluorescence by in-situ observations.

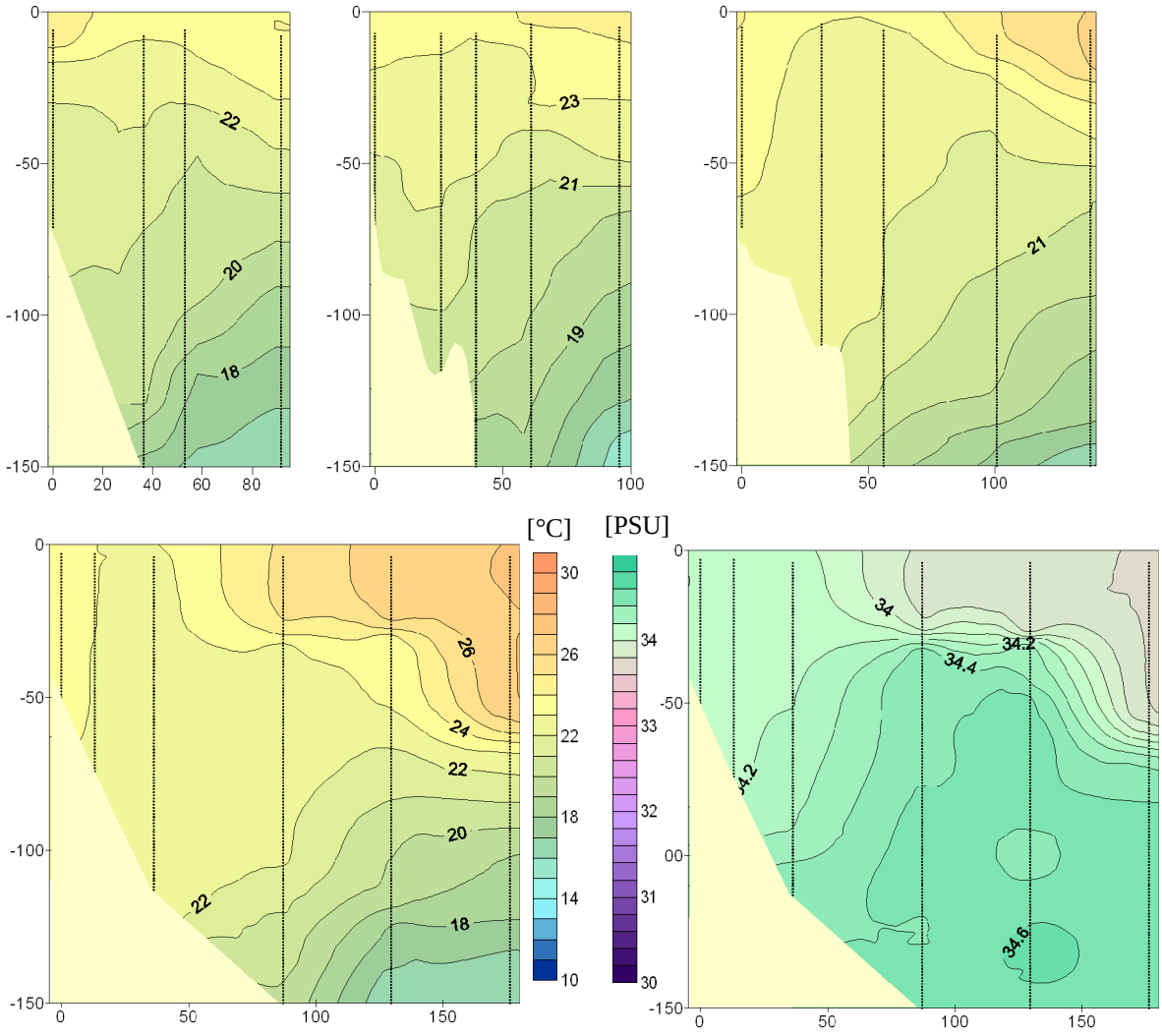

Fig. 6.17:Vertical sections of temperature (a, b, c) and salinity (b) at VG8

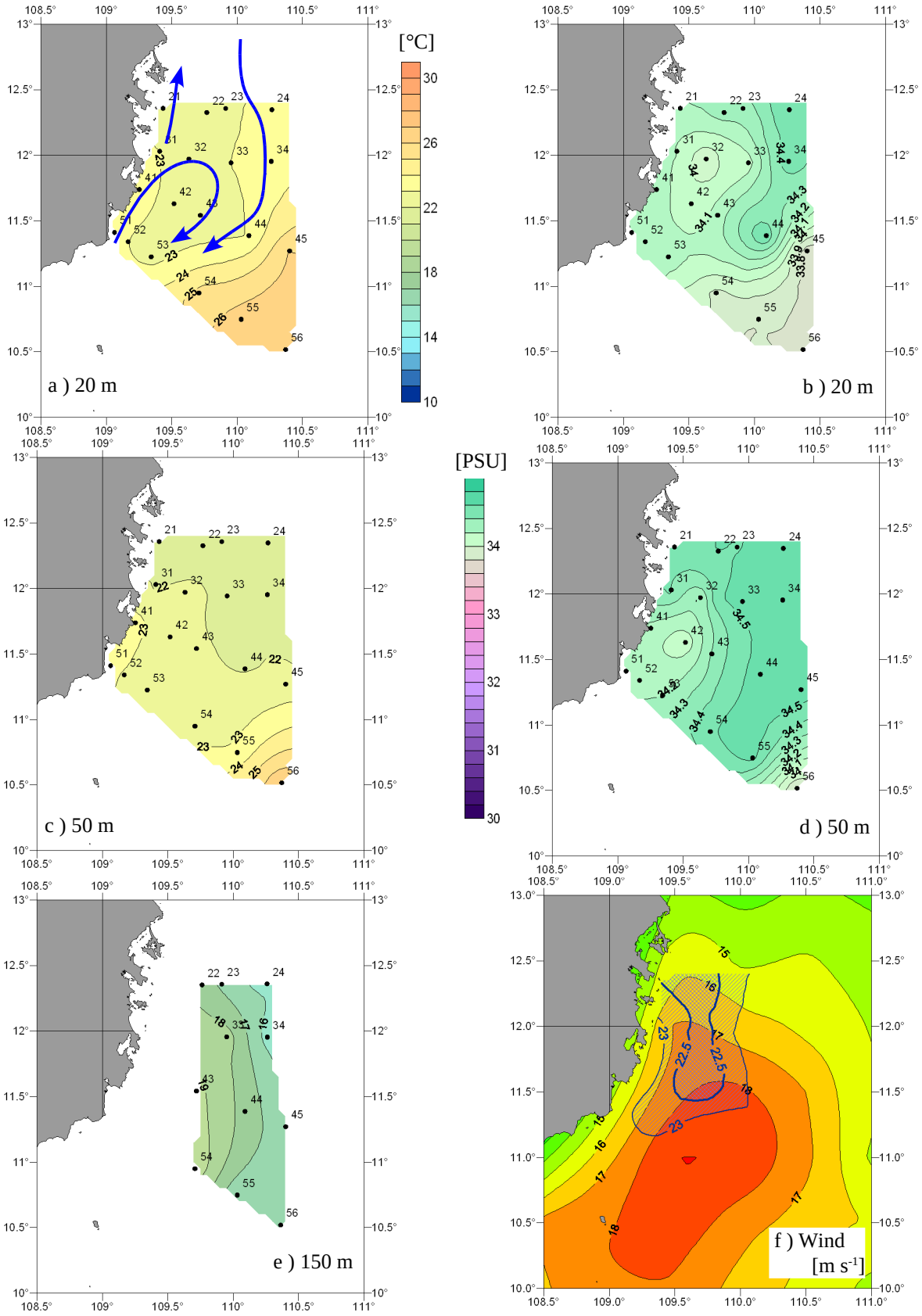

Fig. 6.18: Horizontal distribution of temperatures (a, c, e), salinity (b, e) at VG8 and the relation of the wind field during the cold surge and the UW (f)

6.6 Nutrient concentrations and fluorescence observations

This thesis has its focus on the physical processes in the upwelling area off Vietnam. However, mentioning the words in the introduction, the physical processes related to upwelling are one of the most important nutrient sources for primary production. Hence, a physical-biological coupling, as it is suggested by Ning et a. (2004) in the SCS, is of interest. In this thesis, the biological processes itself will not be discussed, but the distribution of chlorophyll *a*, in relation to the results from the simulation and the hydrographic observations, is shown. Primary production usually bases on the availability of nutrients. The nutrient concentrations during the cruise VG3 was subject of the publication of Dippner et al. (2006). The surface water was nearby nutrient depleted. In 50 m water depth Dippner illustrated a strong nitrate concentration in on the stations where UW was observed, with a magnitude more than 6 mmol l^{-1} on the station 41 and station 42 (11° 35' N). This is the location where the vertical velocities of the simulation shows maximum upwelling. The spreading of the nitrate over the shelf is in good agreement with the spatial distribution of the reproduced upwelling.

The nutrient distribution, integrated over the first 40 m, presented in the work report of the Leibniz-Institut für Ostseeforschung Warnemünde (2005) also illustrates the similarity to the hydrographic distribution. During VG3 the near-shore band of increased nitrate reflects well the band of lower temperatures. As well as the stronger temperature drop during VG7, the nutrient concentrations are noticeable higher than those during VG3. The offshore advected UW at station 54 during VG4 shows concentrations of Nitrate comparable with the concentrations in the UW during VG7. During VG8 increased concentrations of nutrients on the stations associated with UW in the last section could be found.

During the cruises also in-situ fluorescence data with a Seapoint fluorometer was collected. The observed fluorescence was validated with chlorophyll *a* measurements, which can be expected as a good approximation. For the determination of chlorophyll *a* one to three litre of water was filtered and frozen. In the laboratory the magnitude of the Chlorophyll *a* in the water were calculated after Jeffrey and Humphrey (1975) with a spectrophotometer.

Lui et al. (2002) found that the chlorophyll maximum in the subsurface in the SCS is a good approximation for primary production. In the region of the Bengalua upwelling system, Brown and Field (1986) observed the highest chlorophyll concentrations not in the newly uplifted water, but in water masses which are comprise of horizontally advected or aged upwelled water. They calculated a good correlation between the chlorophyll concentration and the primary production. Figueiras et al. (2002) calculated an increase of the concentration of chlorophyll *a* of 0.69 mg m^{-3} day^{-1}. Mentioning the strong horizontal

currents in the VUA, the strongest magnitude of the fluorescence can not be found in the regions of the upwelling itself, but in the downstream direction. Fig. 6.19 shows the distribution of fluorescence along section T2 of the cruises VG3, VG7 and VG8. This section is approximately in the downstream direction of the strongest upwelling. A similarity can be found in all three sections, with the highest magnitude of fluorescence during VG7. During VG3 the maximum fluorescence was not observed direct at the coast. Thus, the offshore advection of the upwelling influenced water during VG3 is also noticeable in the distribution of the fluorescence. Moreover, the figure shows that even during winter the upwelling influences the primary production (fig. 6.19 c). Due to the hydrographic distribution during VG4, UW can be found in section 6. Fig. 6.20 illustrates this section during the inter-monsoon (VG 4) and the summer monsoon (VG 7). During both cruises, the response of the primary production induced by upwelling is observable. The magnitude of the concentration is lower during the inter-monsoon, as it can deduced from the weaker vertical velocities during this period.

Summarizing this section, it is shown, that the upwelling influences the primary production as well during summer, as during winter and spring.

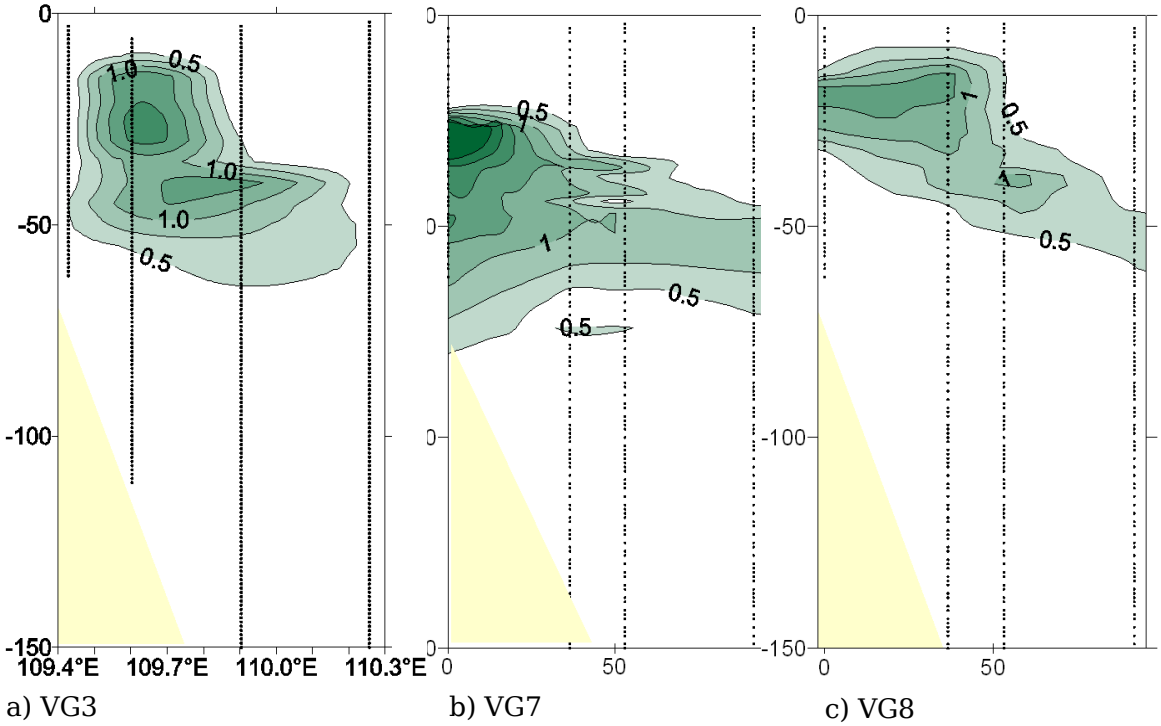

Fig. 6.19: Vertical concentration of fluorescence in section 2 at VG3 (a), VG7 (b) and VG8 (c). Units: mg m^{-3}

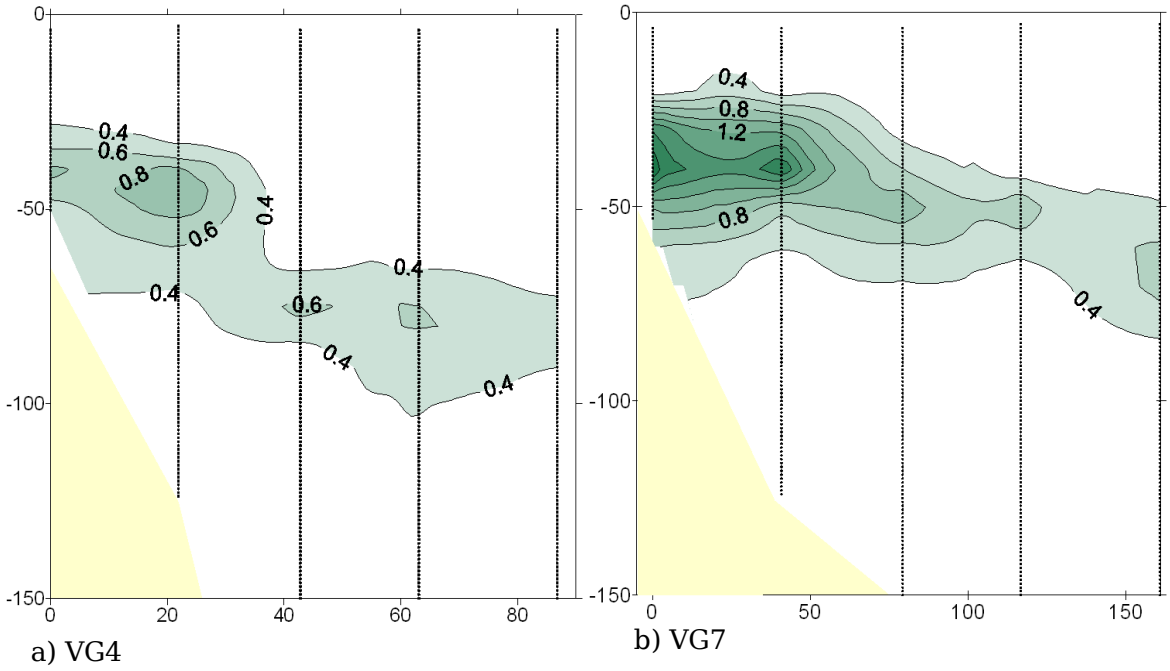

Fig. 6.20: Vertical concentration of fluorescence in section 6 at VG4 (a) and VG7 (b). Units: mg m^{-3}

7

Coastal Upwelling Processes in two dimensions

The distribution of the horizontal and vertical currents presented in Chapter 5 and the analysis of the measurements in Chapter 6 illustrate the appearance of the upwelling. The processes behind the temporal and spatial distribution of the vertical velocities is discussed in this and the next chapter.

Generally, upwelling processes can divided in two dimensional processes and three dimensional processes. The difference is that the two dimensional processes assume the bathymetry, wind-stress and the currents to be homogeneous in the alongshore direction. However, the two dimensional processes are not truly two dimensional, alongshore currents and pressure gradients are allowed. The two dimensional processes are wind driven upwelling and current driven upwelling, both will be deduced here. The magnitude of the processes, compared to each other and to the results of the model (E0), will be analyzed.

7.1 Wind-driven upwelling

The classical coastal upwelling is forced by local alongshore wind, resulting in a net transport of the surface water to the right (northern hemisphere) of the wind direction. This has to be compensated by onshore transport of water in the interior, a process which is well known and examined by many models. According to Ekman (1905), assuming steady state conditions, a homogeneous ocean and steadily blowing wind, the equations of motions can be simplified in a way that only the effect of vertical turbulence is considered in the frictional terms. For the calculation of wind-driven upwelling, first, the wind-induced drift current is calculated, which is produced by the drag of the wind over homogeneous water.

For the calculation it is necessary to neglect the horizontal pressure gradient, which leads to the assumption, that only the wind drag and the coupling with vertical friction are essential processes. According to Ekmans solution it is necessary, that the water is unbounded in the horizontal and the sea is of infinite depth.
With the assumptions made before, the equations of motions can be simplified to:

$$u \cdot f = \frac{A_v}{\rho} \cdot \frac{\delta^2 v}{\delta z^2} \tag{7.1a}$$

$$-v \cdot f = \frac{A_v}{\rho} \cdot \frac{\delta^2 u}{\delta z^2} \tag{7.1b}$$

where ρ is defined as the pressure, and f is the Coriolis parameter:

$f = \Omega \cdot \sin(\varphi)$

with $\Omega = 7.292 \cdot 10^{-5} s^{-1}$ being the rotation rate of the earth.

A_v is defined as the vertical coefficient of turbulent viscosity and is assumed to be constant at first.
The variable *a* is established:

$$a^2 = \frac{f \cdot \rho}{A_v} \tag{7.2}$$

The equation (7.1a) and (7.1b) can be multiplied with $i = \sqrt{-1}$, which yields:

$$u \cdot i \cdot a^2 = i \cdot \frac{\delta^2 v}{\delta z^2} \tag{7.4b}$$

$$v \cdot i^2 \cdot a^2 = \frac{\delta^2 u}{\delta z^2} \tag{7.3b}$$

Summarising of the equation (7.3a) and (7.3b) gives:

$$(u + i \cdot v) \cdot i \cdot a^2 = \frac{\delta^2 (u + i \cdot v)}{\delta z^2} \tag{7.4}$$

The solution of (4) is:

$$u + i \cdot v = C_1 \cdot e^{i \cdot C_3} \cdot e^{a \cdot \sqrt{i} \cdot z} + C_2 \cdot e^{-i \cdot C_4} \cdot e^{-a \cdot \sqrt{i} \cdot z} \tag{7.5}$$

It is possible to calculate the velocity components through separation of the real and the imaginary part:

$$u = C_1 \cdot e^{\frac{a}{\sqrt{2}} \cdot z} \cdot \cos\left(\frac{a}{\sqrt{2}} \cdot z + C_3\right) + C_2 \cdot e^{-(a \cdot \sqrt{2}) \cdot z} \cdot \cos\left(\frac{a}{\sqrt{2}} \cdot z + C_4\right) \tag{7.6a}$$

$$v = C_1 \cdot e^{\frac{a}{\sqrt{2}} \cdot z} \cdot \sin\left(\frac{a}{\sqrt{2}} \cdot z + C_3\right) + C_2 \cdot e^{-(a \cdot \sqrt{2}) \cdot z} \cdot \sin\left(\frac{a}{\sqrt{2}} \cdot z + C_4\right) \qquad (7.6b)$$

The solution depends mainly on the four constants C_1, C_2, C_3, C_4 . These constants can be terminated with the boundary conditions.

As said at the beginning, the depth of the water is infinite $(z = \infty)$. Equation (7.6) shows that, if C1 is zero, it is possible to accomplish the boundary condition v = u = 0 at $z = \infty$. It follows, that the first term on the right hand side of (7.6 a;b) can be disposed from the formula.

At the sea surface, the boundary condition is given by the wind stress τ_x, τ_y .

For simplification, the coordinate system will be rotated in a way that the wind is blowing only in the y-direction.

Then τ_x will be zero at the surface:

$$\tau_x = 0 \quad at\, z = 0 \qquad (7.7a)$$

τ_y must be the negative vertical coefficient of turbulent viscosity multiplied by δv and divided by δz , hence the frictional influence at the surface is:

$$\tau_y = -A_v \cdot \frac{\delta v}{\delta z} \quad at\, z = 0 \qquad (7.7b)$$

The boundary condition equation (7.7a) yields the equation:

$$\left(\frac{\delta u}{\delta z}\right)_{z=0} = \frac{-C_2 \cdot a}{\sqrt{2}} \cdot (\sin(C_4) + \cos(C_4)) = 0 \qquad (7.8)$$

Equation 7.8 is true if $(\sin(C_4) + \cos(C_4)) = 0$. This is the case if $C_4 = 45°$.

The boundary condition equation (7.7a) yields the equation:

$$\left(\frac{\delta v}{\delta z}\right)_{z=0} = \frac{C_2 \cdot a}{\sqrt{2}} \cdot (\cos(45°) + \sin(45°)) = \frac{-\tau_y}{A_v}$$

Because $(\sin(45°) + \cos(45°)) = \sqrt{2}$, the second constant, C_2, can be found: $C_2 = \frac{\tau_y}{A_v \cdot a}$.

Equation (7.7) illustrates, that C_2 is the velocity of the current at the surface and will be called V_0 in the following.

Ekman (1905) introduced the depth of frictional influence, the depth of the “Ekman-Layer” (D_e) :

$$D_e = \pi \cdot \sqrt{\frac{A_v}{\rho \cdot \frac{1}{2} \cdot f}} \tag{7.9}$$

After inserting D_e into (6a;b) and with the boundary conditions calculated before, the drift current as a function of depth is:

$$u = V_0 \cdot e^{-(\frac{\pi}{D_e}) \cdot z} \cdot \cos(45° - \frac{\pi}{D_e} \cdot z) \tag{7.10a}$$

$$v = V_0 \cdot e^{-(\frac{\pi}{D_e}) \cdot z} \cdot \sin(45° - \frac{\pi}{D_e} \cdot z) \tag{7.10b}$$

If $z = D_e$ in the equations (10a) and (10b), u and v near zero.

From the drift currents in equation (7.10a) and equation (7.10b), with several idealisations, vertical velocities can be approximated. At first, a sea with two layers (fig. 7.1), a layer of frictional influence at the surface and a geostrophic interior, is defined. The coordinate system is rotated in such manner that the y-Axis points in alongshore-direction, with the coast to the left, the x-Axis is zero at the coast and points offshore.

The water depth d has to be large enough for the frictional influence on the Bottom-Boundary-Layer (BBL) to be negligible, yielding a minimum water depth of about three times D_E. Although it contradicts the boundary conditions of the drift current, a vertical wall exist at x = 0. The horizontal scale is set to be sufficiently small for the effect of a varying Coriolis-parameter with latitude $(\beta - effect)$ to be negligible (f-plane).

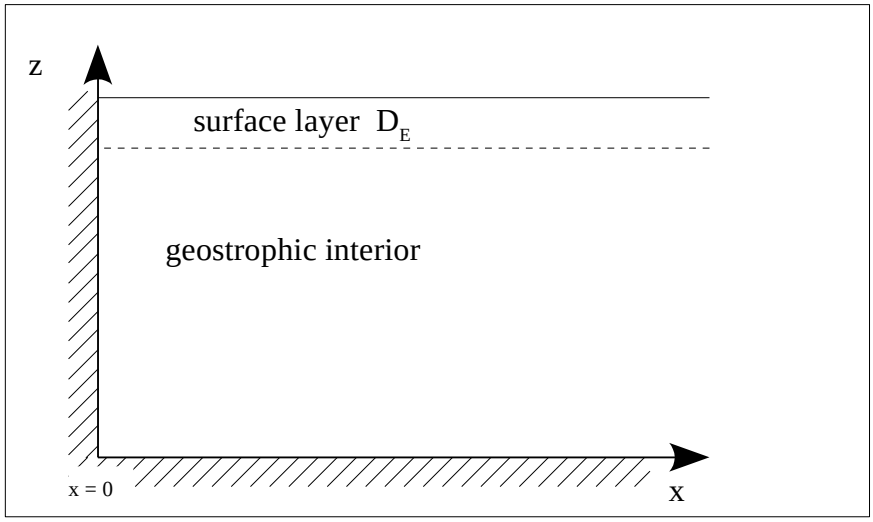

Fig. 7.1 Scheme of a simple two layered sea

If a homogeneous wind field is assumed, and with that a homogeneous flow in the alongshore direction, the equation of continuity or conservation of mass (7.11a) can be used for a two-dimensional environment (7.11b):

$$\frac{\delta v}{\delta y}+\frac{\delta u}{\delta x}+\frac{\delta w}{\delta z}=0 \qquad (7.11a)$$

$$\frac{\delta u}{\delta x}+\frac{\delta w}{\delta z}=0 \qquad (7.11b)$$

Of course, no water can flow through the bottom, and the vertical movement of the sea surface is assumed to be negligibly small. With these conditions at the surface and at the bottom, the vertical velocity has to be zero:

$$w=0 \quad at\, z=0 \wedge z=d \qquad (7.12)$$

With equation (7.10) and $u_e \approx 0 \quad at\, D_e$ the mass transport in the surface layer can be calculated:

$$m_{xe} \approx \rho \cdot \int_0^{D_e} u \cdot dz = \rho \cdot \frac{V_0 \cdot D_e}{\pi \cdot \sqrt{2}}$$

Insertion of V_0 and D_e results in a simple approximation of the wind induced mass transport:

$$m_{xe}=\rho \cdot \frac{\tau_y}{f} \qquad (7.13)$$

Mentioning the conservation of mass (7.11b) and the boundary conditions (7.12), the integrated transports in the cross-shore direction have to be zero:

$$\int_0^d u \cdot \delta z = 0 \qquad (7.14)$$

This yields the conclusion, that the transport m_{xe} in the surface layer has to be compensated by the geostrophic interior:

$$m_{xe} = -m_{xg} \qquad (7.15)$$

This is true if the BBL is neglected, and d is of such depth that the geostrophic interior is sufficiently far away from all frictional influences.

The velocity of the onshore current in the geostrophic interior can be approximated, with D_g as the depth of the geostophic interior:

$$u_g \approx \frac{M_{xe}}{D_g} \quad \text{or} \quad u_g \approx \frac{\rho \cdot \frac{\tau}{f}}{D_g} \qquad (7.16)$$

With the insertion of $\delta z = D_g$ and $\delta x = L_x$ in equation (7.11b), the vertical velocity (w_{wind}) can be estimated:

$$w_{wind} = u_g \cdot \frac{D_g}{L_x} \qquad (7.17a)$$

The magnitude of the geostrophic current is known from equation (7.16) and with that, an estimated equation for vertical velocities is established:

$$w_{wind} = \frac{\tau_y}{\rho \cdot f \cdot L_x} \qquad (7.17b)$$

In this equation L_x is a representative horizontal length scale.

Hidaka (1954) as well, investigated in a steady-state upwelling theory in a homogeneous ocean. According to his theory, an approximate value for the vertical motion can be found, if the horizontal geostrophic velocity u_g is known:

$$\frac{w_{wind}}{u_g} = \frac{D_e}{L_x} = \sqrt{\frac{A_v}{A_h}}$$

With the assumption, that the surface layer has the same thickness as the geostrophic interior $D_e \approx D_g$, this equation is the same as (7.17a). Hence, the vertical velocities depend on the ratio of the vertical and horizontal viscosity multiplied by the geostrophic onshore current.

In analogy to D_e , Hidaka defines a “horizontal frictional distance”:

$$L_x = \sqrt{\frac{A_h}{f}}$$

In this equation, A_h is the horizontal eddy coefficient of turbulent viscosity.
For wind in the alongshore direction, Hidaka calculated upwelling between the coast and a distance of 0.5 L_x .
Garvin (1971) used the same estimation of L_x. Allen (1971) and Pedlowsky (1974) included stratification in their upwelling model. Both used a slightly different calculation of L_x:

$$L_x = \sqrt{\frac{A_h}{A_v}} \cdot d \qquad (7.18)$$

Hamilton and Rattray (1978) established the baroclinic radius of deformation as horizontal length scale:

$$L_x = R = \frac{N \cdot d}{f} \qquad (7.19)$$

In this thesis, the same horizontal scale as in the solution established by Allen (1971) and Pedlowsky(1974) is used. In Chapter 3 the estimation of A_v in HAMSOM was illustrated. The model provides a good estimation of the vertical turbulent viscosity coefficient, which depends on the vertical sheer and the stratification of the water column.
The equation of wind driven upwelling is based on an offshore flow of the surface layer. This yields a pressure gradient in the offshore direction. Of course, currents flow perpendicular to the pressure gradient, hence this solution requires an alongshore pressure component $\delta\eta/\delta y$, where η is the elevation of the sea surface. A solution including alongshore currents, and with those an alongshore pressure gradient, was calculated by Garvine (1971). Due to the pressure gradient $\delta\eta/\delta x$ induced by the drift current, an alongshore current establishes, which induces an alongshore pressure gradient if the coast is not endless. This is a necessary condition to induce a geostrophic onshore flow in the interior.
The estimation of the vertical velocities of the wind driven upwelling is an idealized view on coastal upwelling, primarily because of the assumption of $d \gg D_e$ to neglect the effect of friction. In smaller depth the BBL has to be included, as Ekman (1923) did by calculating slope currents. Ekman illustrated that the typical spiral is deformed and alongshore currents are established. A coastal jet in the direction of the alongshore wind was deducted by Yoshida (1955), Thomson and O'Brian (1973) and Pedlowski (1978). Three-layer models of transient upwelling illustrate, that the wind displaces the surface layer, thus transporting the next layer to the surface, the third layer is only moved upward slightly (Csanady, 1981). Leth and Middleton (2004b) included the BBL in their hydrodynamic upwelling model and

analyzed the spin up phase of the upwelling process. Their results indicate that only in the first few days the offshore transport in the Ekman layer due to the wind stress is directly balanced by an onshore flow in the interior. After the increase in strength of the alongshore currents, a balance between wind stress and bottom friction is reached, and with that, the upwelling is restricted to the BBL. The process behind upwelling through the BBL can be called current driven upwelling is illustrated in the next section.

7.2 Current driven upwelling

If the coast lies to the left (northern hemisphere) of the current direction, friction- induced motions enable vertical velocities. The bottom friction on the shelf and the Coriolis acceleration cause an onshore flow near the bottom (Hsueh and O'Brien, 1972). The currents can be induced by local wind, or be part of the basin-wide circulation. Due to the westward intensification of ocean currents, upwelling at western boundaries is more strongly influenced by the currents of the basin-wide circulation than at eastern boundaries.
To induce upwelling through the BBL, a geostrophic current, which induces an alongshore velocity (*v*), is needed. The calculations will be done in the same coordinate system as in the case of wind driven upwelling, a flat bottom and a vertical wall to the right are assumed. Instead of a surface boundary layer a BBL is introduced.
With the thickness of the BBL and the alongshore velocity v at the top of it, the cross-shore velocity u_B in the BBL can be calculated:

$$u_B = -v \cdot \exp\left(\frac{-\pi \cdot (d-z)}{D_B}\right) \cdot \sin\left(\frac{\pi \cdot (d-z)}{D_B}\right) \tag{7.20}$$

With equation (7.20) a transport of mass in the across-shore direction of the BBL is ascertainable:

$$m_{xB} = \int_{d}^{(d-D_B)} u_B \cdot dz = -\frac{1}{2} \cdot v \cdot D_B \tag{7.21}$$

The thickness D_B of the BBL can be calculated with:

$$D_B = \sqrt{\frac{2 \cdot \left(\frac{A_v}{\rho}\right)}{f}} \tag{7.22}$$

As well as in the case of the wind driven upwelling, the vertical velocity of current driven upwelling (w_{cur}) across a length scale (L_x) can be approximated due to conservation of

transports (7.11b) and the transport of mass in the across-shore direction of the BBL (7.21):

$$w_{cur} = \frac{\frac{1}{2} \cdot v \cdot D_B}{L_x} \tag{7.23}$$

where *v* is the along-shore velocity at the top of the BBL. As well as the wind driven upwelling (7.17b), the vertical velocities can be calculated independent of the depth of the boundary layer.
A helpful relationship was established by Gill (1982):

$$\sqrt{\frac{1}{2} \cdot \left(\frac{A_v}{\rho} \right) \cdot f} = 2 \cdot C_D \cdot |v| \tag{7.24}$$

where C_D is a drag coefficient and *v* is a velocity in the alongshore direction at the top of the BBL.
Equation (7.24) can be converted to (A_v / ρ) ,in order that equation (7.24) can be integrated into equation (7.22). Applying the equation (7.22) to equation (7.23) yields an idealized equation for current-driven upwelling:

$$w_{cur} = \frac{2 \cdot C_D \cdot |v| \cdot v}{f \cdot L_x} \tag{7.25}$$

A typical magnitude of the drag coefficient is: $C_D = 2 \cdot 10^{-3}$.

Equation (7.25) illustrates well that positive alongshore currents on the shelf induce positive vertical velocities, if the coast lies left of the current. Thus, upwelling can appear independent from the local wind forcing.

7.3 The magnitude of two dimensional upwelling

The two main two-dimensional mechanism that drive the coastal upwelling have been deduced in the last two sections. In this section, the magnitude of both processes will be compared to each other. Also, the behavior of the spin-up of an upwelling event will be investigated. The two-dimensional processes are set in relation to the resulting vertical velocities from E0. The indication of a bathymetric steering, which was suggested by the distribution of the vertical velocities in chapter 5, will first be neglected and discussed in the next section.

To compare the wind-driven and the current-driven processes, the ratio of wind-driven

vertical velocities and current-driven vertical velocities can be calculated:

$$\frac{w_{cur}}{w_{wind}} = \frac{2 \cdot C_d \cdot |v| \cdot v / (f \cdot L_x)}{\tau_y / (\rho \cdot f \cdot L_x)} = \frac{2\,\rho \cdot Cd \cdot |v| \cdot v}{\tau_y} \tag{7.25}$$

Considering the deductions from section 7.1 and 7.2, both processes are based on the conservation of transports. Thus, one interpretation of the ratio w_{cur} / w_{wind} is, that if it is 1, the offshore surface drift current is completely balanced by the friction-induced onshore movement of the BBL and a cross-shelf transport in the geostrophic interior vanishes. Values of more that 1 indicate that the currents are not forced through the local wind alone and are influenced by the basin-wide circulation.

Generally speaking, if a boundary current of 0.5 m s^{-1} is present on the shelf, than the wind stress has to be greater than 1.03 PA for the ratio to be smaller than 1. With an average wind stress of 0.13 PA, which is realistic in the VUA during summer, the effect of the BBL will be stronger if the alongshore current is stronger than 0.23 ms^{-1}.

As mentioned by Leth and Middleton (2004b), the spin-up phase of upwelling is an important process. To illustrate the behavior of the vertical velocities induced by both two-dimensional processes, considering the local forcing, a small model experiment (E1) was implemented. For this, a barotropic model with realistic bathymetry and a constant wind field with the average values from Juli 2004 was used. The wind stress was set to southwest at a strength of 0.13 PA, which is a good approximation for the time investigated.

The realistic bathymetry leaves the assumption of two dimensions, but it reproduces well the situation which can be found in the VUA. The model was only run for one week to prevent any influences of the basin-wide circulation on the simulation. From the alongshore currents simulated by E1 and the wind stress, the ratio w_{cur} / w_{wind} for each day of the simulated period could be calculated.

The results of this experiment show some peculiarities. The ratio w_{cur} / w_{wind} is highest on the northern part of the VUA, between 12° N and 13° N. The ratio is around 1 after three days. This agrees well with the findings of Leth and Middleton (2004b). However, after five days, current-driven vertical velocities are two times higher than those induced by the surface offshore flow. On the shallow Sunda shelf in the south, the ratio is 1 after the first day and does not change anymore. In this region, after the first day of the simulation the currents at the surface are entirely in an alongshore direction, identical to the direction of the wind stress. An explanation for this may be that the Ekman surface layer completely overlaps the BBL and thus a drift transport perpendicular to the wind stress vanishes, as it was calculated by Ekman (1923). In the central region, where the alongshore gradient of the bathymetry is strongest, the ratio never reaches a value of 1. In this area the magnitude never exceeds a value of 0.8 during the spin-up process. In areas with a constant bathymetry, the ratio between alongshore currents (v_{along}) and ones perpendicular to the shore (v_{cross}) reaches

$v_{along}/v_{cross} > 100$ after six days. In areas with an varying bathymetry, the ratio is lower than 50 % of that, with ratios of $v_{along}/v_{cross} < 40$. This is comparable to the results of Song et al. (2001), who found meandering of currents over changing bathymetry.

The ratio w_{cur} / w_{wind} calculated with the currents of the long time run E0 includes the basin-wide circulation. For this, average alongshore currents for each of the four regions Nha Trang, Cam Ranh, Phan Rang and Hoa Da from E0 were calculated. These regions were defined in chapter 2.

With the alongshore wind stress for each region and the spatially averaged alongshore currents of E0, daily values of w_{wind} and w_{cur} were calculated and from these, daily and monthly vertical velocities. Using E0, for each of the four regions, depth-averaged monthly vertical velocities (w_{model}) were calculated as references. Fig. 7.2 illustrates the ratio w_{cur} / w_{wind}, fig. 7.3 the ratio w_{model} / w_{wind} and fig. 7.4 the ratio w_{model} / w_{cur}. Fig. 7.2a shows the vertical velocities calculated with equation (7.17b) (red line), equation (7.25) (blue line) and the ratio between current- and wind-driven upwelling in the region Nha Trang. The most apparent result is the change of the current direction in July and with that the change of the sign of the vertical velocities induced by the BBL. This results in a negative ratio w_{cur} / w_{wind} in this area from July to September. During this time, the currents flow in upwind direction, which is a result of the basin-wide pressure gradient and the wind stress curl. From October to February the ratio w_{cur} / w_{wind} is positive. The ratio is strongest in October with a value of more than five and decreases to a value of 1.5 in February. This is a surprising result, one might suggest that with the continuing northeast monsoon the cyclonic circulation would get stronger and the ratio increase. Probably, the pressure gradient, built up by the wind stress in the southwestern basin and the wind stress curl, prevents the strengthening of the boundary current during winter. From April to June the current-induced vertical velocities are growing slightly stronger than the wind-induced ones, but the ratio remains close to 1.

In the Cam Ranh region (fig. 7.2b) the distribution of the ratio w_{cur} / w_{wind} is very similar to that of the Nha Trang region. However, the current-induced vertical velocities decrease significantly in July, but they do not change their direction until September. This behavior of the currents was illustrated in the aforementioned 6th state of the horizontal currents. It was illustrated that the Cam Ranh region is the confluence zone of the two boundary currents. As in the northern region, a decrease of the ratio during winter is to be seen. The ratios are generally lower than those in the region of Nha Trang, which confirms the findings of experiment E1, hence the currents are directed further in an on- or offshore direction.

In the region of Phan Rang (fig. 7.2c), the ratio is comparable to that of the Cam Ranh region, except that the ratio is not negative during September.

In the southernmost region (fig. 7.2d), the Hoa Da area, the ratio between current-driven

upwelling and wind-driven upwelling is between 1.1 and 2.1 during the whole year, except in April, when the ratio is only 0.2. The currents are always in the direction of the wind, but the current-induced vertical velocities are, on average, 50% higher than those induced by the local wind. None of the regions shows a significant correlation between the two processes. Recapitulating Fig. 7.2, an interesting feature was discovered: in the north of the VUA, the current direction changes from cyclonic to anticyclonic before the monsoon changes its direction and also the change from anticyclonic to cyclonic is in late summer and not related to the change of the monsoon. The early change of the current direction in April was illustrated in the horizontal distribution of the currents of state 5 and can be explained with the impinging of an anticyclonic eddy on the shelf. The change of the current direction in the northern region during the southwest monsoon is due to the growing cyclonic circulation in the northern SCS and the associated strengthening of the counter current. Hence, the vertical velocities induced by the currents are negative in that area from July on. The southward boundary current may influence the anticyclonic circulation in the southern regions in such a way, that the northward current decreases with the continuing summer monsoon. Using sea surface temperatures from satellite, Kuo (2002) found a southward movement of the upwelling off the Vietnamese coast during summer. With the results from E0 this could be explained with the increase of the southward boundary current. The results of the modeling studies illustrate that this is not a smooth movement, but rather a jump between two states over only several days. These states were presented as state 5 and state 6 in chapter 5.

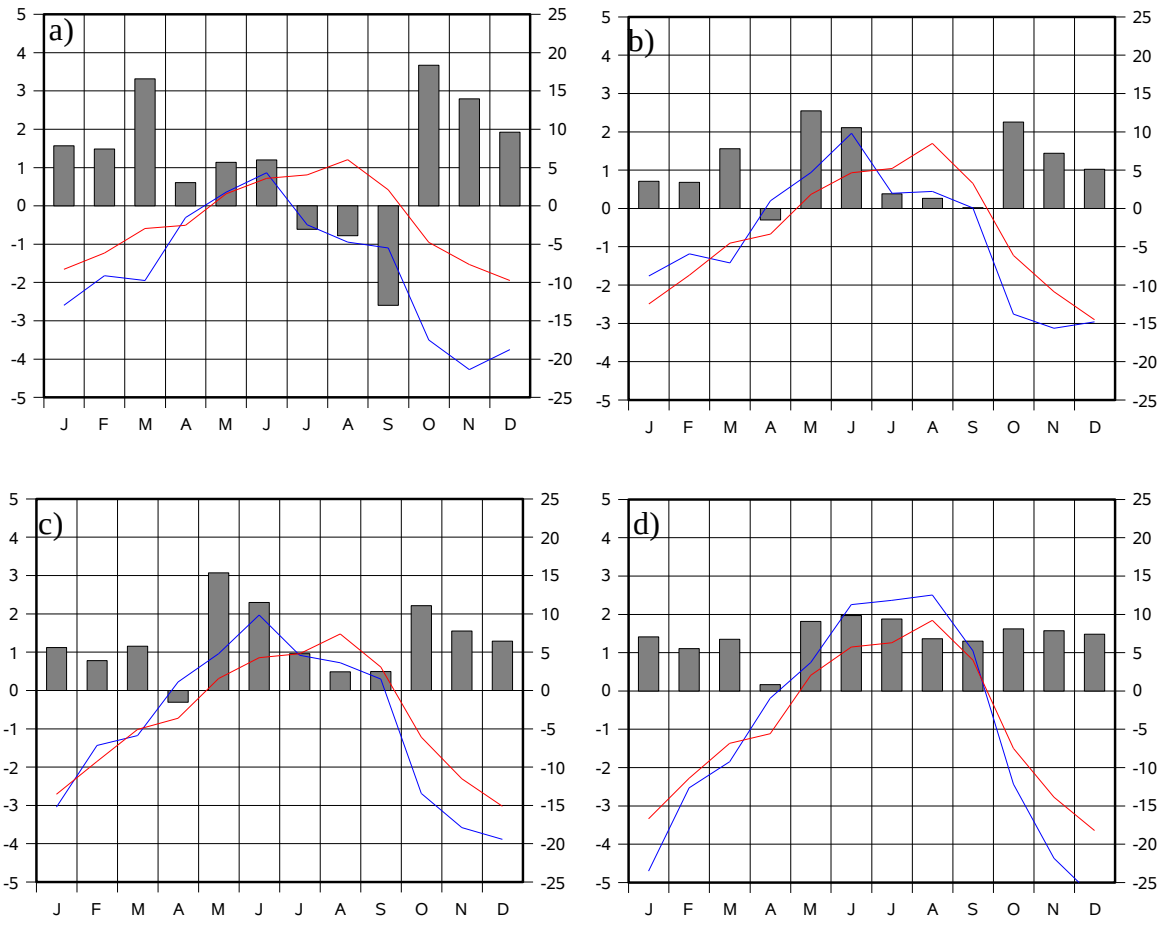

Fig. 7.2: Ratio of current- to wind-driven upwelling (w_{cur} / w_{wind}, gray bars), wind-driven vertical velocities (w_{wind}, red lines), current-driven vertical velocities (w_{cur}, blue lines) in the regions a) Nha Trang, b) Cam Ranh, c) Phan Rang and d) Hoa Da
Unit of the vertical velocities: m day^{-1}

Fig. 7.3 illustrates the ratio between the vertical velocities from the model results of E0 and those induced by wind-driven upwelling calculated with equation (7.17b). In the region of Nha Trang, the ratio is positive with a magnitude O(2) in winter. Due to the offshore anticyclonic eddy in April, the positive ratio turns negative. During summer, the vertical velocities of E0 are approximately constant, while the wind-induced vertical velocities increase with the strengthening of the monsoon and the ratio w_{model} / w_{wind} decreases from 4.3 in May to 2 in August.

This decrease can also be found in the Cam Ranh region (fig. 7.3b), but due to the higher winds in this region the ratio is slightly lower. From November to January, the model simulates positive vertical velocities, as it was found before in the distribution of the vertical velocities of state 1, thus the ratio is negative during this time.

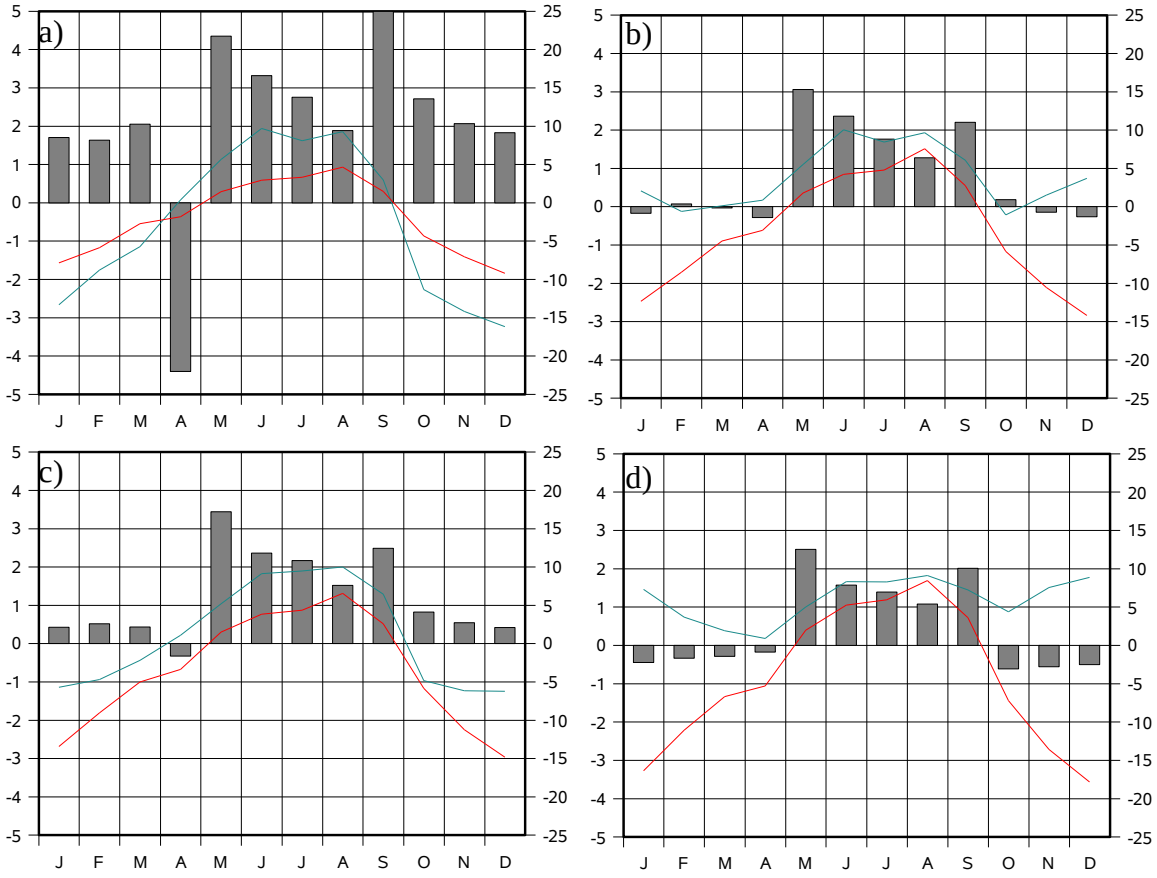

Fig. 7.3: Ratio of the upwelling from E0 to wind-driven upwelling (w_{model} / w_{wind}, gray bars), vertical velocities from E0 (w_{model}, green lines), wind-driven vertical velocities (w_{wind}, red lines) in the regions
a) Nha Trang, b) Cam Ranh, c) Phan Rang and d) Hoa Da
Unit of the vertical velocities: m day^{-1}

In the region of Phan Rang (fig. 7.3c) the decrease of the ratio w_{model} / w_{wind} during the summer monsoon is identical to that in the northern regions. During winter, the vertical velocities from E0 are half as strong as the the wind-induced ones.In the southernmost area, a decrease of the ratio w_{model} / w_{wind} during the summer monsoon can be found, as in regions to the north. During winter, the ratio is always negative, with values around -0.5. As it was illustrated in chapter 5, in this region, upwelling of the same strength is present in summer

and winter, even though the wind stress and the drift current presume downwelling.
The correlation between the wind-induced vertical velocities and the model results from E0, is 0.74, 0.31, 0.56, and -0.06 for the regions of Nha Trang, Cam Ranh, Phan Rang and Hoa Da respectively. The significant correlation in the region of Nha Trang yields the conclusion that on the deep shelf in the north, upwelling due to the local alongshore wind stress is an important process. But even in this region, during summer, the vertical velocities from the model are stronger than those calculated using equation (7.17b).

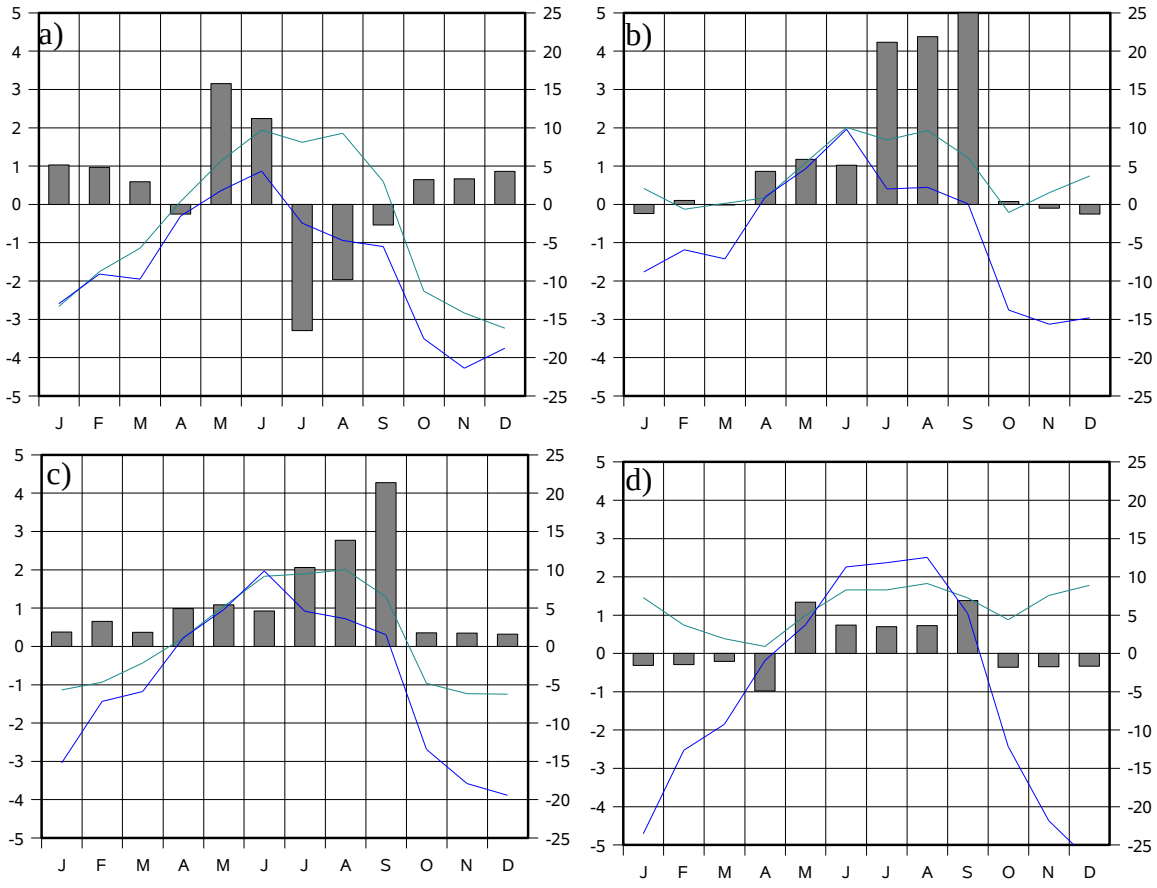

Fig. 7.4: Ratio of the upwelling from E0 to current-driven upwelling (w_{model} / w_{cur}, gray bars), vertical velocities from E0 (w_{model}, green lines), wind-driven vertical velocities (w_{cur}, blue lines) in the regions
a) Nha Trang, b) Cam Ranh, c) Phan Rang and d) Hoa Da
Unit of the vertical velocities: m day^{-1}

The ratio between the vertical velocities due to the onshore movement of the BBL and those simulated by E0 is given in fig. 7.4. In the northernmost area, during winter the ratio is close to 1. Current-driven upwelling seems to give a good approximation during northeast monsoon. During summer this relationship collapses. In May and June the vertical velocities

from E0 are 3 and 2 times stronger than those due to the onshore flow in the BBL. From July to September the ratio is negative, in July the ratio w_{model} / w_{cur} reaches a value of -3.
The Cam Ranh region has a negative ratio from November to January, hence neither the wind-driven upwelling nor the current driven-upwelling can explain the vertical velocities in this region. However, during spring, until June, the ration is 1 and so current-driven upwelling can approximate the vertical velocities well. With the change to state 6 in July and the associated confluence of the two boundary currents in this region, the vertical velocities from E0 are four times higher than those provided by the BBL.
In the region of Phan Rang, the ratio w_{model} / w_{cur} is positive the whole year. From October to March a ratio of O(0.5) shows that the negative vertical velocities due to current-driven upwelling are two times higher than those from the model. As in the Cam Ranh region, upwelling due to an onshore movement of the BBL can explain well the vertical velocities of the model from spring to early summer. Here too, the relationship collapses when state 6 is established in late summer. During late summer, the ratio increases from 2 in July to 4 in September.
In the southernmost region (fig. 7.4d) no coherence between the current-driven vertical velocities and those from E0 can be found from October to April. While the current-driven vertical velocities induce downwelling, the model simulates upwelling. However, during summer the the ratio is close to 1. Hence, current-driven upwelling gives a good approximation.
The correlation between the current-induced vertical velocities and the model results from E0, is 0.63, 0.28, 0.56, -0.08 for the regions of Nha Trang, Cam Ranh, Phan Rang and Hoa Da respectively.
This section illustrated that neither the local wind nor the current-induced transports in the BBL can explain the vertical velocities for all times and for all regions. Moreover, in the region of Cam Ranh and Hoa Da the two-dimensional processes fail completely in describing the vertical velocities. As a reference of western boundary upwelling areas, the Yucatan region may be mentioned. Merino (1997) thought that wind-driven divergence might not be an important mechanism for the upwelling in the Yucatan region. However, an interaction between the Yucatan current and the bathymetry and an interaction with the counter current seems to be more realistic. The upwelling off Yucatan can be found to be independent of the direction of the wind, hence his suggestions are acceptable. The results of the model (E0) let us suggest that in the VUA, besides the local wind and the transports through the BBL, the same processes are responsible for a part of the upwelling. The next chapter will describe how these vertical velocities can be reproduced using three-dimensional processes.

8

Coastal Upwelling Processes in three dimensions

In chapter 7, the simulated two-dimensional upwelling processes were illustrated. The horizontal and vertical circulations demonstrate that they can explain only a part of the vertical velocities. The use of only two dimensions neglects the inhomogeneity in the wind field and in the alongshore bathymetry. Thus, this chapter deals with the effect of these inhomogeneity on the governing process of the upwelling.

In the SCS the wind field builds a curl, in summer as well as in winter (chapter 2), hence, this chapter investigate in the vertical velocities due to this curl.

Moreover, neither the increase of the upwelling at some pronounced locations, nor the upwelling during northeast monsoon can be predicted neglecting the changes of the bathymetry in the alongshore direction. The appearance of increased upwelling at the same locations in different states of the horizontal circulation indicates a topographic steering, especially because the alongshore change of the depth is strongest in these areas.

The occurrence of upwelling in those regions with changing bathymetry is supported by Kling (1996). He simulated the behavior of vertical velocities in a canyon. Even in the case with the coast to the right of the main current (favorable to downwelling), his simulations yielded upwelling on the downstream side of the canyon.

In the figures of the vertical sections perpendicular to the coast in chapter 5, there are almost no closed circulation cells. These would be typical for two-dimensional upwelling simulations. Moreover, several vertical sections show that the equation of continuity is not fulfilled two-dimensionally. Hence, the $\delta v / \delta y$ term is an indispensable part of the equation, due to which the idealization made in equation 7.11b becomes questionable. This is also proved by the analysis of observations of different upwelling regions, done by Smith (1981).

8.1 The influence of the wind stress curl

Chapter 7 showed the two-dimensional upwelling processes, using an idealized wind field for wind driven upwelling, which was assumed to be homogeneous. In the SCS however, the wind field builds a curl, in summer as well as in winter (chapter 2). Yoshida (1967) pointed out, that there is always a curl between the land and the offshore sea. He established the equations of motions for a two-layer model and supported the thesis that the curl of the wind between the land and the sea is as important as the alongshore wind. The upwelling resulting from the wind stress curl and divergence and convergence of the Ekman transport can be calculated, using the continuity equation (7.11a). Integrating the equation (7.11a) with respect to z, and establishing the boundary condition w = 0 at z = 0 yields:

$$\frac{\delta m_{xe}}{\delta x}+\frac{\delta m_{ye}}{\delta y}-w_{ep}=0 \qquad (8.1)$$

According to the deductions made in section 7.1 the wind-induced mass transport is:

$$m_{xe}=\rho\cdot\frac{\tau_x}{f} \qquad (8.2a)$$

$$m_{ye}=\rho\cdot\frac{\tau_y}{f} \qquad (8.2b)$$

Equation 8.1 can be combined with equation 8.2, yielding the Ekman pumping velocity:

$$w_{curl}=\frac{\frac{\delta \tau_y}{dx}-\frac{\delta \tau_x}{\delta y}}{\rho\cdot f} \qquad (8.3a)$$

Thus, with the definition of the wind stress curl,

$$curl\,\tau=\frac{\delta \tau_y}{\delta x}-\frac{\delta \tau_x}{\delta y}$$

an estimation for the vertical velocities induces by the wind stress curl is found:

$$w_{curl}=\frac{curl\,\tau}{\rho\cdot f} \qquad (8.3b)$$

Vertical velocity due to the wind stress curl can be a significant part of the upwelling process. Münchow (2000) investigated the upwelling induced by the wind stress curl near Point Conception at the westcoast of the United States. Near Point Conception the coastline changes its orientation and thus establishes a cyclonic wind stress curl, forcing a cyclonic ocean circulation. Using a hydrodynamic model, Münchow simulated upwelling velocities

of O(4 – 10 m day^{-1}) induced by the curl of the wind stress. These magnitudes exceed the vertical velocities of the "classical" wind-driven vertical velocities at the Californian coast. Just as in California, the coastline in southern Vietnam changes its orientation. The occurrence of a wind stress curl at this location was shown in chapter 2. With equation (8.3b) it is possible to determine, whether the vertical velocities due to the curl have any relevance. With the wind stress field from QuickScatt the average wind stress curl for each day in the four regions (Nha Trang, Cam Ranh, Phan Rang, Hoa Da) in the VUA was calculated. The calculated vertical velocities due to the wind stress curl are small in comparison to the velocities from the model E0. On average, the wind stress curl is responsible for 10 - 20 % of the vertical velocities in the VUA. The absolute values never exceed 2 m day^{-1} .

8.2 Bathymetric-induced upwelling

The equations for the calculation of the vertical velocities deduced in chapter 7 and chapter 8.1 completely neglect all variation of the bathymetry, a simple flat bottom and a vertical wall at the coast is assumed. As an introduction, Bache (1860) will be mentioned, who observed lower temperatures at several areas in the Gulf Stream. He found a correlation between the change in bathymetry and the water temperatures. Hoffmann (1884) reported about cold water near the Agulhas-Bank where the Agulahs Current moves offshore. One of the first theoretical modelling studies of topographic effects on the upwelling process was that of Song (2002) and Song and Chao (2002). The latter used a sinusoidal-varying bathymetry, an upwelling-favourable wind stress forcing and a quasi-realistic stratification. They deduced that the upwelling process is strongly influenced by the bathymetry and the stratification. Due to the variations of the bathymetry, the currents start to meander, resulting in a change of vorticity, which results in upwelling. Even if the wind was upwelling-favourable, at pronounced locations downwelling could be found. They simulated a conservation of the total Ekman pumping. This means that the vertical net transport is the same as without the changing topography. As Kling (1996), Song and Chao (2002) used a completely symmetric bathymetry. As a result of the symmetry, the increase of upwelling on one side of a ridge is balanced by downwelling on the other side. This balance is disrupted without a symmetry of the bathymetry. According to Cruzado and Salat (1981), it can be proven, that the upwelling caused by interaction of the Canary Current with the changing bathymetry is as strong as the upwelling related to the local wind stress. The occurrence of upwelling during winter supports the thesis that in the VUA this process can exceed the wind-driven or current-driven upwelling.

The effect of the topography can not be calculated using a simple approximation equation, as it was possible with the two-dimensional processes. For this reason, the magnitude of the three-dimensional process is defined as the residual value calculated as differences between the vertical velocities from the model experiment E0 and the wind-driven, current-driven and wind-stress-curl-driven processes. As shown before, current-driven and wind-driven upwelling superimpose each other; a two-dimensional vertical velocity, w_{2D}, is defined as the higher absolute value of the two-dimensional processes.
Combined with the vertical velocities induced by the wind stress curl, the effect of the changing bathymetry can be approximated:

$$w_{bath} = w_{E0} - (w_{2D} + w_{curl})$$

It has to be admitted, that this calculated vertical velocities can not be found in nature. They are defined as residual vertical velocities, which, combined with the other processes, yield the "real" simulated vertical velocities.
Fig. 8.1 shows the distribution of the magnitude of the monthly averaged bathymetry-induced vertical velocities for the four areas defined in chapter 2. It can be seen that in the Nha Trang region, where the bathymetry is homogeneous in the alongshore direction, no significant vertical velocities (> 5 m day^{-1}) can be found. This is not a surprising result, considering that two-dimensional processes explain the upwelling quite well in this region.

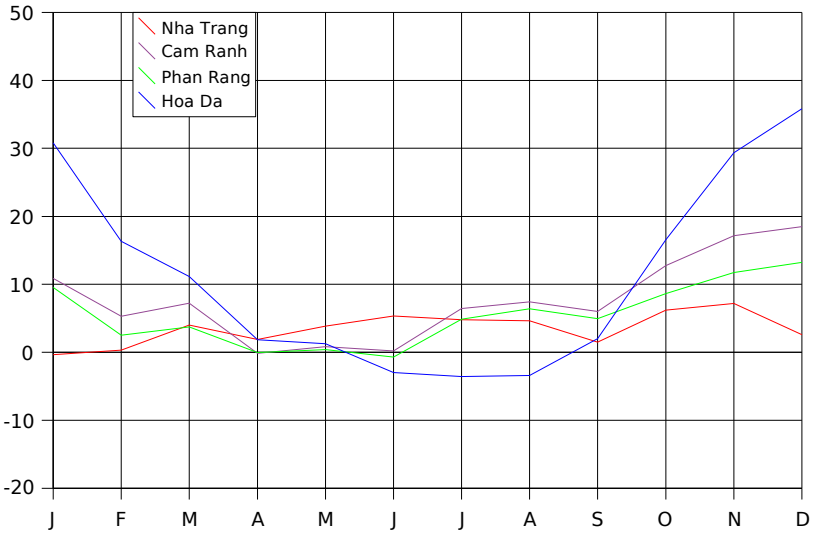

Fig. 8.1: Monthly variability of the vertical velocities induced by the bathymetry in the four regions. Units: m day^{-1}

In the canyon-like structure, the Phan Rang region, vertical velocities of O(15 m day^{-1}) occur during winter. The vertical velocities of E0 are also negative in this region, but due to the bathymetry, they are lower than the two-dimensional processes would suggest.

In the regions, which show upwelling during winter, Cam Ranh and Hoa Da, the magnitudes of w_{bath} indicate a significant role of the alongshore bathymetry. The calculated bathymetry-induced vertical velocities can reach more that 40 m day^{-1} in the monthly mean.

The magnitude of the upwelling induced by the bathymetry should correlated with the alongshore velocity of the current. Fig. 8.2 illustrates the relationship between the alongshore current and the magnitude of the vertical velocities due to the bathymetry. The magnitudes of the horizontal velocities are related to those of the vertical velocities for each day of E0.

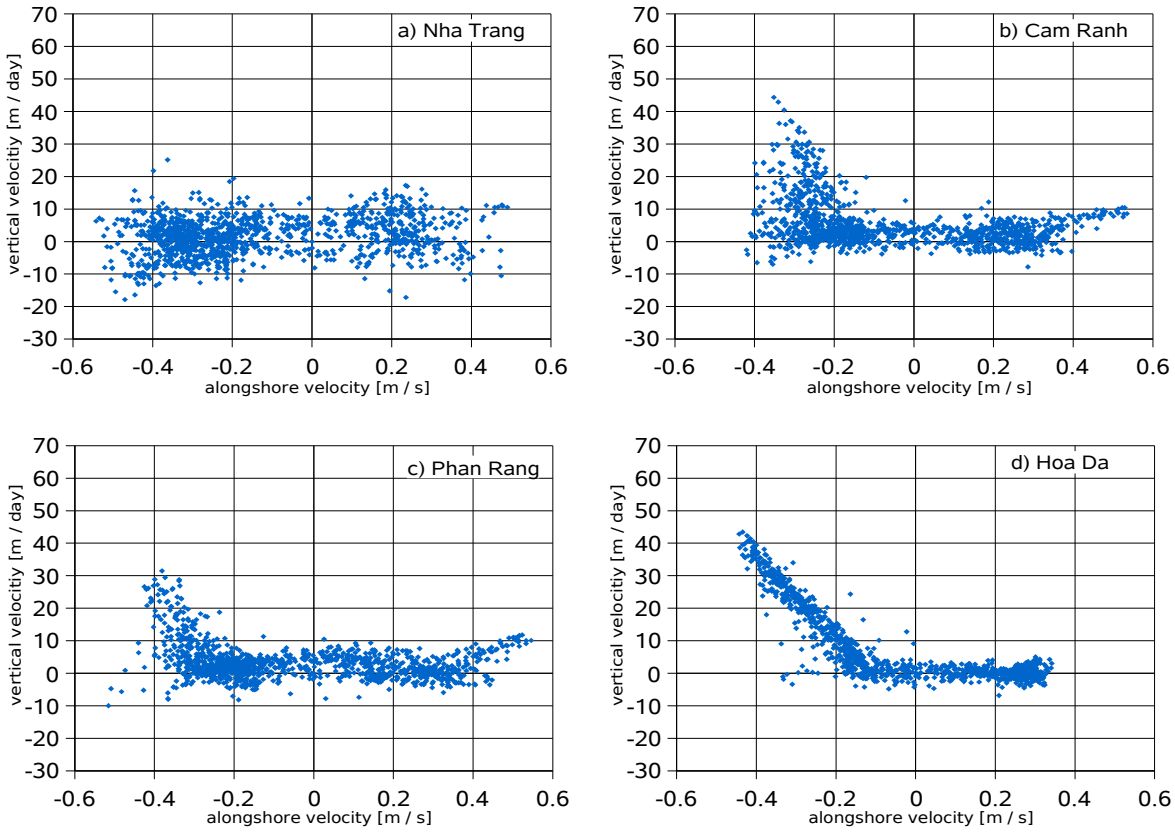

Fig. 8.2: Scatterplot of w_{bath} in relationship to the alongshore currents

As expected, there is no relation to be found between the currents and w_{bath} in the region of

Nha Trang, but a scattering of the residual vertical velocities of about 10 m day^{-1}. This may be a result of the averaging process or of mesoscale non-deterministic flow interactions. In the Cam Rang region and the Phan Rang region, a southward current velocity higher than 0.2 m s^{-1} is a necessary condition to simulate positive vertical velocities. A reason for the current velocity only being a necessary condition, may be the stratification of the water. Only in the southernmost region a clear relationship between the horizontal and the vertical velocities can be found. If the current is southward and the magnitude is greater than 0.2 m s^{-1}, w_{bath} increases linearly with the current speed. This shows that the current has to exceed a minimum velocity to induce vertical velocities.

Fig. 8.2 illustrate that the bathymetric induced vertical velocities appear if a strong southward current appears on the shelf. In literature a current with the coast to the right is referred to be downwelling favourable, like it was shown in the last chapter, thus a process which differs from the classical upwelling processes has to be responsible for the vertical velocities. The processes illustrated in this and the next sections refer to the interior of the water column, to neglect the effect of friction. This is done knowingly to separate these processes, a completely reconstruction including all superimposed processes is done by the simulation with HAMSOM (E0).

Fig. 8.3 shows a flow-chart of the theoretical mechanism which can explain the positive vertical velocities induced by the southward boundary current.

The process consists on three steps:

1. If the shelf changes its depths, it is necessary that the inertial forces exceeds the effect of gravity to allow the current to flow cross the isobathes, thus upward into shallower water. This mechanism is based on the hydraulic theory (Long, 1954), in which a flow over an obstacle is simulated. The relation of the inertial forces and the effect of gravity is given by the Froude number:

$$Fr = \frac{v}{\sqrt{g' \cdot d}} \qquad (8.4)$$

In this equation, v is the current velocity, g' the reduced gravity and d is a characteristic change of the depths.

The reduced gravity is defined with:

$$g' = \frac{g \cdot \delta\rho}{\rho_0}$$

where ρ_0 is the reference density, and $\delta\rho$ is the differential change in density with depth.

With the definition of the buoyancy frequency, the Froude number can be written as:

$$Fr = \frac{v}{N \cdot d} \qquad (8.5)$$

If Fr > 1, the flow is called supercritical and the inertial forces overcome the gravitational forces. If this applies, the flow crosses the isobathes and is forced into shallower water. Equation 8.5 shows that the Froude number depends on the buoyancy frequency, thus the stratification. If the vertical density differences are strong, the current is blocked by the bathymetry, and the current is forced to flow round the obstacle. Chapter 8.5 deals with the relation between the Froude number and w_{bath} simulated by the model.

2. The second important process is the conservation of Potential Vorticity:

$$\frac{D}{Dt}\frac{(\zeta + f)}{d} = 0 \qquad (8.6)$$

In this equation ζ is the relative vorticity and f the Coriolis Parameter (the planetary vorticity).

A decreasing d causes a decrease of $(\zeta + f)$ to accomplish equation 8.6. The lowering of the depth may be counterbalanced with the change of the Coriolis parameter in the meridional direction, hence:

$$\frac{D}{Dt}\frac{f}{d} = 0 \quad ; \text{i.e.,} \quad \frac{f}{d} = const \qquad (8.7)$$

For an individual fluid trajectory, this yields: $\frac{(f + \delta f)/f}{(d + \delta d)/d} = 0$.

From this a necessary change of the Coriolis parameter due to the changing depth can be calculated: $\delta f = \left(\frac{d}{d + \delta d} \cdot f \right) - f$

For the region of Cam Ranh (11° 30' N – 12° N) the following parameters can be found:

- $d = 180\,m$ at 12° N
- $f = 3.03 \cdot 10^{-5} s^{-1}$ at 12° N
- $\delta d = d_{11°30'N} - d_{12°N} = -90\,m$

Using this parameters a theoretical value for $\delta f = -1.35 \cdot 10^{-5} s^{-1}$ have to occur. The real value of the change of the Coriolis parameter at this location is to be found: $\delta f = f_{11°30'N} - f_{12°N} = -1.25 \cdot 10^{-6} s^{-1}$. This illustrates that the flow cross the isobathes are not counterbalanced by the Coriolis parameter, but a significant rotation of the current due to the relative vorticity is forced. Moreover, the assumption of a constant Coriolis parameter yields an error being less than 10 %. Using the equation 8.6, it can be concluded,

that the relative vorticity have to decrease, which implies that $\frac{D}{Dt}\zeta$ has to be negative. Thus, the flow is forced to rotate anticyclonic. An anticyclonic rotation of a southward directed current forces a component towards the coast.
Nevertheless, in contradiction to the two-dimensional processes, the flow of the current is mainly in the alongshore direction. The distribution of the relative vorticity during different states of the circulation and a discussion in more detail is presented in chapter 8.6.

3. It was shown, that a high Froude number yields the boundary current to cross isobathes. Second, it was concluded that this let the flow rotate more in the direction of the coast, which forces an increased flow into shallower depths.
From the kinematic boundary condition, it can be concluded, that the flow relative to the bottom must be tangential to it. Using this condition, a vertical velocity of a flow on a sloping bottom can be calculated:

$$w_{z=b} = u \cdot \frac{\delta b}{\delta x} + v \cdot \frac{\delta b}{\delta y} \qquad (8.8)$$

In this equation, δb is defined as the change in the bathymetry relative to the initial depth, thus if the bottom is planar δb is zero. On a sloping bottom, δb is not zero, the vertical velocity depends on the change of the bathymetry. Thus, if a current crosses the isobathes into shallower water $(\delta b > 0)$, upward vertical velocities can be calculated. The upward motion particularly near the bottom, can be found in the vertical sections of the vertical velocities (fig. 5.1) in chapter 5.

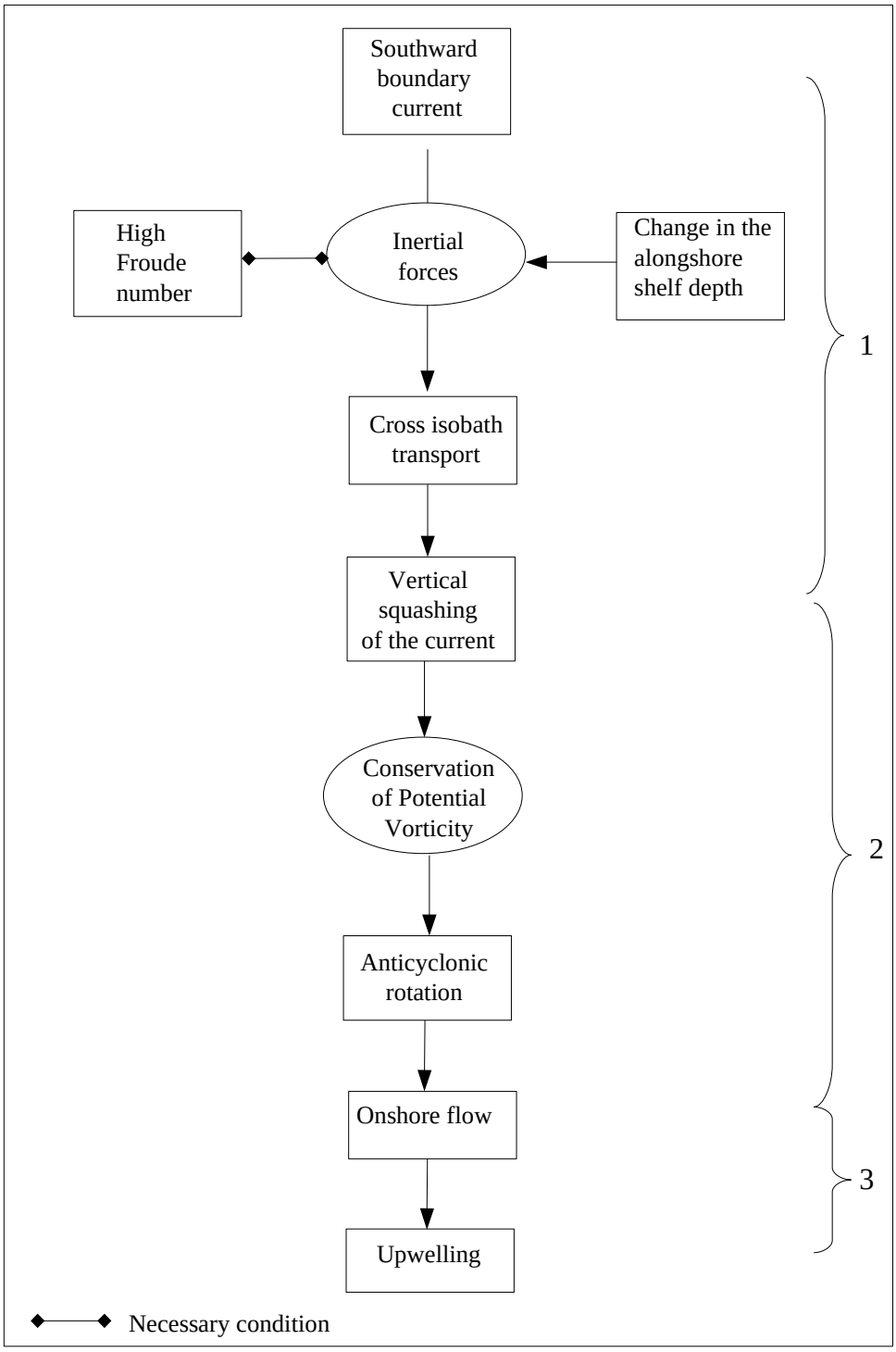

Fig. 8.3 : Upwelling mechanism induced by the change of the alongshore bathymetry and the interaction with the southward boundary current.
The mechanism contents of three steps, three necessary conditions have to be fulfilled.

In this section a possible theoretical mechanism concerning the upwelling induced by the southward boundary current, interacting with the bathymetry, is illustrated. Unlike the two-dimensional processes, this upwelling mechanisms is strongly related to the alongshore motion. Nevertheless, a mass of water moves upward and shoreward in response to bathymetric changes.

Besides the change in depth the widening of the shelf can influence the upwelling. Pringle (2002) simulated enhanced transport onto the shelf in a coastal ocean, if the shelf widens in the direction of the alongshore current. The change in shelf width only affects the flow in the direction of coastal trapped Kelvin wave propagation from the change in shelf width. The VUA can be found downstream of a significant widening of the shelf (chapter 2) in the direction of Kelvin wave propagation, hence this may increases the onshore flow.

During summer, the complex situation, with two boundary currents complicates the interpretation. Particularly, during state 6 of the circulation (chapter 5) a strong offshore directed jet can be found. As it was shown in the observations (chapter 6) and in the simulation, also during state 5 the boundary current separates slightly from the coast.

Xie (2003) shows that the wind-stress-curl over the SCS does not determine the separation process, since he found a discrepancy between the wind forcing and the response of the sea surface heights. The theory behind this thesis is supported by Cessi et al. (1987), who presented numerical studies in which anticyclonic wind stress forcing is applied over the southern part of a rectangular basin with no forcing to the north. Nevertheless, the western boundary current extended to the northernmost margin of the basin, without separating at the line of vanishing wind stress curl. The former deductions illustrated the importance of the conservation of potential vorticity. This agrees well with the findings of Greenspann (1963), Jankowitz and Pietrafesa (1982), Özgökmen et al. (1997), Stern (1998) and Spitz and Nof (1991). These publications deal with the separation of boundary currents and come to the conclusion, that topographic steering due to the conservation of potential vorticity is the main process in the separation of boundary currents from the coast. Another interesting aspect of the current separation is, that downstream from the separation point, upwelling is increased.

As the change of the alongshore bathymetry, a curvature of the coastline can induce the same effects. Kelly (1985) and Dale and Barth (2000) found that jets tend to move offshore downstream from capes, leaving a pool of dense upwelled water inshore. As well, they can explain the upwelling with the potential vorticity. Marshall and Tansley (2001) developed an implicit formula for the boundary current separation in the case of the curvature of a coastline. To induce the separation of a western boundary current, the current must exceed the stabilising influences of the beta effect. They found a idealised formulation for the separation process:

$$r < \sqrt{\frac{v}{\beta}} \tag{8.9}$$

In this formulation v is the velocity of the current.

As mentioned before, in the VUA the coastline changes its direction.

With $\beta = 2.25 \cdot 10^{-8} s^{-1} m^{-1}$ and a boundary current of the magnitude O(0.5 m s^{-1} – 1 m s^{-1}) during summer, the radius of curvature has to be less than O(150 km - 200 km).

The curvature of the coastline at 11° 30' just meets this condition. Hence, besides the change of the shelf depth, the curvature may support the offshore jet.

However, it may be unique to the VUA, that there is a variable bathymetry and in summer two boundary currents collide. In the model result (E0), a strong offshore jet can be found in state 6. The confluence zones can always be found at the same pronounced locations, indicating topographic steering. However, according to Lebedev and Nof (1996) the strengths of both boundary currents can also control the point of collision. They investigated the confluence zone of the boundary current off Brasil, the Brasil-Malvinas confluence. Using a nonlinear inviscid reduced gravity model on a *f*-plane, they produced some remarkable results. The counter-current forces the main current in an offshore direction. The point of separation depends on the transports of both currents, variations in the transports result in meandering of the offshore flow. An interesting conclusion of their studies is, that the transport of the main current is completely controlled by the counter current. However, this result has to be judged with care, Lebedev and Nof are not sure, whether this effect is due to their idealizations. On the other hand, Thomson and Schmitz (1989) showed that the pathway of the Gulf Stream is in almost the same manner controlled by the counter current. The findings of experiment E1, that the averaged cyclonic circulation in the north may influence the average anticyclonic circulation in the south, supports this thesis. Summarized, it can be concluded that the strengths of both boundary currents and the bathymetry are responsible for the occurrence of the strong offshore jet.

8.5 Inertial Forces and changes in the shelf depth

The process of inertial forces driving a flow cross isobathes were shown in the last section, if this is responsible for the bathymetric induced upwelling a correlation between w_{bath} and the Froude Number has to be found. In the VUA, the current does not flow over a ridge like in the publication of Esler et al. (2005), but up the slope due to changes in the alongshore bathymetry. The depth d can be taken as the half of the water column, which represents approximately the change of the alongshore depth in each region. Hence, the depth changes from 180 m to 90 m , form 120 m to 60 m and from 60 m to 30 m in the Cam Ranh region, the Phan Rang region and the Hoa Da, respectively. In the region of Nha Trang, no change in the alongshore depth can be found, and as it was shown in fig. 8.2, no w_{bath} can be found.

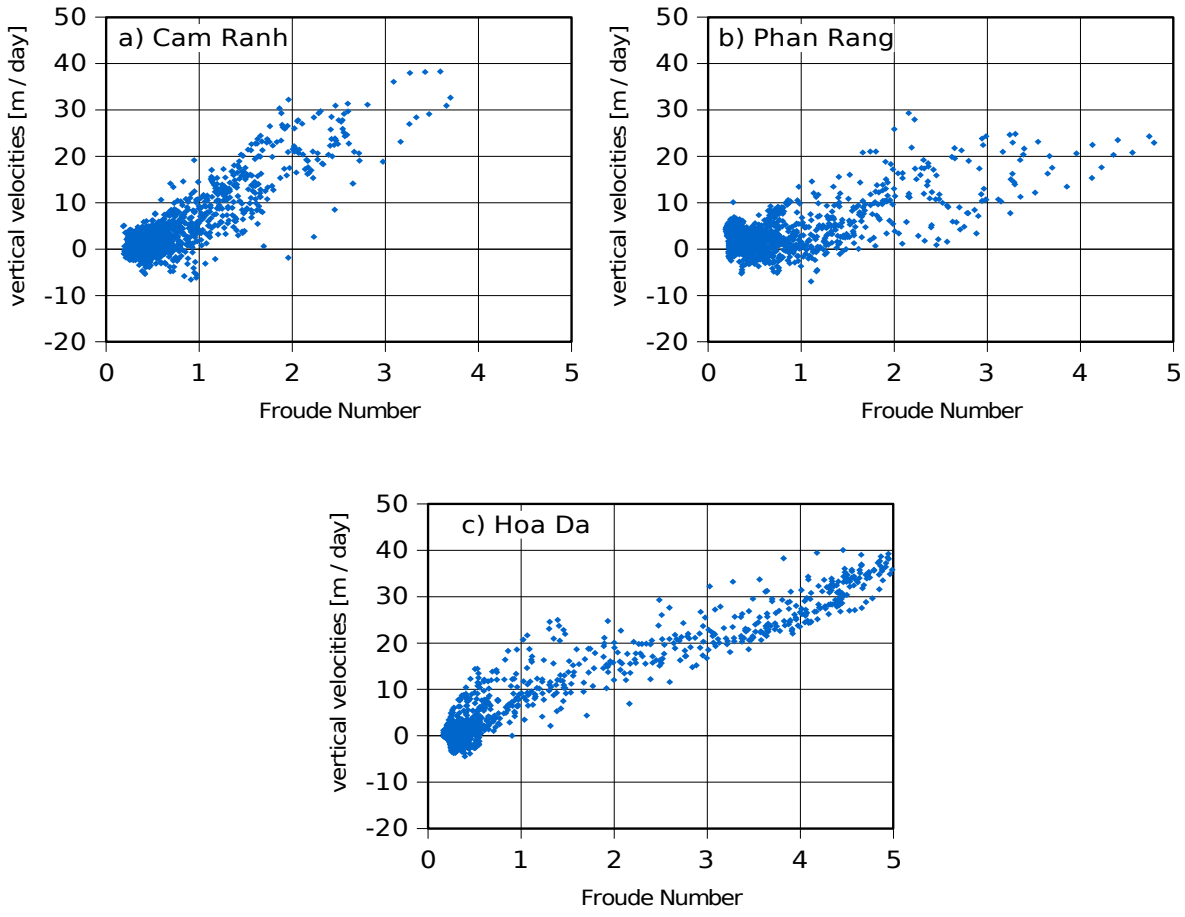

Fig. 8.4: Scatterplot of w_{bath} in relationship to the Froude number

Fig. 8.5 illustrates the relationship between the Froude number and w_{bath}. The buoyancy frequency N and the current velocity v is calculated from the results of E0

The relationship is only slightly visible in the canyon-like structure of Phan Rang. A better relationship can be found in the Cam Ranh region and the Hoa Da region. The correlations at Cam Ranh, Phan Rang and Hoa Da are 0.87, 0.71 and 0.95, respectively.

For the possible occurrence of upwelling, a minimum Froude number of 1 was expected, but, in contrast to the relationship of the alongshore currents and w_{bath}, a minimum value for the Froude number can not be found.

Summarized, if the stratification is taken into account, it was shown that the first part of the mechanism deducted in the last section, is considered to be a relevant process.

8.6 The conservation of potential vorticity

Neumann (1960) described two solutions of how the change of the bottom topography can influence ocean currents, one according to Ekman (1923) and the other one to Sverdrup (1941). In Ekman's solution, a friction-driven circulation is deflected to the right when the depth decreases. The magnitude of the deflection is independent of the water depth itself, but depends on the slope of the bottom. A net displacement of the streamlines takes place. Sverdrup deduced that the streamlines are deflected on the upstream side of a ridge, but turn back on the downstream side of the ridge, which he could explain with the Coriolis force. Sverdrup assumed a geostrophic current and neglected the effects of frictional forces. Besides friction, the key process of the interaction between currents and bathymetry is the conservation of potential vorticity. Recent publications (e.g. Gill and Schumann, 1979, Song, 2002) emphasise the influence of potential vorticity on the currents in upwelling regions.

From the results of the long-term run (E0) a relative vorticity can be calculated, which is given by:

$$\zeta = \frac{\delta v}{\delta x} - \frac{\delta u}{\delta y} \qquad (8.10)$$

A idealised two layered sea is assumed. For simplification the first layer is defined as the upper half of the water column and the second layer is defined as the lower half of the water column, hence the interface between both layers describes not a horizontal plane. The interesting motion of the upwelling circulation is related to the deeper layer. The lower half of the water column is of interest, because it approximately reflects the water mass, which will be moved upward.

The simulated currents of the model (E0) are used to calculate the relative vorticity.
Fig. 8.5 illustrates the distribution of the relative vorticity in the lower half of the water column for state 1 (fig. 8.5a), state 3 (fig. 8.5b), state 5 (fig. 8.5c) and state 6 (fig. 8.5d), being the states with the highest vertical velocities. In the figure, the locations that show increased positive vertical velocities are marked with blue ellipses. The change of the alongshore bathymetry is visualised with brown dashed lines, which represent the crestlines of the ridge (11° 40' N) and the beginning of the Sunda shelf (chapter 2). Remarkable features are highlighted as in chapter 5.
In state 1 (fig. 8.5a), on the northern shelf, the distribution of relative vorticity is irregular (F1). As it can be seen in the horizontal velocities (fig. 5.1c, 5.1d), the flow of the current is strongly disturbed by mesoscale bathymetric characteristics, like sea mountains, resulting in instabilities in the flow. Off the shelf, the vorticity is cyclonic (F2), which can be seen as well in the distribution of horizontal currents. Noticeable is the anticyclonic relative vorticity of the currents in the upstream direction of the two upwelling areas (F3, F4), which are congruent with the change in the alongshore depth (brown dashed lines).
The connection between the anticyclonic rotation in these regions and the upwelling downstream has to be discussed. Because the velocity of the current in the zonal direction is small in comparison to the velocity in the meridional direction, u can be set to zero. Results from the long-term run of the model provide a ratio *v/u* of O(20).
With the neglect of external forcing, meaning no change of $\delta\zeta/\delta t$ and u = 0, the change of the relative vorticity is:

$$\frac{D\zeta}{Dt} = v \cdot \frac{\delta\zeta}{\delta y} \qquad (8.11)$$

In the regions upstream from the positive vertical velocities, the shelf becomes shallower to the south. This means $\delta d/\delta y$ is positive. In a southward current, the velocity v in equation (8.11) is negative, and thus, equation (8.6) can only be true if the relative vorticity is negative, as well. This may happen under two conditions: the first is, that $\delta v/\delta x$ is negative, the second is, that $\delta u/\delta y$ is positive.
Assuming the current is not rotating downstream the upwelling. If the water is becoming shallower, $\delta v/\delta x$ can become negative, thus a shear on the the right side of the current appears. The second possibility, hence $\delta u/\delta y$ is positive illustrates that the current tends to rotate anticyclonicly in the direction to the coast, coming into shallower water, thus the flow crosses the isobaths. The change of the relative vorticity could be an explanation for the distribution of the vertical velocities in the alongshore section and the sections perpendicular to the shore of state 1.
The distribution of relative vorticity in state 3 (fig. 8.5b) shows the same scattering in the northernmost part (F1) of the VUA. Offshore from the region of increased upwelling, an

anticyclonic rotation (F2) of the current can be found. The southward current, which is present in the lower half of the water column, rotates in the onshore direction, thus into shallower water. In the upwelling center, south of Cam Ranh (F3), the currents are directed northward south of the ridge and southward north of the ridge. The cyclonic rotation south of the ridge and the anticyclonic circulation north of the ridge comply well with the onshore rotation of the horizontal currents in larger depths. Anticyclonic currents can also be found downstream from the third region of upwelling (F4) of this state. The explanation of this distribution is the same as for state 1, except for the cyclonic rotation south of the ridge.

However, during state 3, no significant wind forcing is present, thus the effect of the Potential Vorticity doesn't have to exceed the influence of the local wind forcing to induce upwelling. Also, the inshore recirculation (fig. 5.3a) may be explained with this process.

The distribution of relative vorticity of state 5 can be seen in fig. 8.5c. As in winter, on the northern shelf, the relative vorticity has a disordered structure. Remarkable is the positive relative vorticity of the flow upstream from the region of enhanced upwelling. A positive relative vorticity causes a cyclonic rotation, hence, considering the northward direction of the main current, the flow rotates towards the shore. As in state 1, $\delta d / \delta y$ is positive, but now the relative vorticity has to be positive, because the velocity v is positive. As in the case of the southward boundary current, an inshore deacceleration and an onshore rotation flow can be seen in the horizontal circulation.

These findings were confirmed by the model of Song et al. (2001), who simulated the formation of upwelling centers downstream from ridges. Recapitulating, it can be said, that in a flow with the coast to the left, the lower part of the water column rotates cyclonicly where the shelf deepens, resulting in increased onshore flow. Hence, the vertical velocities and the offshore flow of the upper layer are intensified in these regions.

The second summer state (state 6, fig. 8.5d) shows a more scattered distribution of the relative vorticity, which is not surprising, considering the complex horizontal circulation of this state. The most obvious feature is the positive vorticity off the shelf (F1, F2) due to the shear induced by the southward boundary current and the anticyclonic circulation in the deep basin. East of the upwelling (F3), negative relative vorticity occurs. This can be seen as well, in the horizontal circulation in depths of 50 m and 80 m in fig. 5.6b and fig. 5.6c, respectively. In this region and these depths, the boundary current rotates anticyclonicly, which results in a strong onshore flow. At F4, the relative vorticity is positive, which, due to the northward flow, results in an onshore flow of the deeper part of the water column.

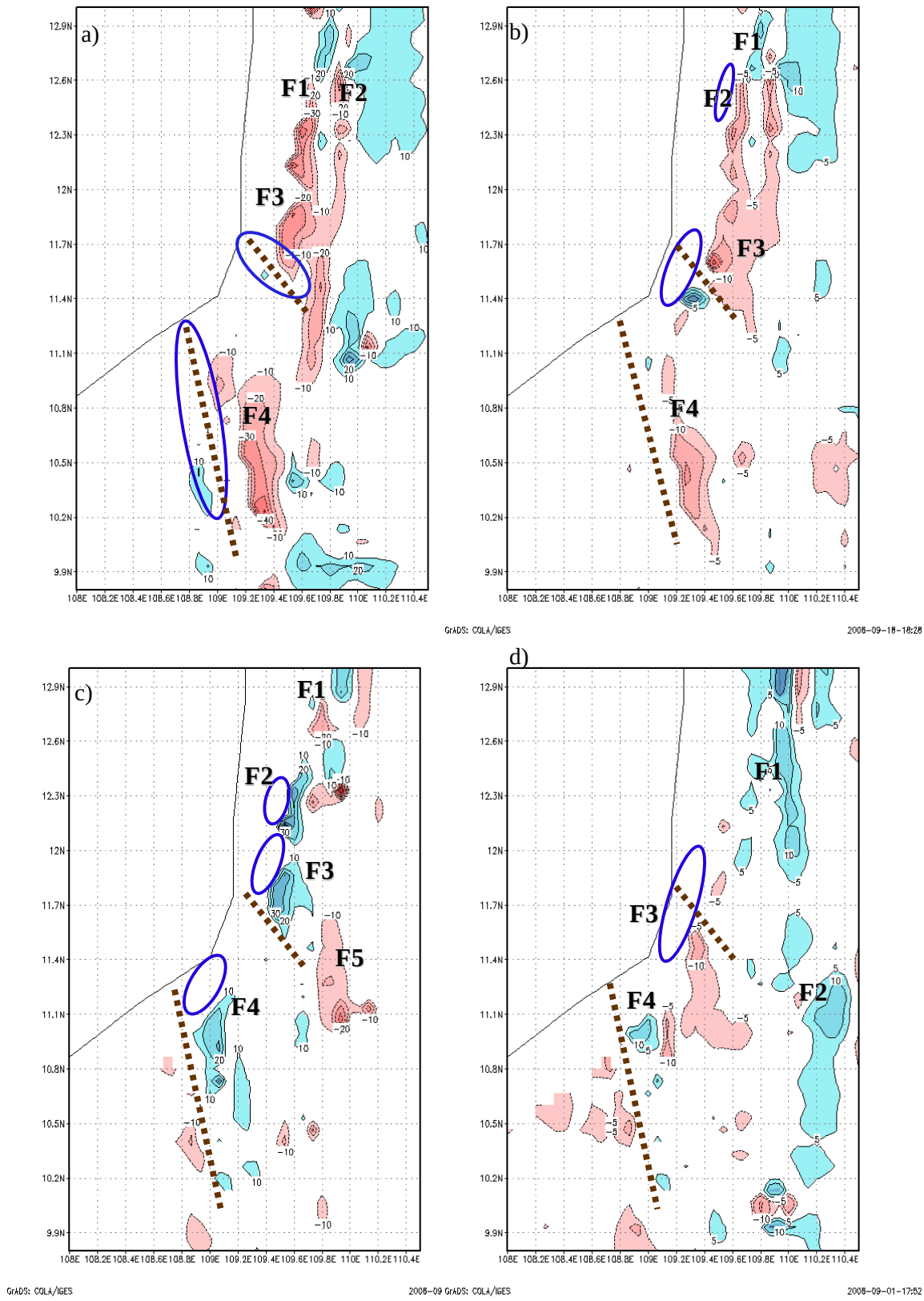

Fig. 8.5: Horizontal distribution of the relative vorticity in the lower half of the water column, for state 1 (a), state 3 (b), state 5 (c) and state 6 (d). Unit: $1\times10^{-5}[s^{-1}]$.

The appearance of increased upwelling is correlated with the distribution of relative vorticity, hence the conservation of potential vorticity is a significant process in the VUA. Moreover, if the change of the alongshore depth, is as high as in the VUA, this process can exceed the effects of both two-dimensional upwelling processes.
This section showed, that the strong change in the alongshore depth resulting in a onshore rotation of the current, thus in shallower water and with that upwelling is increased during summer or appears during winter.
Summarized, this and the section before showed, that the theoretical mechanism illustrated in chapter 8.2 is plausible the process to induce upwelling due to the interaction of the southward boundary current and the bathymetry.

8.3 The influence of the local wind on the vertical velocities

The last sections illustrated the upwelling due to the boundary currents. Huthnance (1985) showed in a review of shelf edge circulations that the circulation contributions from a western boundary current are about one order of magnitude larger than those from other coastal or slope currents, irrespective of the local forcing. This does not mean that the local wind can not force upwelling. During summer, the currents driven by the local wind interacting with the bathymetry or the basinwide circulation interacting with the bathymetry, may explain those vertical velocities in the VUA that are not related to the two-dimensional processes. Thus, a model experiment (E2) was conducted. In this experiment, the nature of the spin-up process is utilised. As in E1, in the spin-up phase a basin wide circulation is not present yet, only the local forcing affects the local currents. To prevent any influence of the basin-wide circulation, the model is restarted after a simulation time of one week.
With this method, the current field of summer of 2004 was simulated. The idea of using the spin-up time of a three-dimensional model was introduced by Leth and Middleton (2004a), who used this method to separate the effect of local wind stress from that of eddy advection.
In E2 a realistic wind field was used to include the effects of the wind stress curl. To avoid any influence of external effects, the open boundaries were closed. An average stratification is given by the Levitus (Boyer, 1998a, 1998b, 1998c) dataset.
To prevent influences of the difference in the stratification between long-term run E0 and the spin-up run E2, the vertical velocities of E2 are scaled by the factor $\sqrt{A_{vE2}/A_{vE0}}$ with A_{vE0} and A_{vE2} defined as the vertical coefficient of turbulent viscosity of model experiment E0 and E2, respectively. This scaling is necessary, because E2 uses the Levitus dataset and the stratification is much lower than that from E0. As equation 7.17 shows, wind

driven vertical velocities depend on a length scale L_x. This length scale is related to the vertical turbulent viscosity coefficient (equation 7.18), thus on the stratification and with that a scaling of the vertical velocities are necessary to match both experiments.

Fig. 8.6 shows the vertical velocities from the long-term run of the model (E0), those from the weekly spin-ups (E2) and those calculated with the approximation equation (7.17b) for the four areas defined earlier. The comparison between the long-term run E0 and the spin-up run E2 shows some interesting features. In the two northern areas, the vertical velocities of E0 and E2 are very similar. At the end of July, this similarity ceases and the alongshore currents of E0 suggest a strengthening of the northward boundary current. In both areas, the influence of the local wind is O(50 % - 60 %).

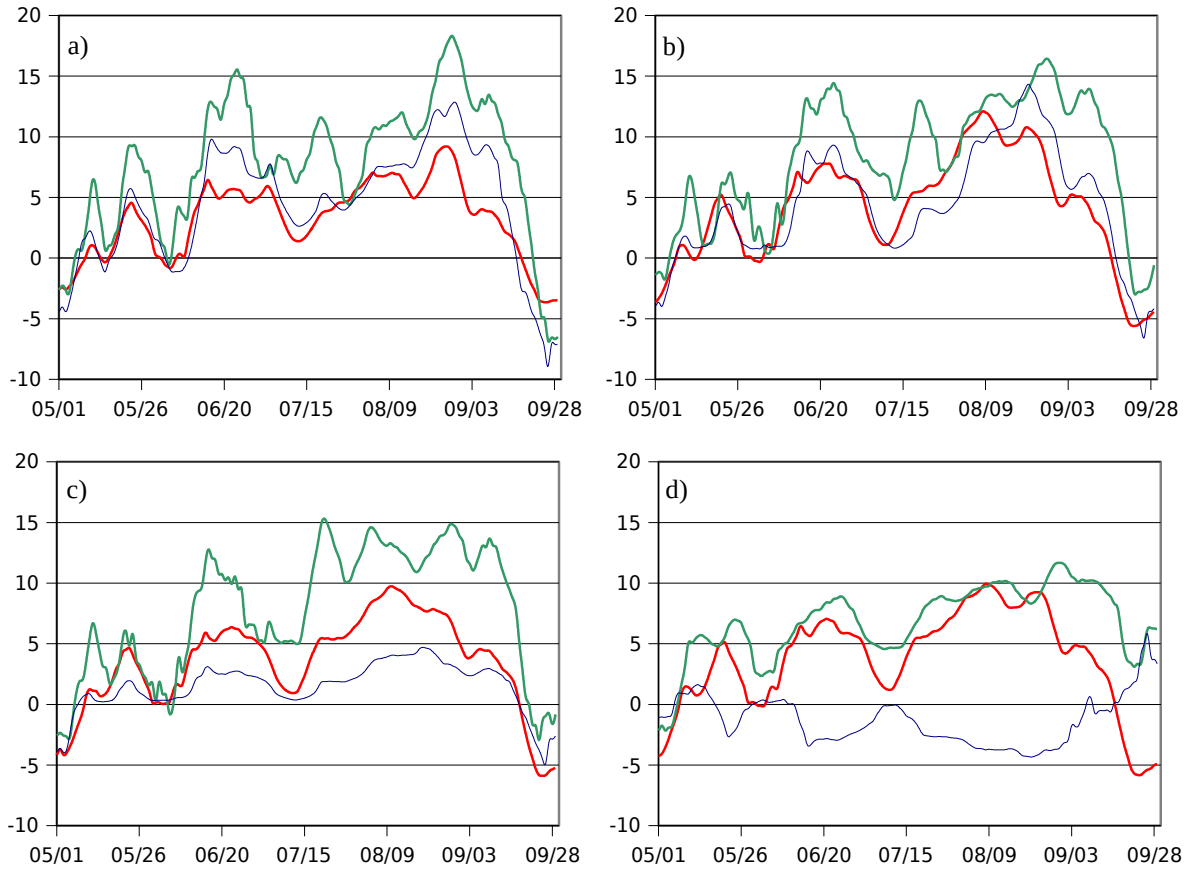

Fig. 8.6: Distribution of the vertical velocities during the summer of 2004, from E0 (green line), from E2 (blue line) and calculated with the alongshore windstress (red line)
for the regions of Nha Trang (a), Cam Ranh (b), Phan Rang (c) and Hoa Da (c).
Units: m day^{-1}

In the region of Phan Rang, the local wind induces only O(20 %) of the vertical velocities, the boundary current, which interacts with bottom friction and the changing bathymetry, is by far the more important process. However, it has to be mentioned, that the correlation between the wind stress and the vertical velocities is high, with a significant value of 0.8 in this region. This is not a surprising result, regarding that the overall circulation of the SCS is mainly forced by the wind stress. Interestingly, in the southernmost region, the local wind produces negative vertical velocities. Due to the bathymetry, in this region, the drift current causes downwelling to occur even though the wind is favorable to upwelling. Song et al. (2004) reproduced the same results for pronounced areas of their variable topography. Thus, in the Hoa Da region, only the boundary current is responsible for the positive vertical velocities.

8.7 The influence of the Mekong

The cruises illustrated that during summer water masses influenced by the Mekong flow into the VUA. The occurrence of a plume of this water mass (MKW) can be seen in the distribution of salinity of both summer cruises. The influence of the stratification on the vertical turbulent viscosity coefficient, and thus the vertical velocities, has been illustrated before. Hence, the summer of 2004 was simulated in a model experiment (E3) excluding the Mekong river to deduce its influence.

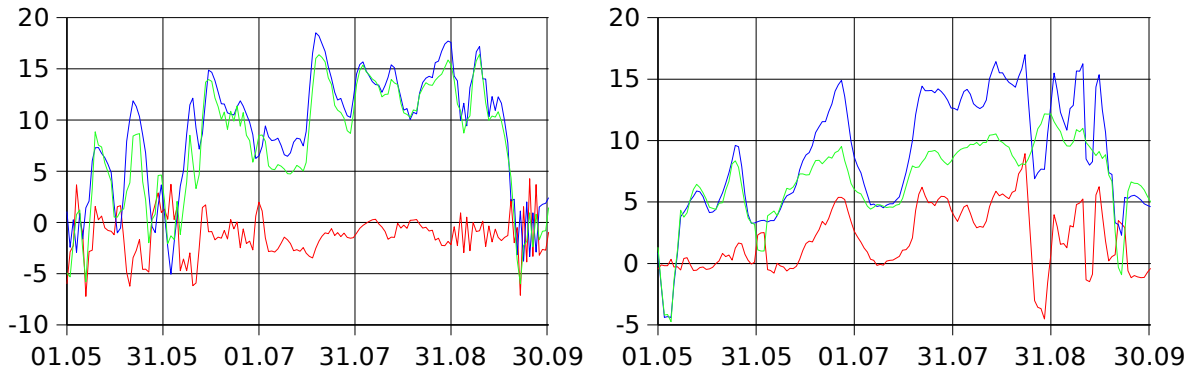

Fig. 8.7: Distribution of the the vertical velocities during the summer of 2004, including riverine discharge (green line), without riverine discharge (blue line) and the differences (red line) in the region of Phan Rang (left side) and Hoa Da (right side). Units: m day^{-1}

Fig. 8.7 shows the vertical velocities of E0, E3 and the difference between both experiments for the two southern regions, Rhan Rang and Hoa Da, respectively. In the figure, the green lines represent the vertical velocities from E0, the blue lines those from E3 and the red lines the differences between both.

The results demonstrate well the influence of the riverine discharge, especially in the Hoa Da region the influence is significant. During May, the influence is low, but the vertical velocities of E0 are lower with the beginning of a stronger discharge and a stronger advection of the Mekong water in mid-June. On average, the upwelling is increased by O(20 %) without the Mekong, but the increase can reach a magnitude of O(50 %). As it would be expected, to the north, in the Phan Rang region, the influence is only O(15 %). In the Cam Ranh region, the influence of the Mekong is only O(9 %). The standard deviation of the differences is σ_{diff} = O(2.5 m day^{-1}) in the Hoa Da region and σ_{diff} = O(4.7 m day^{-1}) in the Phan Rang region. The higher standard deviation illustrates that the Mekong plume only flows into the Phang Rang region at certain times. The distribution of the vertical turbulent viscosity coefficient of both experiments are shown in fig. 8.8. The change due to the absence of the Mekong is significant in the Hoa Da region, where the coefficient including the Mekong (E0) is only O(56 %) of that without riverine influence (E3). In the Phan Rang region, the influence of the Mekong on the vertical turbulent viscosity coefficient is still present.

These results may explain a peculiar result of the observations of VG7 at track 6. Surprisingly, the distribution of the temperatures illustrates that at the second observation of this track, after the strong monsoon event, there was no cooler water to be found near the coast. This could be explained with the stronger advection of low-salinity water, as it was found in the second plume after the storm. Considering the results of E3, this near-shore plume significantly reduces the vertical velocities.

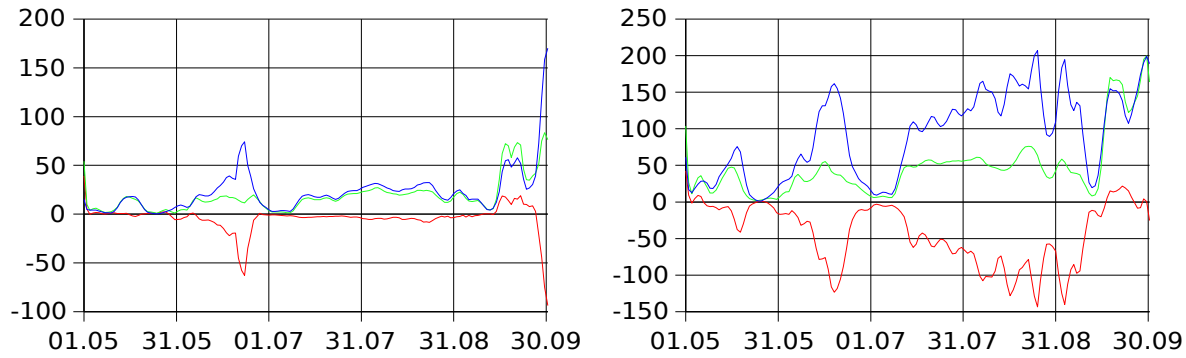

Fig. 8.8: Distribution of the vertical turbulent viscosity coefficient during the summer of 2004, including riverine discharge (green line), without riverine discharge (blue line) and the differences (red line) in the region of Phan Rang (left side) and Hoa Da (right side)Units: cm^2 s^{-1}

9

Inter-annual variability

This chapter investigates the inter-annual variability of the upwelling off Vietnam and its relationship to the El Niño/Southern Oscillation (ENSO). The ENSO is the most important coupled ocean-atmosphere phenomenon to cause global climate variability on inter-annual time scales. Xie (2003) found a correlation between the cold offshore jet during summer and the ENSO with a time lag of half a year. However, the observations of the cruises (chapter 6) illustrate that the sea surface temperatures measured by satellite do not offer a good approximation for the strength of the upwelling. Especially the fact that the upwelling does not reach the surface at several times, influences the results. Moreover, during winter, it is difficult to separate horizontal advection from vertical advection. The simulation time of E0 is too short to yield any results concerning the inter-annual variability. Instead of temperatures, chlorophyll concentrations are a possibility to illustrate the inter-annual variability of the upwelling. The SeaWIFS chlorophyll *a* data, as well as the fluorescence data observed in-situ, show the same slightly offshore directed jet during summer 2003 (VG3). Fig. 10.1 illustrates the similarity of the results of both observations. The in situ-data are depth-averaged. Although the enrichment of the chlorophyll occurs in the subsurface, the observations from satellite are able to detect this enrichment. One might say, that the chlorophyll concentrations from satellite-based observations offer a good approximation for the strength of the upwelling. However, it has to be mentioned, that the availability of the satellite data depends on the cloud cover. During several strong upwelling events cloud cover inhibited the detection of the concentration.

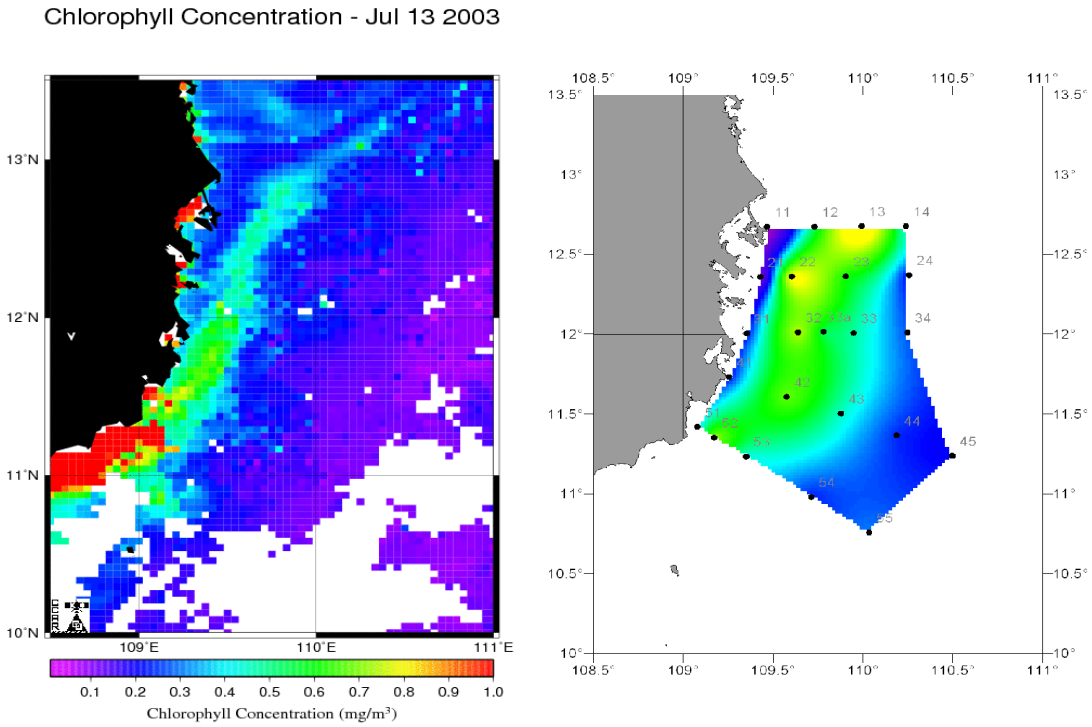

Fig. 10.1: Chlorophyll concentration from SeaWIFS observations (left) and depth-averaged in-situ observations during July 2003 (right)

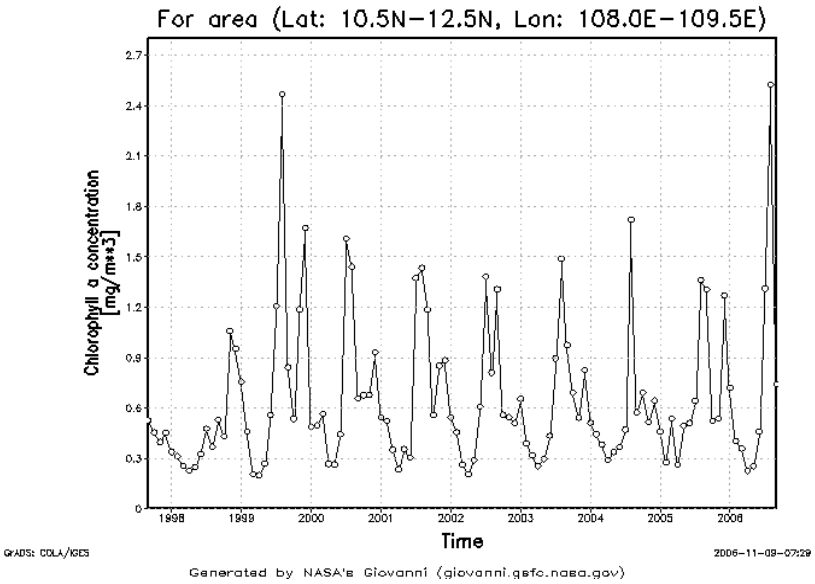

Fig. 10.2: Monthly averaged chlorophyll concentration from satellite observations from September 1997 to September 2006

Fig. 10.2 shows the monthly averaged chlorophyll concentration from SeaWIFS for the period from September 1997 to September 2006. Enriched chlorophyll concentrations can be found during summer as well as during winter. This is supported by the reproduced vertical velocities, which show positive vertical velocities during both seasons. In most years the magnitude of the concentration is higher during summer than during winter, but in some years the magnitude in December can reach the same range that was seen during summer.

The findings of Xie (2003), that the summer sea surface temperatures follow the ENSO state with a time lag of 6 months, raise the question if there is a connection between the chlorophyll concentration in winter and that of the following summer. As winter and summer we define those months with the strongest monsoon events, being November, December and January for the winter monsoon and July and August for the summer monsoon. Fig. 10.3 illustrates the anomalies of the concentrations for both seasons, the winter concentration is illustrated with the blue line, the summer with the red line. The green line is the ENSO state during winter represented by the Multivariate ENSO Index (MEI). The MEI is build by the US National Oceanic and Atmospheric Administration (http://www.cdc.noaa.gov/ENSO/).

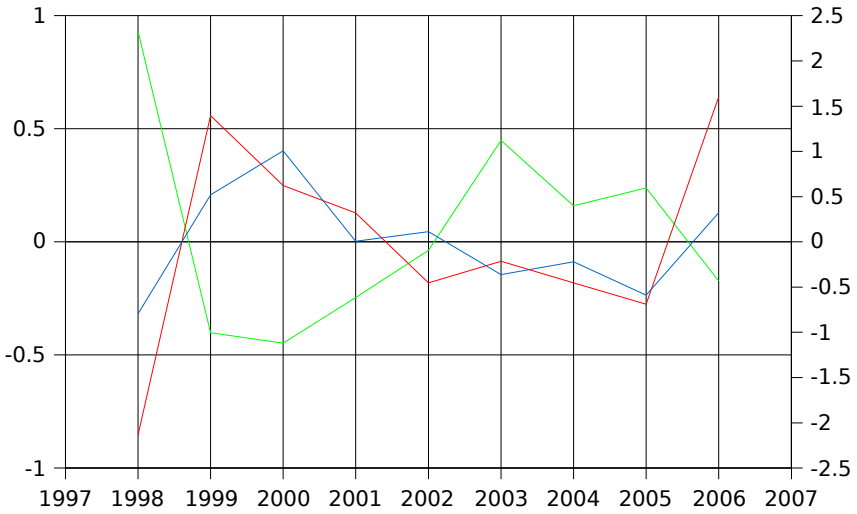

Fig. 10.3: Anomalies of the chlorophyll concentration during winter (blue line) and summer (red line) in mg m^{-3} and the MEI (green line)

The MEI is based on the six main variables observed for the tropical Pacific. These six variables are: sea-level pressure, zonal and meridional components of the surface wind, sea surface temperature, surface air temperature, and total cloudiness fraction of the sky.

Negative values of the MEI represent the cold ENSO phase (La Niña), while positive MEI values represent the warm ENSO phase (El Niño) in the pacific.

First, a significant correlation between both summer and winter concentration can be seen, at a value of 0.8. Hence, strong upwelling during winter is followed by strong upwelling in summer. On the monthly scale, the highest correlation can be found between July and the past winter (0.85).

Moreover, the figure shows a strong negative correlation between the winter MEI and the chlorophyll concentration in winter and summer. The correlation is significant, with -0.90 during winter and -0.86 during summer. An El Nino during winter weakens the chlorophyll concentration and the upwelling, during summer as well as during winter.

The reason for the correlation between the status of the SCS and the ENSO during summer, with a time lag of 6 months, is still a point of discussion. Xie et al. (1998) and Xie (2003) supposed an atmospheric relationship. Xie et al. (1998) found a delayed onset of the summer monsoon after an El Nino. In contrast Qu et al. (2004) mentioned that earlier studies ignore the advection of heat through the Luzon Strait. They found that, especially in winter, heat advection seems to be the only important process responsible for the cooling in the upper layer of the SCS. According to Qu et al. the SST in the SCS increases around the mature phase of El Niño and peaks in the following summer.

10
Summary & Outlook

10.1 Summary

The horizontal and vertical circulation in the upwelling area, as well as the hydrography south east of Vietnam, were illustrated and analysed with model studies and ship experiments. The processes which cause the vertical circulation are deducted and classified. Furthermore, the monthly variation of the upwelling in the VUA is simulated.

In chapter 2, a brief introduction into the monsoon system, as the most important driving force for the circulation, is given. The seasonal circulation of the SCS, as a review of earlier researches, is illustrated. The state of the art of the research of the upwelling regions in the SCS and especially in the VUA discovers the necessity of regional modelling studies and hydrographic surveys. Due to the local morphology the upwelling area itself can be divided into four different regions, which will be in the focus of the analyses.

Chapter 3 gives an overview of the used methods. The hydrodynamic model with the used boundary conditions as well as the adaptation of HAMSOM to the physical conditions of the SCS is presented. It was shown that the Smagorinsky scheme, implemented on the Arakawa C-grid, allows to calculate a variable horizontal turbulent exchange coefficient. Further on a simple algorithm to assimilate sea surface temperatures observed by satellites is illustrated. An overview of the instruments and procedures deployed during the ship experiments is given.

In chapter 4, a verification of the reproduction of the whole SCS with remote sensed data is conducted. The acceptable quality of the simulation in the region of the upwelling is documented with the illustration of analogies between the currents, the distribution of

temperature and salinity, reproduced and observed, respectively.

In the fifth chapter, the six typical states of the horizontal circulation are presented for several depths. The states highlight the change of the circulation due to the changing monsoon wind, as well as some features which occur independent from the wind forcing. The main characteristic is the appearance of a southward and a northward boundary current . The pathways of the boundary currents are strongly steered by the bathymetry. This yields to a complex mesoscale current system, with different meandering of the currents in different depths. Both boundary currents can exist at the same time during late summer. Together they build a confluence zone and form an offshore jet.
The vertical velocities in the VUA, according to the states of the horizontal circulation, are described. Upwelling was found at pronounced regions also during northeast monsoon and inter-monsoon. Significant positive vertical velocities can be found not only near the coast, but at two regions they spread cross the shelf. The magnitude of the vertical velocities of O(10 m day^{-1}) appears to be strong compared with other regions in the SCS, but the velocities cover the same range as off Yucatan.

Chapter 6 shows the hydrographic results of the ship experiments. The observations are set in relation to the vertical velocities of the model experiment. A complex structure in the distribution of temperature and salinity had been found. The two summer monsoon cruises give the feasibility to compare the observed hydrography due to different states of the circulation. Indications of upwelling can be found during the inter-monsoon cruises as well as in winter. The effectiveness of the upwelling on the primary production is documented by the observed data of the fluorescence. They identifies that the upwelling during summer as well as during spring and winter influence the primary production in a positive way.

In chapter 7, the processes, which explain the vertical velocities in two dimensions, hence neglecting the alongshore direction, are deducted. A spin-up experiment discovers that the wind driven upwelling, due to offshore movement of the surface layer, which will be compensated through the geostrophic interior, vanishes after three days. After this period the offshore flow is balanced by an onshore flow of the BBL. With the onset of the basin-wide circulation the upwelling due to the BBL is the most important process. On the shallow Sunda Shelf, where both boundary layers overlap, the equilibrium is achieved on the first day. The relation between the two dimensional processes and the results of the reconstruction of the vertical velocities of the model illustrates, that the two dimensional processes can explain the upwelling in the north of the VUA, where the bathymetry do not vary in the alongshore direction. However, in the center of the upwelling, where the shelf changes its depth, there is no correlation.

Chapter 8 deals with the three-dimensional processes. Due to the high Froude number of the southward boundary current, the inertial forces can become more important than the gravitational forces. Thus, if the shelf changes its depth a flow across the isobathes is possible. This causes a squashing of the water column, which results due to the conservation of the potential vorticity in an anticyclonic rotation. Both, the inertial forces and the anticyclonic rotation dispose the current into shallower water. With the assumption that the flow is aligned with the sloping bottom, upwelling is established. This process can occur independent of the local wind forcing.
A model experiment without the Mekong river illustrates, that during summer the stronger stratification due to the river discharge can decrease the vertical velocities.

The inter-annual variability and the correlation with the ENSO is pointed out in chapter 9, by using satellite based chlorophyll *a* concentrations. Increased concentrations can be found during winter and summer. Moreover, the magnitude of the concentration both during summer and winter is correlated with the ENSO status during winter. This means that an El Nino during winter, lowers the upwelling during winter and summer.

According to the research goals, defined in the introduction, the seasonal variability, and the influence of the monsoon on the variability of the coastal processes are studied. Summarizing, upwelling took place independent from the direction of the monsoon and can be found during summer, spring and winter.
In this work, the main governing processes are identified: The classical two dimensional processes can not explain the upwelling at all. Upwelling is forced mainly by the western boundary currents. Hence, the interaction of the boundary currents with the bathymetry is the main physical process, that is that 40 % - 100 % of the upwelling is forced by the basin-wide circulation and not by the direct influence of the local wind.
The stratification of the water column is the second important factor, which influences the strength of the upwelling. The discharge of the Mekong increases the stratification and with that the discharge decreases the vertical velocities.
The third goal was the inter-annual variability of the coastal activity. Therefore the relation between the ENSO and the upwelling was studied. A correlation of the ENSO with the upwelling, represented by the chlorophyll concentration was found. Both, the concentration during winter and the concentration during summer are correlated with the ENSO during winter.

10.2 Outlook

A main effect of the atmosphere on the ocean is the momentum exchange due to wind stress. But also, the ocean influences the atmosphere through radiation, sensible heat flux and release of latent heat, thus, several processes related to the SST. Hence, one main open question may is the influence of upwelling on the atmosphere. In this context it is remarkable that Xie (2003) found the greatest variability of the wind stress within the Asian Monsoon can be observed in the VUA. The high reflective cloud frequency (HRC) represents a possible consequence of upwelling on the atmosphere: Off the coast of Vietnam, the HRC is to be found only about 30% of that in the eastern part (Wang and Wu , 1997), hence they suggest a relative lower atmospheric convection, which can be explained with the colder water in the VUA due to the upwelling.

According to Defant (1950) a 1°C / 100 km temperature gradient can generate a surface wind of about 2 m s^{-1}. The direction of the wind is from the cold to the warm surface water with a deflection angle δ , which depends on the stratification of the atmosphere. δ can have a value between -20° and -30° (Chu, 1986, 1988) in the northern hemisphere. In the VUA, during summer, a gradient in the SST of O(1.5°C / 100 km – 3°C / 100 km) between upwelling influenced and non-influenced water is possible. This gradient of the SST can generate a thermal wind of O(3 m s^{-1} – 6 m s^{-1}).

Moreover, the thermal wind induced by the temperature difference between the land and the sea may influence the upwelling process. Franchito (1998) simulated a significant impact of the sea breeze on the vertical velocities.

However, the fact of a two way system has to be studied with a coupled ocean-atmospheric model.

Another interesting fact is, that a plume of Mekong influenced water is flowing into the upwelling area. This sets the focus on regions of fresh water influence (ROFIs), e.g., Simpson et al. 1996, de Kok et al, 2001. It was discussed that the Mekong influences the vertical velocities. Therefore, frontal structures in the ROFI and between upwelling induced water and riverine discharge is one goal of the second part of the Vietnam project.

The impact of climate change on the coastal processes is also an open question. Until now not all processes of the monsoon system itself are deduced, for example the linkage between the summer monsoon and the winter monsoon could not been answered.

Some technical improvements can accurate the results of the simulation of the upwelling. With nested models and a resolution of less than O(1 km), the morphology of the bathymetry in the VUA and processes on the mesoscale are represented in a more realistic manner. Furthermore, an advancement of the transport algorithms in the model may solve the frontal structures less diffusive. An assimilation of SSH in the model may threat the

simulation to more realism. Accordingly, the strength and the interaction of the two boundary currents will be improved.

Acknowledgments

I would like to thank Dr. Thomas Pohlmann for encouragement, helpful comments, criticisms and suggestions.
I would like to express my gratitude to the staff of the Institute of Oceanography Nha Trang, the crews of the research vessels and Dr. Rolf Peinert for their support and assistance in Vietnam.
Many thanks to all members of the cruises for having nice times in Vietnam and the help to weather through all the suffering during the cruises.
Thanks should be given all the colleagues of the Institute of Oceanography Hamburg for technical and scientific support.
I would like to thank Valentin Born who carefully corrected the English.

This work was funded by the DFG (Deutsche Forschungsgemeinschaft) and the BMBF (Bundesministerium für Bildung und Forschung).

Last but not least, i would like to thank Dörte Kröger for passing on me at several times and the support during stressful times.

Hartmut Hein

Hamburg, 10.03.2007

List of abbreviations

AMS	Asian Monsoon System
AVHRR	Advanced Very High Resolution Radiometer
BBL	Bottom-Boundary-Layer
EAM	East Asia Monsoon
ENSO	El Niño/Southern Oscillation
GRDC	Global Runoff Data Center
HRC	Highly Reflective Clouds
LST	Luzon Strait Transport
MEI	Multivariate ENSO Index
ROFI	Regions Of Fresh water Influence
SCS	South China Sea
SCSMEX	South Chine Sea Monsoon Experiment
SEAM	Southeast Asian Monsoon
SeaWiFS	Sea-viewing Wide Field-of-view Sensor
SSH	Sea Surface Heights
SST	Sea Surface Temperatures
TMI	Tropical Rainfall Measuring Mission Microwave Imager
UW	Upwelled Water
VLLJ	Vietnam Low Level Jet
VUA	Vietnam Upwelling Area

List of Figures

References

Annan J. D., Hargreaves J. C. , 1999: Sea surface temperature assimilation for a three-dimensional baroclinic model of shelf seas, Continental Shelf Research, Volume 19, Issue 11, Pages 1507 - 1520.

Allen, J.S., 1973: Upwelling and Coastal Jets in a Continuously Stratified Ocean, Journal Phys. Oceanogr., 3, 3, 245 – 257.

Alvares, A., Tintore, J., Sabates, A., 1996: Flow modification and shelf-slope exchange induced by a submarine canyon off the northeast Spanish coast, Journal Geophys.Res., Vol. 101, C5, 12043-12055.

Alvarez Fanjul, E., Perez Gomez, B. and Rodriguez Sanchez-Aravalo, I., 1997: A description of the tides in the Eastern North Atlantic. Prog. Oceanog., 40: 217-244.

Arthur, R.S., 1965: On the circulation of vertical motion in the eastern boundary currents from determination of horizontal motion, Journal Geophys. Res., 70, 2799 – 2803.

Atkinson, L. P., Brink, K. H., Davis, R. E., Jones, B. H., Paluszkiewicz, T., Stuart, D. W., 1986: Mesoscale hydrographic variability in the vicinity of Point Conception and Arguello during April – May 1983: The OPUS 1983 experiment. Journal Geophys. Res. 91, 12899 – 12918.

Bache, A. D., 1860: Lecture on the Gulf Stream, American Journal of Science and Arts 30, 1–17

Backhaus, J. O. and Hainbucher, D., 1987: A finite-difference general circulation model for shelf seas and its application to low frequency variability on the North European Shelf. In: J. C. J. Nihoul and B. M. Jamart (eds.), Three-Dimensional Models of Marine and Estuarine Dynamics, Elsevier Oceanography Series, 45: 221- 244.

Backhaus, J. O., 1983: A semi-implicit scheme for shallow water equations for applications to shelf sea modelling. Continental Shelf Research, 2, 243-254.

Backhaus, J. O., 1985: A three-dimensional model for the simulation of shelf sea dynamics. Dt. Hydrogr. Z., 38: 165-187.

Backhaus, J. O., Bartsch J., Damm P., Pohlmann T. and Schrum C., 1991: The marine weather bulletin North Sea. ICES, C.M. 1991/C:16 17p.

Becker, G.A., H.Giese, K.Isert, P.König, H.Langenberg, Th.Pohlmann, C.Schrum, 1999: Mesoscale variability in the German Bight. Deutsche Hydrogr. Zeitung, 51, No. 2/3, 155-179.

Boyer, T.P., J. Antonov, S. Levitus, M.E. Conkright, T. O' Brien, C. Stephens, D. Johnson, R. Gelfeld, 1998: NOAA Atlas NESDIS 20,World Ocean Database 1998 Volume 3: Temporal Distribution of Expendable Bathythermograph Profiles, U.S. Gov. Printing Office, Wash., D.C., 170pp.

Boyer, T.P., M.E. Conkright, S. Levitus, C. Stephens, T. O' Brien, D. Johnson, R. Gelfeld, 1998: NOAA Atlas NESDIS 21,World Ocean Database 1998 Volume 4: Temporal Distribution of Conductivity/Salinity-Temperature-Depth (Pressure) Stations, U.S. Gov. Printing Office, Wash., D.C., 160pp.

Boyer, T.P., M.E. Conkright, S. Levitus, D. Johnson, J. Antonov, T. O' Brien, C. Stephens, R. Gelfeld, 1998: NOAA Atlas NESDIS 22,World Ocean Database 1998 Volume 5: Temporal Distribution of Station Data Temperature and Salinity Profiles, U.S. Gov. Printing Office, Wash., D.C., 108pp.

Brown, P. C. and Field, J. G., 1986: Factors limiting phytoplankton production in a nearshore upwelling area, Journal of Plankton Research, Vol. 8.1, 55 – 68.

Cai, W. J. and Lennon, G., W., 1988: Upwelling in the Taiwan Strait in response to wind stress, ocean circulation and topography. Estuarine, Coastal and Shelf Science, 26, 15 -31.

Carbajal, N., 1993: Modelling of the circulation in the Gulf of California. Reports Centre of Marine Climate Research, 3: 1-186.

Centurioni, L. R., P. P. Niiler and D. K. Lee, 2004: Observations of inflow of Philippine Sea surface water into the South China Sea through the Luzon Strait. J. Phys. Oceanogr., 34 113–121.

Chang, C.-P. and K. M. Lau, 1980: Northeasterly Cold Surges and Near-Equatorial Disturbances over the Winter MONEX Area during Dec. 1974. Part II: Planetary Scale Aspects. Mon. Wea. Rev., 108, 298-312.

Chang, C.-P., P. A. Harr, J. McBride, and H. H. Hsu, 2004: Maritime Continent monsoon: Annual cycle and boreal winter variability. East Asian Monsoon, World Scientific Series on Meteorology of East Asia. Vol. 2,107-150.

Chao, S. -Y., P. -T. Shaw, and S. Y. Wu, 1996a: Deep sea ventilation in the South China Sea, Deep Sea Res., Part I, 43, 445–466.

Chao, S. -Y., P. -T. Shaw, and S. Y. Wu, 1996b: El Nino modulation of the South China Sea circulation, Prog. Oceanogr., 38, 51–93.

Chen, C.T.A., Huang, M.H., 1996: A mid-depth front separating. the South China Sea water and the West Philippine Sea water. Journal of Oceanography 52, 17 - 25.

Chen, T. C., M. C. Yen, W. R. Huang and W. A. Gallus Jr., 2002: An East Asia Cold Surge: Case Study, Mothly Weather Review, Vol 130, 2271- 2290.

Chu, P.C., 1987: Generation of unstable modes of the iceward attenuating swell by icebreeze," Journal of Physical Oceanography, 17, 828-832.

Chu, P.C., 1988: An instability theory of air-sea interaction for coastal upwelling. Advances in Atmospheric Sciences, 5, 277-285.

Chu, P.C. and C.J. Lozano, 1995: P-vector method for determining ocean circulation from hydrographic data, The 21st General Assembly of the International Association for the Physical Sciences of Oceans, Honolulu, Hawaii, 5-12.

Chu, P. C., S. Lu, and Y. Chen, 1997: Temporal and spatial variabilities of the South China Sea surface temperature anomaly, J. Geophys. Res., 102(C9), 20,937–20,956.

Chu, P. C., C. Fan, C. J. Lozano, and J. L. Kerling, 1998a: An airborne expendable bathythermograph survey of the South China Sea, May 1995, J. Geophys. Res., 103(C10), 21,637–21,652.

Chu, P.C., J. Veneziano, and M. Carron, 1998b: Response of the South China Sea to the tropical storm Ernie 1996, Second International Workshop on Princeton Ocean Model (POM), Princeton, 17-20.

Chu, P. C., N. L. Edmons and C.W. Fan, 1999: Dynamical mechanisms for the South China Sea seasonal circulation and thermohaline variabilities. J. Phys. Oceanogr., 29, 2971–2989.

Chu P.C., and R. F. Li, 2000: South China Sea isopycnal surface circulations. Journal Phys. Oceanogr, 30, 2419–2438.

Crusado, A., Salat, J., 1981, Interaction between the canary current and the bottom topography, Coastal Upwelling, Coastal and Estuarine Sciences 1, American Geophysical Union, 1-3.

Csanady, G.T., 1982, Circulation in the Coastal Ocean, D.Reidel Publishing Company, Dordrecht, Holland, page 179.

Csanady,G.T. , 1981, On the structure of transient upwelling events, Journal Phys. Oceanogr., 12, 84 – 96.

Cummins, P., F., Armi, L., Vagle, S., Upstream Internal Hydraulic Jumps., Journal of Physical Oceanography 36 (5): 753-769.

Dale, W. L., 1956: Winds and drift currents in the South China Sea. Malay. J. Trop. Geogr., 8, 1–31.

Dale, A.C., Barth, J.A., 2001: The hydraulics of an evolving upwelling jet flowing around a cape, Journal Phys.Oceanogr., 31, 226 – 243.

Defant F., 1950: Theorie der Land- und Seewinde. Arch. Meteor. Geophys. Bioklimatol, A2 404–425.

Derber, J. and Rosati, A., 1989: A global oceanic data assimilation system. Journal of Physical Oceanography 19, pp. 1333 – 1347.

Ding, Y. H., and T.N. Krishnamurti,1987: Heat budget of the Siberian high and the winter monsoon. Mon. Wea. Rev. 115, 2428-2449.

Ding, Y., 1990: Building-up, air mass transformation and propagation of Siberia high and its relations to cold surge in East Asia. Meteorol. Atmos. Phys., 44, 281-292.

Ding, Y.H., Li, C.Y., Liu, Y.J., 2004: Overview of the South China Sea monsoon experiment. Adv Atmos Sci 21: 343–360.

Ekman, V.W. 1905: On the influence of the earth's rotation on ocean currents, Ark. Mat. Astr. Fys.,. 2, 1-52.

Ekman, V.W., 1923, Über Horizontalzirkulation bei winderzeugten Meeresströmungen, Arkiv för Math., Arst. och Fysik, Band 17, No.26.

Elser, J., G., Rump, O., J., Johnson, E., R., 2005, Steady rotating flows over a ridge, Physics of Fluids, 17, 116601.

Fang, G., W. Fang, Y. Fang, and K. Wang,1998: A survey of studies on the South China Sea upper ocean circulation, Acta Oceanogr. Taiwan., 37, 1–16.

Findlater, J., 1969, A major low-level air current near the Indian Ocean during northern Sommer. Quart. J. Roy. Meteor. Soc. 95, 362 – 380.

Figueiras, F. G., Labarta, U., Reiriz, M. J. F., 2002: Coastal Upwelling, primary production and mussel growth in the Rias Baixas of Galicia, Hydrobiologia, 484, 121-131.

Franchito, S. H., Rao, V. B., Stech, J. L., Lorenzzetti, J. A., 1998: The effect of coastal upwelling on the sea-breeze circulation at Cabo Frio, Brazil: a numerical experiment. Annales Geophysicae 16: 866 – 881.

Freeland, H.J. and Denman, K.L., 1982: A topographically induced upwelling center off southern Vancouver Island, Journal Mar.Res., 40, 1069-1093.

Freeland, H.J., Crawford, W.R., Thomson, R.E., 1984: Currents along the Pacific coast of Canada, Atmos. Oceans, 22, 151-172.

Garvine, R. W., 1971: A simple model of coastal upwelling dynamics, Journal Phys. Oceanogr., 1, 169-179.

Garvine, R. W., 1973: The effect of bathymetry on the coastal upwelling of homogeneous Water, Journal Phys. Oceanogr., 3, 1, 47 – 56.

Geisler, J.E. 1981: A linear model of the Walker circulation. Journal of the Atmospheric Sciences, vol.38, no.7, p. 1390- 400.

Gentemann, C.L, F.J. Wentz, C.M. Mears, and D.K. Smith, 2004: In-situ validation of TRMM microwave sea surface temperatures, Journal of Geophysical Research, 109, C04021.

Gill, A.E., and Schuhmann, E.H., 1979: Topographically induced changes in the structure of an inertial coastal jet: Application to the Agulas Current, Journal Phys.Oceanogr., 9, 975-991.

Gill,A.E, 1982: Atmosphere-Ocean Dynamics, Academic Press, Orlando

Gordon, H. R., 1989: Can the Lambert-Beer law be applied to the diffuse attenuation coefficient of ocean water?, Limnol. Oceanogr., 34, 1389 – 1409.

Hainbucher, D. and Backhaus, J. O., 1999: Circulation of the eastern North Atlantic and north-west European continental shelf: a hydrodynamic modelling study. Fish. Oceanogr., 8 (Suppl. 1): 1 - 12.

Hainbucher, D., Pohlmann, T. and Backhaus, J. O., 1987: Transport of conservative passive tracers in the North Sea: First results of a circulation and transport model. Cont. Shelf Res., 7: 1161-1179.

Halpern, D. and Woiceshyn, P., 1999: Onset of the Somali Jet in the Arabian Sea during June 1997. Journal of Geophysical Research 104(C8): doi: 10.1029/1999JC900141.

Harms I., U. Hübner, J.O. Backhaus, M. Kulakov, V. Stanovoy, O. Stepanets, L. Kodina and R. Schlitzer 2002: Salt intrusions in Siberian River Estuaries - Observations and model experiments in Ob and Yenisei. accepted by Proceedings in Marine Science.

Harms I.H. and M.J. Karcher, 2001: Pathways of anthropogenic radionuclides in the Northern Oceans to appear in: E.M. Scott (ed.) 'Modelling Radioactivity in the Environment', Section 2: Case studies, Elsevier, submitted.

Harms I.H. and P.P. Povinec, 1999: The outflow of Radionuclides from Novaya Semlya Bays - Modelling and monitoring strategies Science of the Total Environment, 237/238.

Harms I.H., M. Heath, A. Bryant, J.O. Backhaus and D. Hainbucher, 2000: Modeling the northeast Atlantic circulation - Implications for the spring invasion of shelf regions by Calanus finmarchicus ICES-Journal of Marine Science, Vol. 57, no. 6, pp. 1694-1707.

Harms I.H., M.J. Karcher and D. Dethleff, 1999: Modelling Siberian river runoff -Implications for contaminant transport in the Arctic Ocean- Journal of Marine Systems, in press.

Harms I.H., M.J. Karcher and H. Burchard, 2001: Modelling oceanic pathways of radioactivity on local and regional scales, using hydrodynamic general circulation models. to appear in: E.M. Scott (ed.): 'Modelling Radioactivity in the Environment', Section 1: Technical modelling issues, Elsevier, submitted.

Harms, I. H., Backhaus, J. O. and Hainbucher, D., 1999: Modelling the seasonal variability of circulation and hydrography in the Iceland-Faeroe-Shetland overflow area. ICES CM 1999/L:10, Annual Science Conference, 29 September to 2 October 1999, Stockholm, Sweden.

Harms, I.H. 1992: A numerical study of the barotropic circulation in the Barents and Kara Seas. Continental Shelf Research, Vol. 12, No. 9.

Harms, I.H. 1997: Modelling the dispersion of 137Cs and 239Pu released from dumped waste in the Kara Sea. Journal of Marine Systems, Vol. 13 (1997), pp. 1 – 19.

Harms, I.H. 1997: Watermass transformation in the Barents Sea. -Application of The HAMburg Shelf Ocean Model (HAMSOM)- ICES-Journal of Marine Science, 54, pp. 351 – 365.

Harms, I.H. and M.J. Karcher 1999: Modelling the saisonal variability of circulation and hydrographiy in the Kara Sea. Journal of Geophysical Research, Vol. 104, No. C6.

Helder, W., Schrum, C., Shiemmield, G., 1996: North Sea budget. In J. Hall, S. V. Smith and P.R. Boudreau. Report on the International Workshop on Continental Shelf Fluxes of Carbon, Nitrogen and Phosphorus. LOICZ Reports and Studies 9, JGOFS Report 22, 50p.

Hidaka, K., 1954. A contribution to the theory of upwelling and coastal currents, Trans. Amer. Geophys.Union, 35, 431 -444.

Hoffmann, P., 1884: Zur Mechanik der Meeresstömungen, Mittler und Sohn, Königliche Hofbuchhandlung, Berlin.

Houghton, R.W., 1976: Circulation and hydrographic structure over the Ghana continental shelf during the 1974 upwelling, Journal Phys.Oceanogr., 6, 909-924.

Houghton, R.W., Beer,T., 1976: Wave propagation during the ghana upwelling, Journal of Geophys. Res., 81, 24, 4423-4429.

Houghton, R.W., Colin, C., 1986: Thermal structure along 4°W in the Gulf of Guinea during 1983- 1984, Journal Geophys. Res., 91z, 11727-11739.

Hsueh, Y. and O'Brien,J., 1972: Steady coastal upwelling induced by an along-shore current, Journal Phys. Oceanogr., 1, 180-186.

Hsueh, Y., Kenney III, R.N., 1972: Steady coastal upwelling in a continuously stratified ocean, Journal Phys. Oceanogr., 2, 27 -33.

Hsueh, Y., Ou, H.-W., 1975: On the possibilities of coastal mid-shelf and shelf break upwelling, Journal Phys.Oceanogr., 5, 670-682.

Hu, J. Y., H. Kawamura, H. S. Hong and Y. Qi, 2000: A review on the currents in the South China Sea: Seasonal circulation, South China Sea Warm Current and Kuroshio intrusion. J. Oceanogr., 56, 607–624.

Hu, J.Y., H. Kawamura, H. Hong, M. Suetsugu, M. Lin, 2001: Hydrographic and Satellite Observations of Summertime Upwelling in the Taiwan Strait: A Preliminary Description, Terrestrial, Atmospheric and Oceanic Sciences, Vol 12.2, 415-430.

Huang, Q. Z., W. Z. Wang, Y. S. Li and C. W. Li, 1994: Current characteristics of the South China Sea. p. 39–47. Oceanology of China Seas 1, ed. by D. Zhou et al., Kluwer.

Huang, D., 1995: Modelling Studies of Barotropic and Baroclinic Dynamics in the Bohai Sea. Reports Centre of Marine Climate Research, 17: 1 – 126.

Hübner U. und J. Backhaus, 1997: Der küstennahe Gezeitenstrom im Gebiet der östlichen Ostfriesischen Inseln. Forschungszentrum Terramare, Bericht Nr. 4, 65pp, ISSN 1432-797X.

Hull, D. and Bacon, D.J., 1984: Introduction to Dislocations, 3rd Edition (Int. Series on Mat. Science and Technology, Vol. 37) Pergamon Press.

Hwang, C. and S. A. Chen, 2000: Circulations and eddies over the South China Sea derived from TOPEX/Poseidon altimetry. J. Geophys. Res., 105, 23943-23965.

Ingham, M.C., 1970: Coastral upwelling in the northwestern of Gulf of Guinea, Bull. Marine Sci., 20, 2-34.

Isobe A., and T. Namba, 2001: The circulation in the upper and intermediate layers of the South China Sea,Journal of Oceanography,57, 93-104.

Ito, T, Kaneko, A., Furokawa, H., Gohda, N., Koterayama, W., 1995: A structure of the Kuroshio and it's related upwelling on the East China Shelf Slope, Journal Oceanogr., Vol.51, 267 – 278.

Jeffrey, S.W., Humphrey, G.F., 1975: New spectrophotometric equation for determining chlorophyll a, b, c1 and c2. Biochem. Physiol. Pflanz., 167:194-204.

Johnson, J.A., 1982: A two time-scale model of stratified shelf currents, Continental Shelf Research, 1, 2, 143-157.

Kalman, R.E., 1960: A new approach to linear filtering and prediction problems. Journal of Basic Engineering 82D, pp. 33 – 45.

Kara, A. B., A. J. Wallcraft, and H. E. Hurlburt, 2005: Sea surface temperature sensitivity to water turbidity from simulations of the turbid Black Sea using HYCOM, Journal Phys. Oceanogr., 35, 33 – 54.

Keen, T. R., Kindle, J., C., and Young, D, K, 1997: The interaction of southwest monsoon upwelling, advection and primary production in the northwest Arabian Sea Journal of Marine Systems, 13, 61-82.

Kling, J. M., 1996: Circulation near submarine canyons: A modeling study, Journal of Geophysical Research -Oceans 101 (C1): 1211-1223.

Kochergin, V.P., 1987, Three-dimensional prognostic models. In: Three-dimensional coastal ocean models. Ed.: N.S. Heaps. Washington, D.C.:American Geophysical Union, Coastal and Estuarine Science 4, 201-208.

Kok, J. M. de, C. de Valk, J. H. Th. M. van Kester, E. de Goede, R. E. Uittenbogaard, 2001: Salinity and Temperature Stratification in the Rhine Plume. Estuarine, Coastal and Shelf Science 53, 467-475.

König, P., C. Schrum, 1997: Hydrographic Observations and Model Results From a PRISMA Drift Experiment April (23 to 29, 1991), Marine Ecology Progress Series, Vol. 156, 255-261.

Kuo N.-J., Zheng Q., Ho C.-R., 2004: Response of Vietnam coastal upwelling to the 1997-1998 ENSO event observed by multisensor data, Remote Sensing of Environment, Volume 89, Number 1, pp. 106-115(10).

Kuo N.-J., Quanan Z., Ho C.-R., 2000: Satellite observation of upwelling along the western coast of the South China Sea, Remote sensing of environment, vol. 74, no3, pp. 463-470.

Landau, L. D., Lifshitz, E. M., 1986: Theory of Elasticity. Course of Theoretical Physics, Volume 7. Pergamon Press, Oxford.

Lau, K. M., C.-P. Chang and P. H. Chan, 1983: Short-Term Planetary-Scale Interactions over the Tropics and Mid-latitudes. Part II: Winter-MONEX Periods. Mon. Wea. Rev., 111, 1372-1388.

Lau, K. M., and P. H. Chan, 1983a: Short-term climate variability and athmospheric teleconnection as inferred from satellite derived outgoing longwave radiation Part I: simultaneous relationships. Journal Atmos.Sci, Vol. 40,No 12, 2735-2750.

Lau, K. M., and P. H. Chan, 1983b: Short-term climate variability and athmospheric teleconnection as inferred from satellite derived outgoing longwave radiation Part II: lagged correlations. Journal Atmos.Sci, Vol. 40,No 12, 2751-2767.

Lau, K. M., and N. C. Lau, 1984: The Structure and Energetics of Midlatitude Disturbances Accompanying Cold-air Outbreak over East Asia. Mon. Wea. Rev., 112, 1309-1327.

Lau, K. M. and C.-P. Chang, 1987: Planetary Scale Aspects of Winter Monsoon and Teleconnections. Monsoon Meteorology, Oxford University Press, 161-202.

Lau, K. M., Yang, G. J., Shen, S.H., 1988: Seasonal and intraseasonal climatology of summer monsoon rainfall over East Asia, Mon. Wea. Rev. 116, 18-37.

Lau K.-M. and S. Yang, 1996: The Asian monsoon and predictability of the tropical ocean-atmosphere system. Q. J. Roy. Meteor. Soc., 122, 945-957.

Lau, K. M., Yang, G. J., 1997, Climatology and interannual variability of the Southeast Asian summer Monsoon., Advances in Atmos. Sciences, 14, 141 – 162

Lau, H.T. Wu and S. Yang, 1998: Hydrologic processes associated with the first transition of the Asian summer monsoon: A pilot satellite study. Bull. Amer. Meteor. Soc., 79, 1871–1882.

Lebedev, I. and Nof, D., 1996, The Drifting Confluence Zone, Journal of Physical Oceanography, 2, 2429 – 2448.

Lee, Z. P., Du,K., P., Arnone, R., Liew, S., C., Penta, B., 2005: Penetration of solar radiation in the upper ocean: A numerical model for oceanic and coastal waters, Journal of Geophysical Research, 110, C9, C09019.

Lemhart, H. J., Radach, G., Backhaus, J.O., Pohlmann, T., 1995: Simulations of the North Sea circulation, its variability, and its implementation as hydroponical forcing in ERSEM. Netherlands Journal of Sea Research, Vol. 33.3, 271-299.

Lenhart, H. J. and Pohlmann, T., 1997: The ICES-boxes approach in relation to results of a North Sea circulation model. Tellus, 49A, 139 – 160.

Leth, O, Middleton, J., F., 2004: A mechanism for enhanced upwelling off central Chile: Eddy advection, Journal of Geophysical Research, Volume 109, Issue C12, C12020.

Li, R. F., Q. C. Zeng, Z. Z. Ji and D. Gun, 1992a: Numerical simulation for a northeastward flowing current from area off the eastern Hainan Island to Tsugaru/Soya Strait. La mer, 30, 229–238.

Li, R. F., Z. Z. Ji and Q. C. Zeng, 1992b: The simulation of the circulation in the western Pacific Ocean. p. 115–126. In Collected Papers of the Symposium on Ocean Circulation, China Ocean Press, Beijing.

Li, R. F., Q. Z. Huang and W. Z. Wang, 1994: Numerical simulation of the upper currents in the South China Sea. Acta Oceanologica Sinica, 16(4), 13–22.

Li, C., and M. Yanai, 1996: The onset and interannual variability of the Asian summer monsoon in relation to land-sea thermal contrast. Journal of Climate, 9, 358-375.

Lill, C.C., 1979: Upwelling over the shelf break, Journal Phys. Oceanogr., 9, 1044-1047.

Lim, H. and C.-P. Chang, 1981: A Theory for Mid-Latitude Forcing of Tropical Motions during Winter Monsoons. J. Atmos. Sci., 38, 2377-2392.

Lim, Y.-K., Kim, K.-Y., Lee, H.-S., 2002: Temporal and Spatial Evolution of the Asian Summer Monsoon in the Seasonal Cycle of Synoptic Fields, Journal of Climate, vol. 15, Issue 24, pp. 3630-3644.

Liu, X. B. and J. L. Su, 1992: A reduced gravity model of the circulation in the South China Sea. Oceanologia et Limnologia Sinica, 23(2), 167–174.

Liu, K.K., Chao, S.Y., Shaw, P.T., 2002: Monsoon-forced chlorophyll distribution and primary production in the South China Sea: observations and a numerical study. Deep-Sea Research Part I - Oceanographic Research Papers 49 (8): 1387-1412.

Longhurst, A.R., 1962: A review of the oceanography of the Gulf of Guinea, Bull- IFAN, A24, 633 - 663.

Lu, R.Y. and Ren, B.H., 2005: The influence of ENSO on the seasonal convection evolution and the phase of 30-60-day oscillations during boreal summer. JOURNAL OF THE METEOROLOGICAL SOCIETY OF JAPAN 83 (6): 1025-1040.

Luff, R. and Pohlmann, T., 1996: Calculation of Water Exchange Times in the ICES-Boxes with an Eulerian Dispersion Model using a Half-Life Time Approach. Dt. Hydrogr. Z., 47, No. 4: 287- 299.

Madden, R. A., and Julian, P. R., 1971: Detection of a 40 – 50 day oscillation in the zonal wind in the tropical Pacific. Journal Atmos. Sci., 28, 702 -708.

Matsumoto, J. 1992: The seasonal changes in Asian and Australian monsoon regions, Journal Met. Soc. Japan, 70, 257-273.

Mao, M., W. Z. Wang, Q. Z. Huang, S. C. Fu, Y. S. Li and C. W. Li, 1992: A three dimensional numerical simulation of the South China Sea circulation. Tropic Oceanology, 11 (4): 34 - 41.

Mao, J., Chan J. C. L. and Wu, G. 2004: Relationship between the Onset of the South China Sea Summer Monsoon and the Structure of the Asian Subtropical Anticyclone, Journal of the Meteorological Society of Japan Vol. 82, No. 3 pp.845-859.

Meehl, G.A., Arblaster, G., M., Loschnigg, J., 2003: Coupled ocean-atmosphere dynamical processes in the tropical Indian and Pacific Ocean regions and the TBO, Journal of Climate, 16, 2138- 2158.

Merino, M., 1997: Upwelling on the Yucatan Shelf: hydrographic evidence. Journal of Marine Systems, 13 , 101-121.

Metzger, E.J., 2003: Upper Ocean sensitivity to wind forcing in the South China Sea. Journal of oceanography 59, no. 6, 783-798.

Metzger, E. J., and Hurlburt, H. E., 1996: Coupled dynamics of the South China Sea, the Sulu Sea, and the Pacific Ocean, J. Geophys. 101, C5, 12,331–12,352.

Metzger, E. J., and Hurlburt, H. E., 2001: The nondeterministic nature of Kuroshio penetration and eddie shedding in the South China Sea. Journal Phys. Oceanogr., 31, 1712-1732.

Middleton, J., F., Leth, O., 2004b: Wind-forced set-up of upwelling, geographical origins and numerical models: the role of bottom drag. Journal of Geophysical Research, 109, doi:10.1029/2003JC002126.

Morimoto, A., Yoshimoto, K. and Yanagi, K., 2000: Characteristics of sea surface circulation and eddy field in the South China Sea revealed by satellite altimetric data. Journal of Oceanogr., 56, 331-344.

Münchow, A., 2000: Wind Stress Curl Forcing of the Coastal Ocean near Point Conception, California, Journal of Physical Oceanography, Vol. 30, 1265 -1280.

Neale R, and Slingo, J., 2003: The maritime continent and its role in the global climate: a GCM study. Journal of Climate, 16: 834–848.

Ning, X., Chai, F., Xue, H., Cai, Y., Liu, C., Shi, J., 2004: Physical-biological oceanographic coupling influencing phytoplankton and primary production in the South China Sea, Journal of Geographical Research, Vol. 109, C10005.

O'Brian, J.J., Hurlburt, H.E., 1972: A numerical model of coastral Upwelling, Journal Phys.Oceanogr., 2, 14- 20.

Pedlosky, J., 1974: On coastal jets and upwelling in bounded basins, Journal Phys. Oceanogr., 4,1, 3-18.

Pedlosky, J., 1978: A inertial model of coastal upwelling, Journal Phys.Oceanogr., 8, 171-177.

Pedlosky, J., 1978: A nonlinear model of the onset of upwelling, Journal Phys.Oceanogr., 8, 178- 187.

Pohlmann, T., 1987: Three-dimensional circulation model of the South China Sea, in Nihoul, J.C.J., and Jamert, B.M., eds., Three-dimensional models of marine and estuarine dynamics: Amsterdam, Elsevier, p. 245-268.

Pohlmann, T., 1991: Evaluations of hydro- and thermodynamic processes in the North Sea with a 3-dimensional numerical model. Reports Centre of Marine Climate Research, 23: 1– 116.

Pohlmann , T., 1996a: Predicting the thermocline in a Circulation Model of the North Sea – Part I: Model description, calibration and verification. Continental Shelf Research, Vol. 16, No. 2, 131-146.

Pohlmann, T., 1996b: Calculating the annual cycle of the vertical eddy viscosity in the North Sea with a three-dimensional baroclinic shelf sea circulation model. Cont. Shelf Res., Vol. 16, No. 2: 147 – 161.

Pratt, L. and Helfrich, K., 2005: Generalized Conditions for Hydraulic Criticality of Oceanic Overflows, Journal of Physical Oceanography, 35 (10): 1782-1800.

Pringle,J. M., 2002: Enhancement of Wind-Driven Upwelling and Downwelling by Alongshore Bathymetric Variability, Journal of Physical Oceanography 2002 32: 3101-3112.

Qu, T., 2000: Upper-layer circulation in the South China Sea. Journal Phys. Oceanogr., 30, 1450–1460.

Qu, T., Kim Y. Y., Yaremchuk, M., 2004: Can Luzon Strait Transport Play a Role in Conveying the Impact of ENSO to the South China Sea?, Journal of Climate, Volume 17, Issue 18, 3644–3657.

Rasmusson, E. M. and T. H. Carpenter, 1982: Variation in the tropical sea surface temparature and surface wind field associated with the Southern Oscillation /El Nino. Mon. Wea. Rev., 110, 345–384.

Rossby, C. G., 1940: Planetary flow pattern in the atmosphere. Quart. Journal R. Soc. Can. Branch. 66, 68- 87.

Rojana-anawat, P., Pradit, S., Sukramongkol, N., Siriraksophon, S., 2001: Temperature, salinity, dissolved oxygen and water masses of Vietnamese waters. Proceedings of the SEAFDEC Seminar on Fisheries Resources in the South China Sea, Area 4: Vietnamese Waters, 346-355.

Roughan, M. and Middleton, J.H., 2002: A comparison of observed upwelling mechanisms off the east coast of Australia, Continental Shelf Research, 22, 2551-2572.

Schrum C., 1994: Numerische Simulation thermodynamischer Prozesse in der Deutschen Bucht. Berichte aus dem Zentrum für Meeres- und Klimaforschung, Reihe (B), Nr.15. 175 S.

Schrum, C. ,Huebner, U., Janssen, F., 2000: Recent Climate Modelling in North Sea and the Baltic Sea. Part A: Model description and validation. Berichte des Zentrums für Meeres- und Klimaforschung, Reihe B, 37, 59 S.

Schrum, C., 1997: Auswirkungen interannualer Klimavariabilität auf Nordsee und Ostsee, Annalen der Meteorologie 34, 169-170.

Schrum, C., 1997: Thermohaline stratification and instabilities at tidal mixing fronts. Results of an eddy resolving model for the German Bight. Cont. Shelf Res., 17(6), 689-716.

Schrum, C., 1999: Sensitivity of atmosphere-ocean heat exchange in the Baltic Sea. Publicationes Instituti Geographici Universitatis Tartuensis 84, 7-10, 154-160.

Schrum, C.,2001: Regionalization of climate change for the North Sea and the Baltic Sea. Climate Research 18, 31-37.

Schrum, C., F. Siegismund, M. St. John, 2001: Decadal Variations in the stratification and circulation patterns of the North Sea. Are the 90's unusual? ICES Symposium of Hydrobiological Variability in the ICES area 1990-1999. Accepted by ICES publication Series.

Schrum, C., Huebner, U., Podzun, R., Jacob, D., 2001: A coupled atmosphere/ice/ocean model for the North Sea and the Baltic Sea. Berichte des Zentrum für Meeres- und Klimaforschung der Universität Hamburg, 41.

Schrum, C., Janssen, F., Hübner, U., 1999: Modelling the interannual variability of hydro- and thermodynamics in the North Sea and the Baltic Sea. ICES CM 1999/O:05, 11p.

Schott, F. A., Dengler, M., Schoenefeld, R., 2002: The shallow overturning circulation of the Indian Ocean, Progress in Oceanography, 53, 57 -103.

Shaw, P. -T., 1989: The intrusion of water masses into the sea southwest of Taiwan, J. Geophys. Res., 94, 18,213–18,226.

Shaw, P. -T., 1991: Seasonal variation of the intrusion of the Philippine seawater into the South China Sea, J. Geophys. Res., 96, 821–827.

Shaw, P. T., and S. Y. Chao, 1994: Surface circulation in the South China Sea, Deep Sea Res., 41, 1663–1683.

Shaw, P. T., S. U. Chao, K. K. Liu, S. C. Pai, and C. T. Liu, 1996: Winter upwelling off Luzon in the northeast South China Sea, J. Geophys. Res., 101, 16,435–16,448.

Shaw, P. T., Chao, S. Y. and Fu, L. L., 1999: Sea surface height variations in the South China Sea from satellite altimetry. Oceanologica Acta, 22(1), 1-17.

Simpson, J. H., 1996: Physical Processes in the ROFI regime, Journal of Marine Systems 12, 3-15.

Smagorinsky, J. 1963: Some historical remarks on the use of nonlinear viscosities, in Large eddy simulation of complex engineering and geophysical flows, edited by B. Galperin and S. A. Orszag. Cambridge University Press.

Smith, R.L., 1968: Upwelling, Oceanogr. Mar.Biol.Rev, Vol 6, London, George Allan and Unwin Ltd., 11 -47.

Smith, R.L., 1981: A comparison of the structure and variability of the flow field in three coastal upwelling regions: Oregon, Northwest Africa and Peru, Coastal Upwelling, Coastal and Estuarine Sciences 1, American Geophysical Union, 107-118.

Stronach, J. A., Backhaus, J. O. and Murty, T. S., 1993: An update on the numerical simulation of oceanographic processes in the waters between Vancouver Island and the Mainland: the GF8 model. Oceanogr. Mar. Biol. Annu. Rev., 31: 1-87.

Su, J. L. and X. B. Liu, 1992: The circulation simulation of the South China Sea. p. 206–215. In Collected Papers of the Symposium on Ocean Circulation, China Ocean Press, Beijing.

Sverdrup, H.U., 1938: On the process of upwelling, Journal Marine Res., 1, 155-167.

Sverdrup, H.U., 1941: The influence of bottom topography on ocean currents, Applied Mechanics, 1941, 6-75.

Tang, D. , D.R. Kester, I.H. Ni, H. Kawamura, H. Hong, 2002: Upwelling in the Taiwan Strait during the summer monsoon detected by satellite and shipboard measurements, Remote Sensing of Environment, 83, 457–471.

Thompsom, J.D., O'Brian,J.J., 1973: Time-dependent coastal upwelling, Journal Phys. Oceanogr., 3, 33 -46.

Thomson, J., D., and Schmitz, W., J., Jr., 1989: A limited – area model of the Gulf Stream: Design, initial experiments, and model-data intercomperation, Journal of Physical Oceanography, 19, 791 – 814.

Tomczak, M. and J.S. Godfrey, 1994: Regional Oceanography: An Introduction. Pergamon Press, 422 pp.

Trenberth, K., E., Stepaniak, D., P., and Caron, J. M., 1999: The Global Monsoon as Seen through the Divergent Atmospheric Circulation. Journal of Climate: Vol. 13, No. 22, pp. 3969-3993.

Versraete,J.-M.,1992: The seasonal upwelling in the Gulf of Guinea, Prog.Oceanogr. 29, 1- 60.

Wang, J., 1985: A steady circulation model in the South ChinaSea. Journal of Shangdong College of Oceanology, 15(3), 22–31.

Wang B., and R. Wu, 1997: Peculiar temporal structure of the South China Sea summer monsoon. Adv. Atmos. Sci., 2, 177–194.

Wang, B., Wu, R., and X. Fu, 2000: Pacific–East Asian teleconnection: How does ENSO affect East Asian climate? J. Climate, 13, 1517-1536.

Webster, P. J., 1983: Mechanics of monsoon low frequency variability: surface hydrological effects. Journal of the Atmospheric Sciences 40: 2110-2124.

Webster, P. J., 1987: The variable and interactive monsoon. Monsoons, J. S. Fein and P. L. Stephens, Eds., Wiley and Sons, 269–330.

Webster, P.J. and S. Yang, 1992: Monsoon and ENSO: Selectively interactive systems. Quart. Journal Roy. Meteor. Soc., 118, 877–926.

Wooster, W.S., 1981: An upwelling mythology, Coastral Upwelling, Coastral and Estuarine Sciences 1, American Geophysical Union, 1-3.

Wu, C. R., Shaw, P. T. and Chao, S. Y., 1998: Seasonal and interannual variations in the velocity field of the South China Sea. J. Oceanogr., 54, 361-372.

Wu, C.-R., Shaw, P.-T., Chao, S.-Y., 1999: Assimilating altimetric data into a South China Sea model, Journal of Geophysical Research, Volume 104, Issue C12, p. 29987 - 30006.

Wyrtki, K., 1961: Physical oceanography of the southeast asian waters, Naga Rep. 2, 195 pp., Scripps Inst. of Oceanogr., La Jolla, Calif.

Xie, A.,Chung, Y. S., Liu X.,Ye, Q., 1998: The inter-annual Variations of the Summer Monsoon Onset over the South China Sea, Theoretical and Applied Climatology, 59, 3-4, 201-213.

Xie X. P., Xie, Q., Wang, D., Liu, W.D., 2003:Summer upwelling in the South China Sea and its role in regional climate variations, JOURNAL OF GEOPHYSICAL RESEARCH, VOL. 108, NO. C8, 3261.

Xu, X., Q. Zhang and H. Chen, 1982: The general descriptions of the horizontal circulation in the South China Sea. Proc. of the Symposium of the Chinese Society of Marine Hydrology and Meteorology, Chinese Society of Oceanology and Limnology, Science Press, Beijing, 119-127.

Xu,J., Chai F., Lui, Z., Zhu B., 2003: Several significant hydrographic characteristics and their formation mechanism in the South China Sea during spring and summer of 1998, Acta Oceanologia Sinca, Vol. 22, No. 4, 491-502.

Xue, H., F. Chai, N. R. Pettigrew, D. Xu, M. Shi, and J. Xu, 2004: Kuroshio intrusion and the circulation in the South China Sea, J. Geophys. Res., 109, C02017, doi:10.1029/2002JC001724.

Yanai, M., C. Li, and Z. Song, 1992: Seasonal heating of the Tibetan Plateau and its effects of the evolution of the Asian summer monsoon. J. Meteor. Soc. Japan, 70, 189-221.

Yang, H.J., Liu, Q., Liu, Z., Wang, D.X., Liu, X.B., 2002: A GCM study of the dynamics of the upper ocean circulation of the South China Sea. Journal of Geophysical Research 107(C7), doi: 10.1029 /2001JC001084.

Yang, H. and Q. Liu, 2003: Forced Rossby wave in the northern South China Sea. Deep-Sea Res. Part I: Oceanographic Res. Papers, 50(7), 917–926.

Yoshida, K., 1957: Coastal upwelling off the California coast, Rec. Oceanogr. Wks Japan, 2, 2,1-13.

Yoshida, K., 1967: Circulation in the eastern tropical oceans with special references to upwelling and undercurrents, Jap. Journal Geophys., 4, 2, 1 -75.

Zaneveld, J. R. V., J. C. Kitchen, and H. Pak, 1981: The influence of optical water type on the heating rate of a constant depth mixed layer, Journal of Geophysical Research, 86, 6426-6428.

Zeng, Q., R. Li, Z. Ji, Z. Gan and P. Ke, 1989: Calculations of the monthly mean circulation in the South China Sea. Scientia Atmospherica Sinica, 13, 127–168.

Zeng, Q. C., R. F. Li, Z. Z. Ji, P. F. Ke and Z. J. Gan, 1992: The simulation of monthly mean circulation of the South China Sea. p. 127–165. In Collected Papers of the Symposium on Ocean Circulation, China Ocean Press, Beijing.

Zhang, Y., J. M. Wallace, and D. S. Battisti, 1997: ENSO-like interdecadal variability: 1900–93. Journal Climate, 10, 1004–1020.

Zimmermann, P.H.; Selkirk, H.B.; Newell, R.E., 1988: The relationship between large-scale vertical motion, highly reflective cloud, and sea surface temperature in the tropical Pacific region. Journal of Geophysical Research, vol.93, no.D9, p. 11205-15.